The Effect of Wall Thermal Conductivity on Shock Wave Reflection

Richard Berry

A dissertation submitted to the Faculty of Engineering and the Built Environment, University of the Witwatersrand, Johannesburg, in fulfilment of the requirements for the degree of Master of Science in Engineering.

Johannesburg, June 2017

Declaration

I declare that this dissertation is my own, unaided work, except where otherwise acknowledged. It is being submitted for the degree of Master of Science in Engineering in the University of the Witwatersrand, Johannesburg. It has not been submitted before for any degree or examination at any other university.

Signed this 14th day of June 2017

Richard Berry

Acknowledgements

I would like to thank the following people:

Professor Beric W. Skews for his supervision of this project. His assistance and guidance in all aspects has been invaluable in the production of this dissertation.

Mr. Randall T. Paton for his assistance in the testing procedure and oversight of the testing within the Flow Research unit.

Mr. Russell E. Hall for his assistance and expertise in the operation of the experimental equipment, as well as input in the design of testing apparatus.

The technical staff in the North West Engineering laboratory workshop, for their diligent work in producing the required components to repair the shock tube and construct the test apparatus, as well as the maintenance required in order to allow testing to occur.

Mr. Antony P. Cohen for his help and advice throughout the research and writing of this dissertation as well as aspects of my personal well-being.

Mr. Paul Sauer and the staff at Airbus Defence and Space Optronics for their assistance and diligence in creating optical windows and the glass test piece timeously in addition to the polishing of the test pieces, allowing the project to proceed.

Lastly, I would like to thank my parents Nigel and Paula Berry for their unending support, motivation and sacrifices to allow me to complete my studies.

Abstract

In traditional two-dimensional shock wave theory the reflection of a shock wave off a surface is treated as an adiabatic process and that the reflection surface is perfectly rigid and smooth with an inviscid flow of the fluid. In reality it has been found that these assumptions are not entirely accurate, and that although they are a good indication in the regular and irregular reflection domains of shock waves over the surface, viscous and thermal effects are present within the flow field. It has been experimentally shown that the transition of regular reflection to irregular reflection exceeds the theoretical limit, which is known as the von Neumann paradox. This paradox has largely been accounted for in the formation of a viscous boundary layer behind the reflected shock wave, based on numerous experimental and computational studies. However, the thermal effects in the reflection process have largely been neglected as the assumption of heat transfer between the post-shock wave gas and the reflection surfaces is assumed to be invalid.

These thermal effects were investigated by testing materials with a varying range of thermal conductivities (1.13 to 401 W/mK) and similar surface roughness's below the suggested limit for hydraulic smoothness. Each experiment placed two test pieces at the same incidence angle, symmetrically in the shock tube. This allowed flow properties to be exactly the same for the two materials being tested with a single plane shock wave. Test Mach numbers ranged from 1.2790 to 1.3986, with tests conducted at shock wave incidence angles of 36°, 40°, 60° and 70°. This allowed both the regular and irregular reflection domains to be tested. Shadowgraph images were created using a z-configuration optical set up. These shadowgraph images were analysed quantitatively based on the angles measured as well as qualitatively based on flow features and symmetry.

Both the quantitative and qualitative tests indicated that there was a difference in the angles between the reflected shock waves and surfaces based on the material thermal conductivity. In the quantitative tests the value of this angle was larger for materials with a lower thermal conductivity, and smaller for ones with a higher thermal conductivity for the regular reflection cases. In the irregular reflection cases the angle between the reflected and incident shock waves was larger for materials with a higher thermal conductivity. The materials with midrange thermal conductivities had reflection angles that lay within the

bounds of the glass and copper angle values. The qualitative images supported these findings showing asymmetry in materials with different thermal conductivities with the intersection of reflected shock waves lying closer to the material with a higher thermal conductivity. Control experiments using test pieces made from an identical material showed no bias due to the location of the test piece in the shock tube.

Contents

List of Figures

List of Tables

Nomenclature

The following symbols are used in this dissertation and are common throughout unless otherwise specified. Symbols without units indicated are dimensionless.

ρ - Density [kg/m^3]
t - Time [s]
a - Speed of sound [m/s]
γ - Adiabatic index (Ratio of specific heats)
R - Specific gas constant [J/kg.K]
v - Velocity [m/s]
M - Mach number
V - Volume [m^3]
P - Pressure [Pa]
n - Number of moles
T - Temperature [K]

Chapter 1 Introduction

1.1 Background

In traditional two-dimensional shock wave theory in fluid flows, reflecting surfaces have been regarded as isothermal, smooth and adiabatic (no heat transfer). This assumes that there is no formation of viscous and thermal boundary layers close to the reflection surface, which would affect the shock wave geometry and reflection angles.

It has also been experimentally established that Regular Reflection persists into the Irregular Reflection domain of shock wave reflection patterns, dependant on the fluid flow properties. This is further discussed in chapter 2

Studies into viscous boundary layer effects behind the reflection point of shock waves have been performed to attempt to explain this phenomenon. This was done ascertain the influence of these boundary layers on shock wave reflection patterns. These studies have yielded positive results with numerical studies supporting the experimental results.

The formation of thermal boundary layers has not been extensively tested, as a possible influence in the reflection angles of shock waves as the adiabatic and isothermal assumptions were always made.

Previous work performed by Berry [**1**] in undergraduate study yielded positive results by varying the reflection surface thermal conductivity, thus altering the possible thermal boundary layers. However, limited results were obtained due to the scope of the undergraduate project. Additionally, the accuracy of the shadow photography visualisation was fairly poor due to the thickness of shock waves in the photographs, producing error bounds that lie too close together to be able to provide definitive conclusions. Thus based on these limited results the effects of thermal conductivity could not conclusively be proven.

It was expected that the shock waves would be self-similar (to maintain the same reflection

angle) throughout each test. However, an unexpected result occurred where the reflection angles changed during the shock waves transition over the reflection surface.

This dissertation subject is an extension of this work and previous work by Barbosa, Skews, de Saxe and Jogessar.

Barbosa and Skews [**2**] created an adiabatic reflection surface that is perfectly rigid and smooth by reflecting two shock waves off each other, using a bifurcated shock tube. In this way the symmetry plane becomes the reflection surface, that satisfies all assumptions made in gas dynamics theory. The results from these experiments supported the theoretical point of transition from Regular to Irregular Reflection. From these results it was concluded that viscous and thermal boundary layers could be the cause of the persistence of Regular Reflection as these layers were not present in the testing.

De Saxe [**3**] and Jogessar [**4**] performed experiments in an undergraduate study of different materials to test if the different thermal conductivities at varied shock wave incidence angles would have an effect on the shock wave reflections. In their testing, only one test piece was loaded in the shock tube at a time. This was detrimental to the experimental results as the flow conditions of pressure, temperature and Mach number could not be accurately reproduced over the various materials and incidence angles. This resulted in an inability to directly compare the results obtained for the different materials. This method was improved on by Berry[**1**] where two test pieces were loaded in the shock tube at a time. This method and results will be discussed further in the literature review.

1.2 Purpose of Study

The purpose of this study is to further the research performed into the influences that a material's thermal conductivity has on the reflection patterns of shock waves.

The study will focus mainly on the experimental results of the reflection of shock waves off plane surface with different thermal conductivities. In the study the degree to which thermal conductivity affects the reflection angles of shock waves will be tested. This will either support or disprove previous work.

The test pieces to be used in the testing will be larger (2.125 times longer) than in previous studies in order to test conclusively the transient effects of the shock waves. The longer

test pieces will allow for a longer test duration and produce more defined reflection patterns.

1.3 Problem Statement

In the study of shock wave reflection off plane surfaces, it is postulated that the material thermal conductivity may have an influence on the reflection angles, and therefore the reflection patterns that are produced. Prior experimentation has yielded positive results, yet more extensive testing is required with more accurate visualisation and longer test pieces in order to conclusively support or reject previous results.

1.4 Assumptions

Traditional assumptions of adiabatic reflection surfaces will be disregarded as these are the subject of the experimentation. The surfaces will be assumed to be hydraulically smooth, as they will be polished to the limits accepted as smooth.

Chapter 2 Literature Survey

2.1 Introduction

This literature review presents the concepts and theory relating to compressible flow properties, shock wave motion and reflection, the utilisation of shock tubes, the visualisation method that will be used in the experimentation as well as pertinent previous work. These sections aim to provide a foundation of understanding for the study topic and what is to be expected from analytical and experimental procedures.

2.2 Fluid Properties in Compressible Flows

2.2.1 General Theory

Fluid flows are analysed in two broad categories of classification, compressible and incompressible fluid flows. The distinction between the two characterisations is based on the change of density of the fluid within a volume that is changing. If the density of the fluid particles remains constant as they move through the flow field, the flow is considered to be incompressible. The mathematical expression for this condition is depicted as: [**5**]

$$\frac{D\rho}{Dt} = 0 \tag{2.1}$$

Similarly, if the density does change such that:

$$\frac{D\rho}{Dt} \neq 0 \tag{2.2}$$

Then as the fluid particles move through the flow field, the flow is considered to be compressible.

In general, incompressible flow fields are considered to exist when the fluid velocity is lower than 30% of the speed of sound propagation in the fluid. Alternatively when the fluid velocity is higher than 30% of the speed of sound propagation in the fluid, the flow is considered to be compressible with density effects becoming significant at this limit. The speed of sound propagation (speed of sound) of the fluid is dependant on the thermodynamic properties of the fluid. Incompressible flow is considered to occur when the speed of sound is relatively high or the flow velocity is relatively low. In this category, the flow is assumed to have a constant density if the density variations are less than 3%.

Most liquids are considered to be incompressible as the speed of sound in these fluids is relatively high, whilst in gasses the speed of sound is relatively low and therefore, gasses are considered to be compressible as compressibility effects are experienced as the flow velocity approaches the speed of sound in the fluid.
The speed of sound in the fluid is calculated from the following equation:

$$a = \sqrt{\gamma RT} \tag{2.3}$$

Flow regimes in a fluid are separated based on the Mach number of the flow. The Mach number is the ratio of the fluid flow velocity to the speed of sound in the fluid, given by the following equation:

$$M = \frac{V}{a} \tag{2.4}$$

The sonic condition, is where the fluid is flowing at the speed of sound and the Mach number is 1. Fluid flows are separated into two general conditions, subsonic and supersonic. Subsonic cases are experienced when the flow is travelling slower than the speed of sound ($M < 1$) and supersonic when the flow is travelling faster than the speed of sound ($M > 1$). These two divisions are further separated into other flow regimes as shown in Table 2.1.

Table 2.1: Flow regime domains and properties

Mach Number	**Flow Regime**	**Fluid Properties**
0.0 < M < 0.3	Incompressible	Density effects are considered negligible.
0.3 < M < 0.8	Subsonic	Density effects are significant, however, there are no regions of localised supersonic flow.
0.8 < M < 1.2	Transonic	Some localised regions of supersonic flow. Supersonic and subsonic regions are separated by shock waves.
1.2 < M < 5.0	Supersonic	Entire flow is supersonic. Shock waves are present in this flow regime.
5.0 < M	Hypersonic	Strong shock waves are experienced in this flow regime. Chemical properties of the gasses affect the gas dynamics of the flow.

The chemical properties that affect the gas dynamics in the hypersonic flow regime include, but are not limited to the vibrational modes of the gas atoms as well as dissociation of the gas molecules at very high speeds and plasma ionization.

2.2.2 Ideal Gas Assumption

It is assumed that in the experimentation, numerical and analytical solutions that air is an Ideal Gas. This is an assumption based on a calorically perfect gas [**6**]. This is when the specific heat capacity of the gas is constant, which is assumed to be true at subsonic and low supersonic flow conditions, which is in the flow velocity domain of testing for this experimentation. The specific heat capacity is the constant of how much heat is added for a given temperature rise per unit of mass.

The Ideal Gas assumption is expressed in the Ideal Gas law given as [**7**]:

$$P = \rho RT \tag{2.5}$$

Where for air ($\gamma = 1.4$)
R= 287.1 J/kg.K.

Compression shock waves are discontinuities that result in a large temperature increase across the shock wave. Depending on the strength of the shock wave, there may be dissociation and ionization of the gas particles across the shock wave. However, at the shock wave Mach numbers generated in testing, this behaviour is unexpected and the Ideal Gas assumption will be used as a fair representation of the gas properties during testing.

2.3 Shock Wave Theory

Shock waves are discontinuities that propagate through fluid flows. These disturbances are characterised by large variations in pressure, density and temperature occurring across the shock wave. They form in order to preserve the conservation of mass, energy and momentum within the flow field. Shock wave topology is dependant on many factors of the fluid flow, such as properties of the fluid as well as the shape and speed of objects within the flow field. The most rudimentary shock waves occur in one-dimensional fluid flows. They are described as normal shock waves as they occur perpendicular to the direction of the fluid flow. In two-dimensional cases oblique shock waves form when the flow is "turned on itself" or, in a supersonic flow where the flow is turned into the main bulk of the flow [**8**]. The normal shock wave is a special case of the two-dimensional oblique shock wave.

2.3.1 Normal Shock Waves

In Figure 2.1 a normal shock wave is shown with the flow conditions upstream of the shock wave denoted as 1 and downstream of the shock wave denoted as 2. The flow parameters upstream of the shock wave are given and the relations between the parameters upstream and downstream are found by applying conservation of mass, energy and momentum equations.

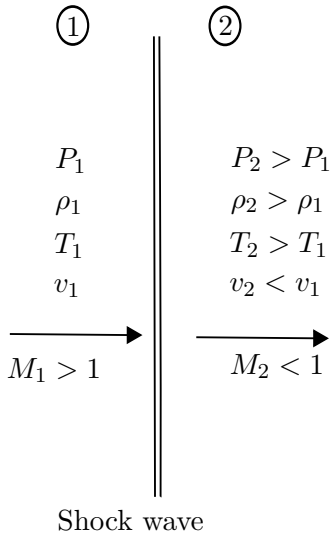

Figure 2.1: Schematic of normal shock wave

After rearranging these equations to solve for certain properties the following equations can be used to determine the properties of the flow downstream of the normal shock wave. The equations reflect a calorically perfect gas, meaning that it is assumed to be an Ideal Gas. These equations also apply only in frictionless flows, with no heat addition.

$$M_2^2 = \frac{1 + [(\gamma - 1)/2]M_1^2}{\gamma M_1^2 - (\gamma - 1)/2} = \left[\frac{(\frac{2}{\gamma - 1} + M_1^2)}{(\frac{2\gamma}{\gamma - 1}M_1^2 - 1)}\right] \tag{2.6}$$

$$\frac{\rho_2}{\rho_1} = \frac{v_1}{v_2} = \frac{(\gamma + 1)M_1^2}{2 + (\gamma - 1)M_1^2} \tag{2.7}$$

$$\frac{P_2}{P_1} = 1 + \frac{2\gamma}{\gamma + 1}(M_1^2 - 1) = \frac{1 + \gamma M_1^2}{1 + \gamma M_2^2} \tag{2.8}$$

$$\frac{T_2}{T_1} = \left[1 + \frac{2\gamma}{\gamma + 1}(M_1^2 - 1)\right]\left[\frac{2 + (\gamma - 1)M_1^2}{(\gamma + 1)M_1^2}\right] = \frac{(1 + \frac{\gamma - 1}{2}M_1^2)}{(1 + \frac{\gamma - 1}{2}M_2^2)} \tag{2.9}$$

Equation 2.6 shows that the downstream Mach number is only a function of the upstream Mach number in an ideal gas. In the case when M_1=1, leading to M_2=1, there is the weakest two dimensional shock wave possible. As the upstream Mach number increases the shock wave becomes stronger and the downstream Mach number gets smaller. When the upstream Mach number approaches infinity the downstream Mach number approaches a finite minimum value.

2.3.2 Moving Normal Shock Waves

Equation 2.6 to Equation 2.9 only applies to stationary shock waves. However, in the testing moving shock waves will be generated that will propagate into stationary air. The equations can be used if the viewer reference frame is moved to coincide with the shock wave. This is equivalent to superimposing a reference velocity to an observer so that the shock wave appears to be stationary. This is called a Galilean transformation [**9**].

Figure 2.2 shows a normal shock wave moving at velocity v_s from left to right into a stationary gas. Again subscripts 1 and 2 denote the upstream and downstream conditions respectively. It can be seen that the gas behind the shock wave is flowing with a velocity of v_a.

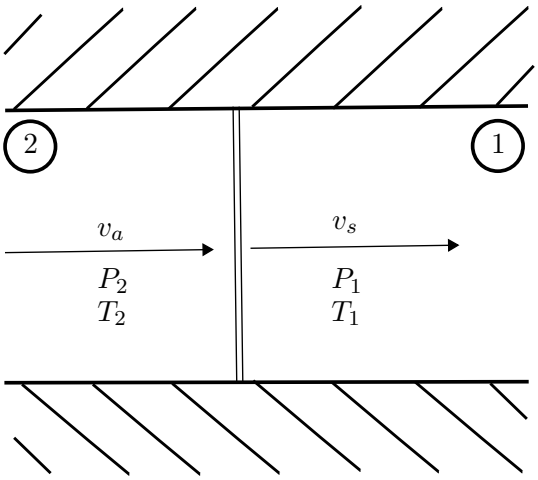

Figure 2.2: Schematic of a moving normal shock wave

In Figure 2.3 the Galilean transformation has been performed and the reference frame is now attached to the shock wave. Here the flow upstream of the shock wave is flowing into the shock wave at a velocity of v_s and the flow downstream is flowing away from the shock wave at a velocity of $v_s - v_a$.

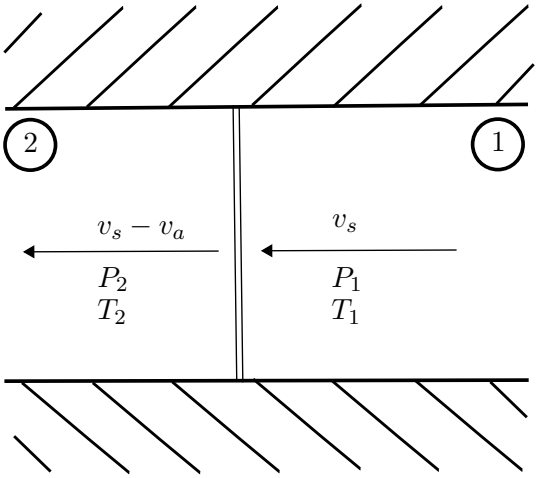

Figure 2.3: Schematic of a normal shock wave with a transformed reference frame

The static conditions of pressure and temperature on either side of the shock wave ($P_1, P_2, T_1, T_2, \rho_1$ and ρ_2) are thermodynamic properties of the fluid and are not affected by the Galilean transformation. However, the stagnation conditions ($P_{01}, P_{02}, T_{01}, T_{02}$) which are measured when the gas is brought isentropically to rest, are dependant on the reference frame applied and so once the static conditions are determined, there must be a transformation back to the original reference plane in order to calculate the stagnation conditions of the gas.

This method will be used later in the reflection of shock waves in order to calculate the reflection angles of shock waves, when reflected off plane surfaces.

2.4 Two-Dimensional Fluid Flows and Shock Wave Reflections

2.4.1 Formation of Oblique Shock Waves

Oblique shock waves are formed in two dimensional supersonic flow fields, when the flow is forced to change direction by a sharp compressive wedge in the flow. This process is explained in Ben-Dor [**10**] and a short summary is given here. The following cases are for steady flow conditions.

The first case is where the fluid flow streamlines approach the wedge at a subsonic velocity as can be seen in Figure 2.4. The boundary conditions require the fluid to flow parallel with the surfaces. As the flow is travelling slower than the speed of sound in the fluid, information of the inclined surface propagates upstream into the flow and the streamlines are "aware" of the wedge before they encounter it and can undergo subsonic turning to change their trajectory to flow parallel with the wall after encountering the wedge.

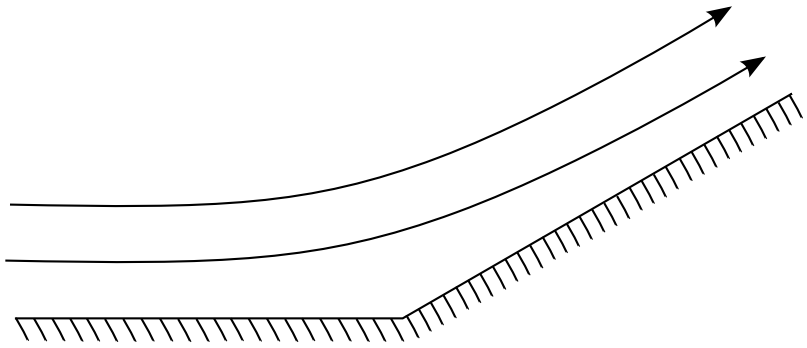

Figure 2.4: Fluid flow turning sub-sonically over a compressive angled wedge

In the next case the fluid flow is supersonic and the wedge angle satisfies the condition: $\theta_w < \delta_{max}(M_0)$ where $\delta_{max}(M_0)$ is the maximum possible wedge deflection for the flow that travels at a velocity of M_0. The information of the wedge's presence cannot propagate into the flow. Therefore the streamlines do not "know" that there is an obstacle ahead of it that requires the flow to be turned. The only way that the flow can alter its direction is for an oblique shock wave to form at the leading edge of the wedge. This allows the streamlines trajectory to change instantaneously so that the streamlines are parallel to the wall. This process is shown in Figure 2.5.

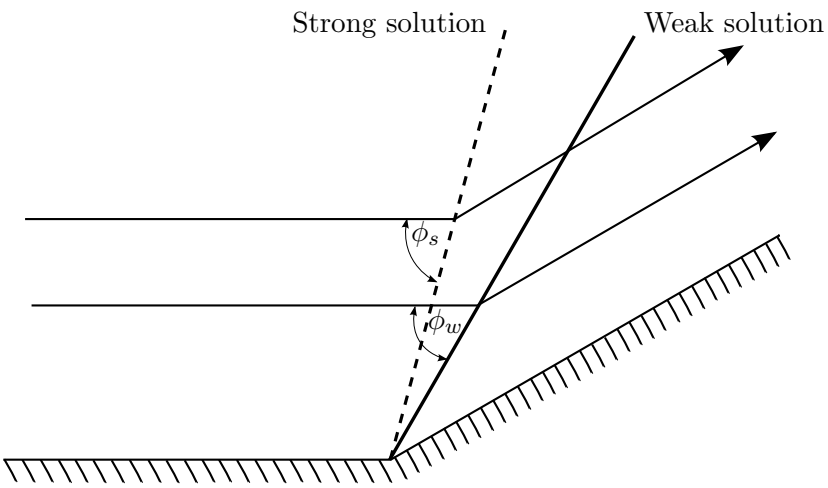

Figure 2.5: Attached oblique shock wave formation on a sharp compressive wedge

As can be seen in Figure 2.5 there are two solutions (strong and weak), that allow for the formation of an oblique shock wave. The solution which corresponds to the strong shock wave is shown as the dotted line. The angle of incidence between the strong shock wave and the oncoming flow is given as ϕ_s. This angle is always greater than the angle of the weak shock wave (solid line) and the oncoming flow, given as ϕ_w. Although both solutions turn the streamlines, the flow downstream of a strong shock wave is subsonic while the flow downstream of a weak shock is usually supersonic. Normally weak shock wave solutions are experienced unless special measures are put in place to ensure that the strong shock wave solution is achieved.

Lastly when $\theta_w > \delta_{max}(M_0)$, an attached straight shock wave cannot form and a detached shock wave known as a bow shock wave forms ahead of the wedge. This is case is shown in Figure 2.6

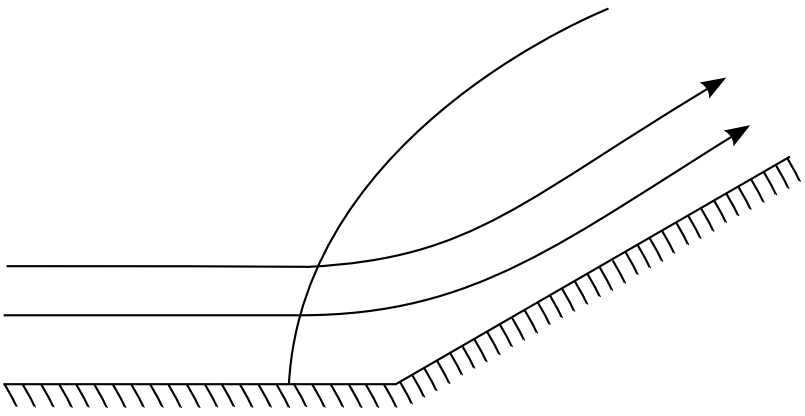

Figure 2.6: Detached bow shock wave formation and subsonic turning at a sharp compressive wedge

As the flow passes through the bow shock wave a region behind it becomes subsonic. Thereafter smooth subsonic turning can occur around the wedge as was seen in the first case.

2.4.2 Regular Reflection of Oblique Shock Waves

Shock wave reflection occurs when the shock waves encounter solid boundaries, a free stream or other shock waves. This occurs in order to satisfy boundary conditions, such as parallel flow to the wall [**10**]. This process will be discussed using a two dimensional parallel tunnel with a compressive wedge surface. The supersonic flow with a velocity of M_0 approaches the wedge as can be seen in the figure. The wedge angle is set such that $\theta_w < \delta_{max}(M_0)$ so that an oblique shock wave will form at the leading edge of the wedge

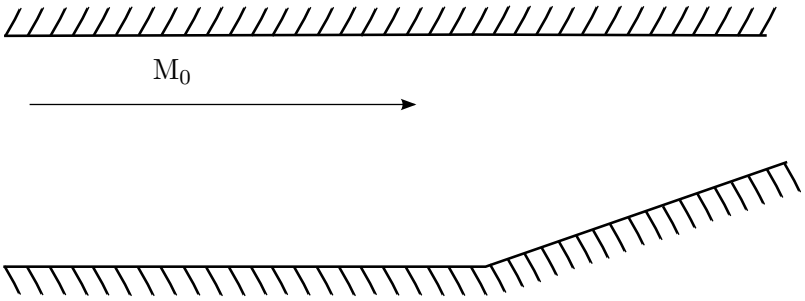

Figure 2.7: Supersonic flow in tunnel approaching a compressive wedge

The flow will be turned so that it is parallel with the inclined wall in order to satisfy the boundary conditions. This is performed through the formation of an oblique shock wave based on the wedge angle and flow conditions. The turned flow (M_1) and initial shock wave is shown in Figure 2.8.

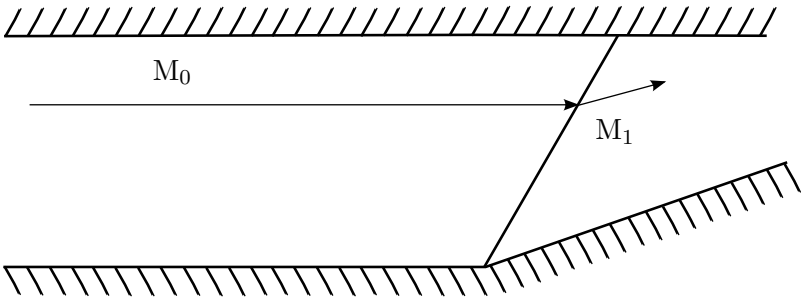

Figure 2.8: Supersonic flow after initial shock wave interaction

After this initial shock wave interaction, the fluid flow is now travelling towards the top wall, and must be turned again to flow parallel to this wall. This is done by the formation of a reflected shock wave to turn the flow again. This is seen in Figure 2.9.

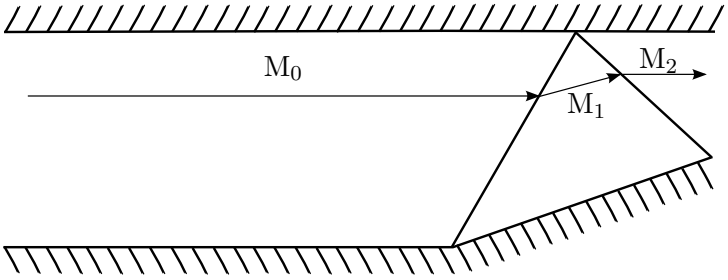

Figure 2.9: Supersonic flow after reflected shock wave interaction

The flow denoted M_2 is now travelling parallel to the top wall as is required by the boundary conditions.

The case given above shows the reflection principle for a steady flow regime, such as one created in a supersonic wind tunnel. Here the shock waves are stationary. However, in an unsteady flow case, where a shock wave moves into a steady flow and encounters a compressive wedge the reflection pattern that forms is shown in Figure 2.10.

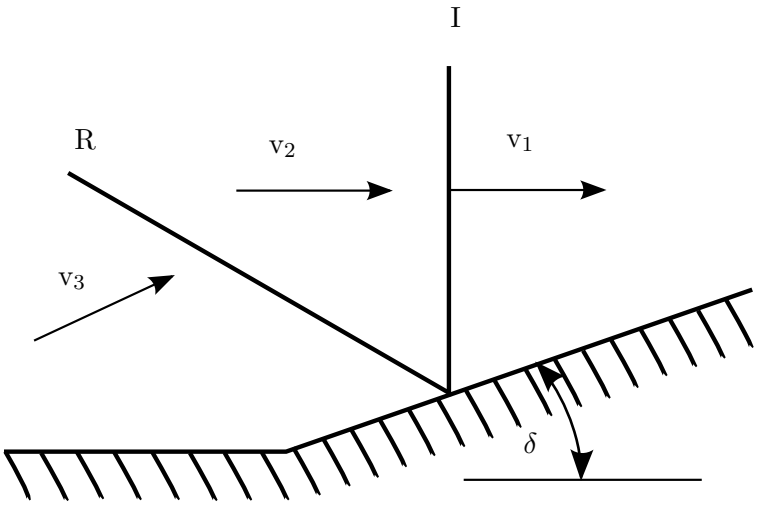

Figure 2.10: Reflection of moving normal shock wave on compressive wedge

In this case, the incident shock wave (I) is approaching the wedge surface set at a deflection of (δ) at a velocity of v_1. A reflected shock wave forms (R) and the velocities of the flow between the shock waves and after the reflected shock waves are given as v_2 and v_3 respectively.

By rotating the geometry by an angle (δ), the reflection topology can be arranged as is shown in Figure 2.11. The point on the wedge surface where the incident and reflected shock waves meet is called the reflection point. This point moves along the surface at a velocity of $\frac{v_1}{sin\delta}$.

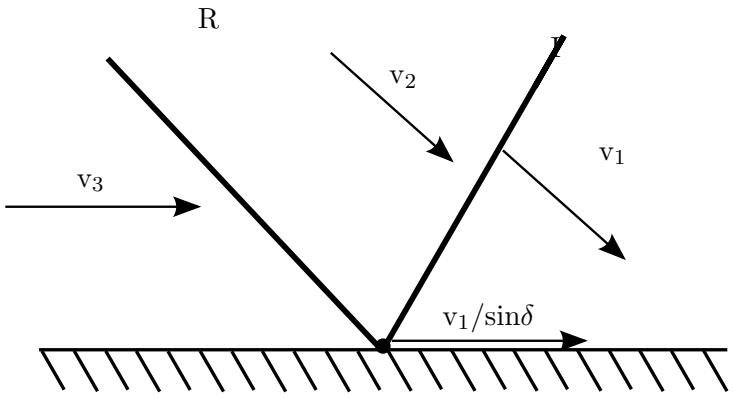

Figure 2.11: Reflection of moving normal shock wave on compressive wedge rotated by δ

As in the case of moving normal shock waves it is advantageous to perform a Galilean transformation and place the reference frame at the reflection point which is shown in Figure 2.12. In this reference frame the shock waves are stationary, and the shock wave equations for steady oblique shock waves can be used. This is known as a pseudo-steady reference frame.

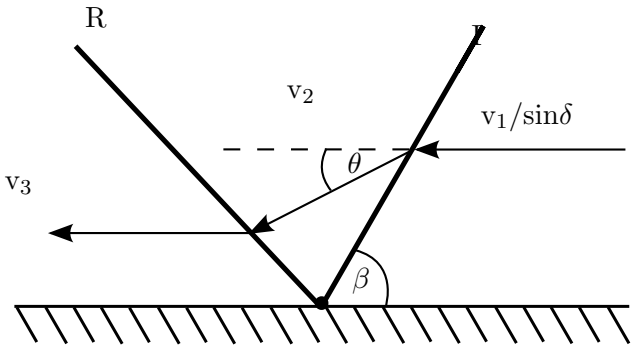

Figure 2.12: Reflection of a shock wave in a pseudo-steady reference frame

The angle β is the shock wave incidence angle and the angle θ is the flow turning angle. The flow turning angle is the angle that the flow is turned by the incident shock wave and subsequently turned by the same angle in the opposite direction by the reflected shock wave.

As previously discussed, the reflection point is the point where the incident and reflected shock waves meet. In the case where this point lies on the reflection surface this is termed as Regular Reflection (RR). However, based on the fluid flow parameters of Mach number and shock wave incidence angle, Regular Reflection may no longer be possible. After the limit of Regular Reflection the reflection point moves off of the surface and further shock waves are formed. This is called Irregular Reflection (IR) and will be discussed in the next section.

The equations that relate the flow parameters across the oblique shock waves in the Regular

Reflection domain are given below [**8**]:

$$M_{n1} = M_1 sin\beta = \frac{v_1}{a_1} \tag{2.10}$$

$$\frac{P_2}{P_1} = 1 + \frac{2\gamma}{\gamma + 1}(M_{n1}^2 - 1) \tag{2.11}$$

$$M_{n2}^2 = \frac{M_{n1}^2 + [2/(\gamma - 1)]}{[2\gamma/(\gamma - 1)]M_{n1}^2 - 1} \tag{2.12}$$

$$M_2 = \frac{M_{n2}}{sin(\beta - \theta)} \tag{2.13}$$

Where a subscript of n denotes the conditions travelling normal or perpendicular to the shock wave.

2.4.3 Irregular Reflection

For the Regular Reflection case, the reflection topology is determined by the shock wave incidence angle (β) and Mach number (M). These are also related to the flow turning angle (θ) in the $\theta - \beta - M$ relation given in equation Equation 2.14. The conventions are shown in Figure 2.13.

$$tan(\theta) = 2cot(\beta)\left[\frac{M_1^2 sin^2(\beta) - 1}{M_1^2(\gamma + cos(2\beta)) + 2}\right] \tag{2.14}$$

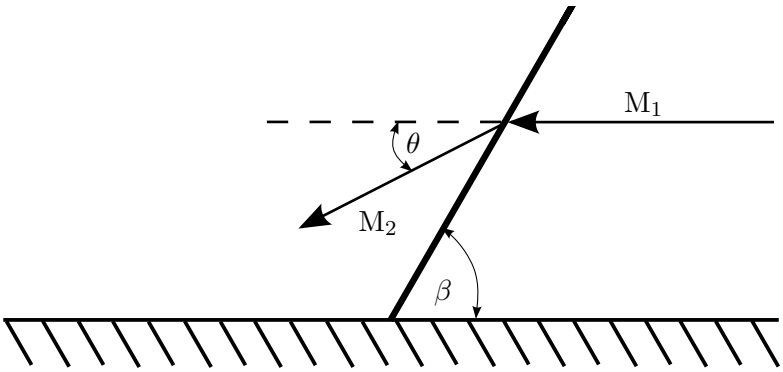

Figure 2.13: Conventions for $\theta - \beta - M$ relationship

This relationship produces $\theta - \beta - M$ curves as can be seen in Figure 2.14.

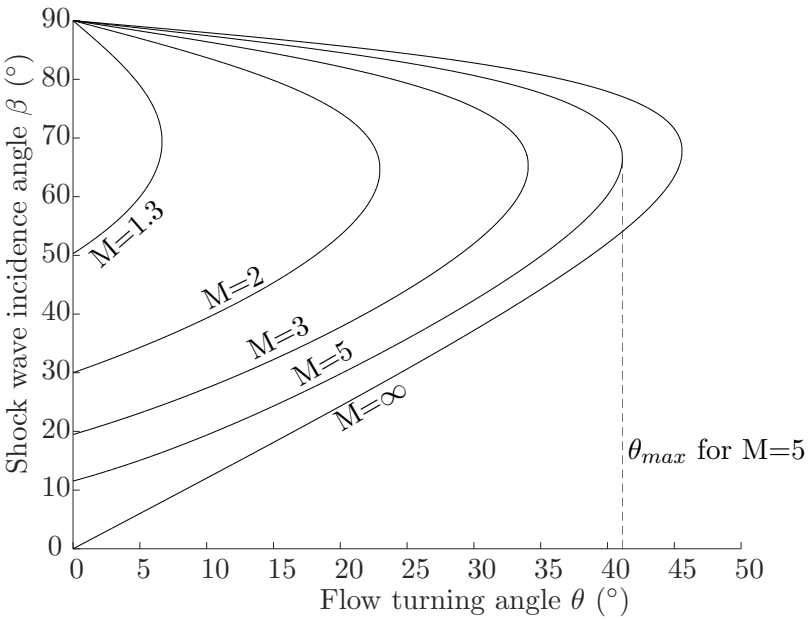

Figure 2.14: $\theta - \beta - M$ curves for various Mach numbers

However, there is limit that the flow can be turned termed, θ_{max}, which is to the right of the curves. Past this limit, Regular Reflection can no longer occur and the reflection topology will transition into Irregular Reflection. The different types of shock wave reflections that can be achieved are shown in Figure 2.15.

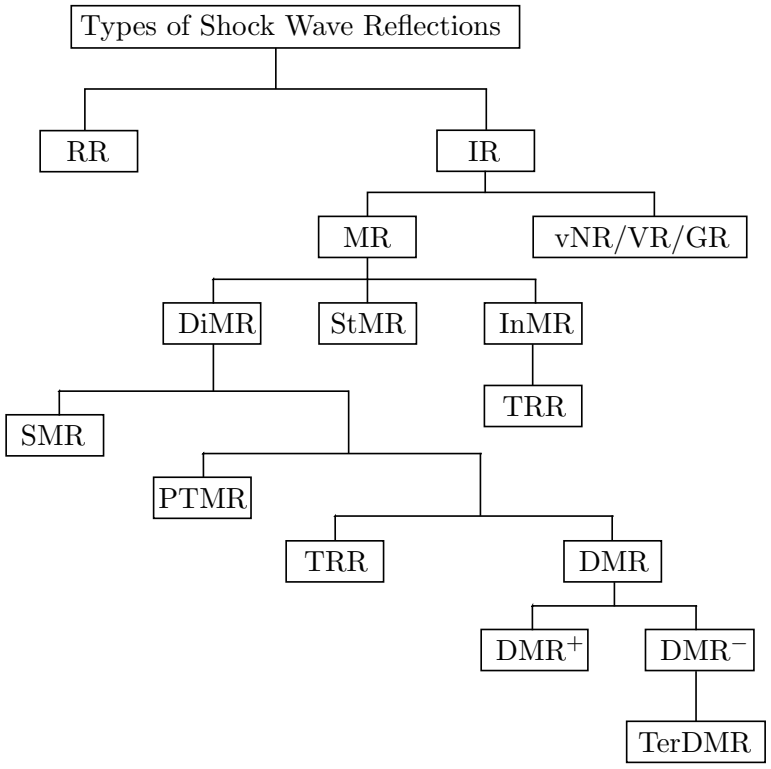

Figure 2.15: The 13 types of shock wave reflection patterns that can possibly occur [**10**]

It can be seen that there are many different types of Irregular Reflection. However, the Irregular Reflection patterns that are to be expected at low Mach numbers are Single-Mach Reflection (SMR) which falls into the Direct Mach Reflection category (DiMr) or von Neumann Reflection (vNR)/ Vasilev Reflection (VR)/Guderly Reflection (GR). It is expected from standard three-shock theory that Mach reflections will occur. The basic topology of Irregular Reflection patterns are shown in Figure 2.16.

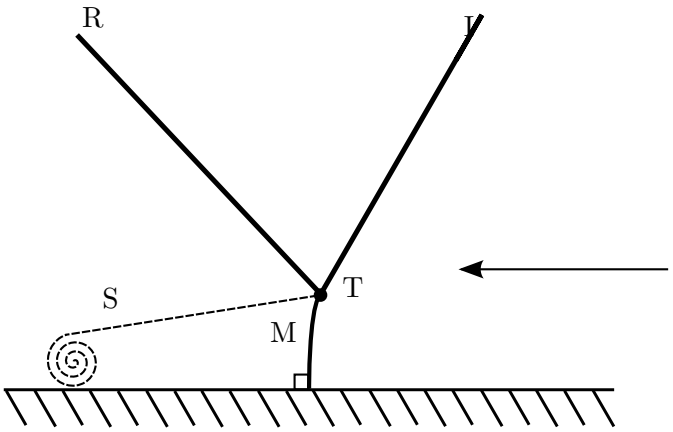

Figure 2.16: General Irregular Reflection in pseudo-steady reference plane

In this arrangement, the reflection point no longer lies on the reflection surface and follows a trajectory away from the material. For this to occur a third shock wave known as the Mach stem (M) forms. The Mach stem meets the incident (I) and reflected (R) shock waves. As there are three shock waves meeting at this point, the reflection point is called the triple point (T). A shear layer (S) forms in the region between the reflected shock wave and Mach stem. The shear layer is a mechanism to allow flows of different velocity magnitudes to align themselves in the same direction.

2.5 Theory of Shock Tubes

A shock tube is a simple piece of gas dynamic equipment used in the research of shock waves. The shock tube is simply a duct of constant cross-sectional shape and area [**11**]. Shock waves are generally created by separating the duct into two sections of different pressures using a gas-tight diaphragm mounted perpendicular to the axis of shock wave propagation. Keeping the duct cross section constant means that the shock wave will ideally not be attenuated (does not lose energy) with distance and the gas flow properties will remain constant over a region behind the shock wave [**12**]. A schematic of a generalised shock tube is shown in Figure 2.17.

The two sections of the shock tube are the driver section and driven section. A large pressure difference is created across the diaphragm by pressurising the driven section or creating a

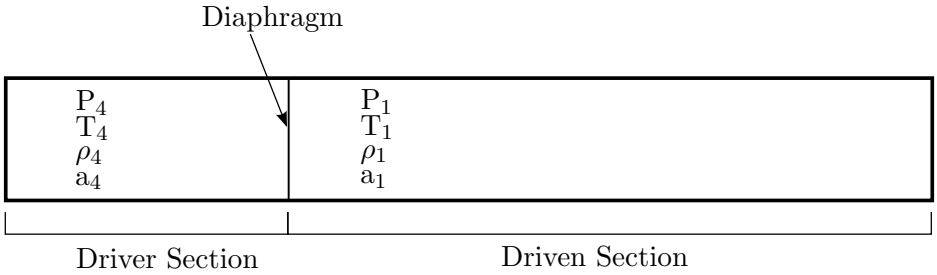

Figure 2.17: Simple shock tube configuration

vacuum in the driven section. Then by fast rupture of the diaphragm, propagation of compression waves form a controlled shock wave within a short distance. By the rupture of the diaphragm an expansion wave moves into the driver section and a compressive shock wave moves into the driven section.

The pressure vs. location diagram at a point before the diaphragm is ruptured is shown in Figure 2.18. A pressure vs. location diagram after diaphragm rupture is shown in Figure 2.19.

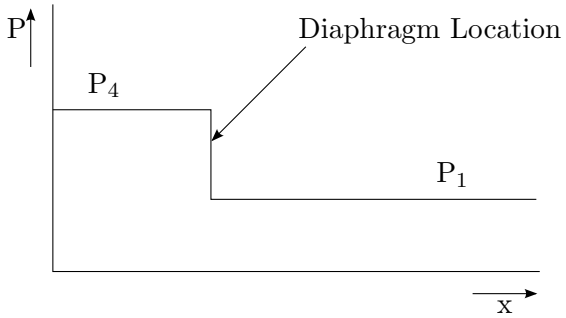

Figure 2.18: Pressure diagram before diaphragm rupture

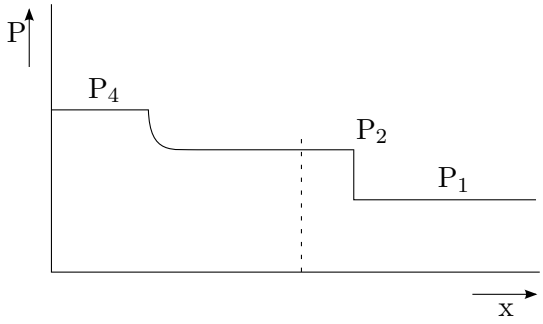

Figure 2.19: Pressure diagram after diaphragm rupture

The dotted line in Figure 2.19 is the contact surface. This is the gas that was originally at the diaphragm location. The fluid particles to the right of the contact surface are compressed and heated, while the fluid particles to the left are expanded and cooled.

Figure 2.20 depicts a wave diagram of the shock wave generation process.

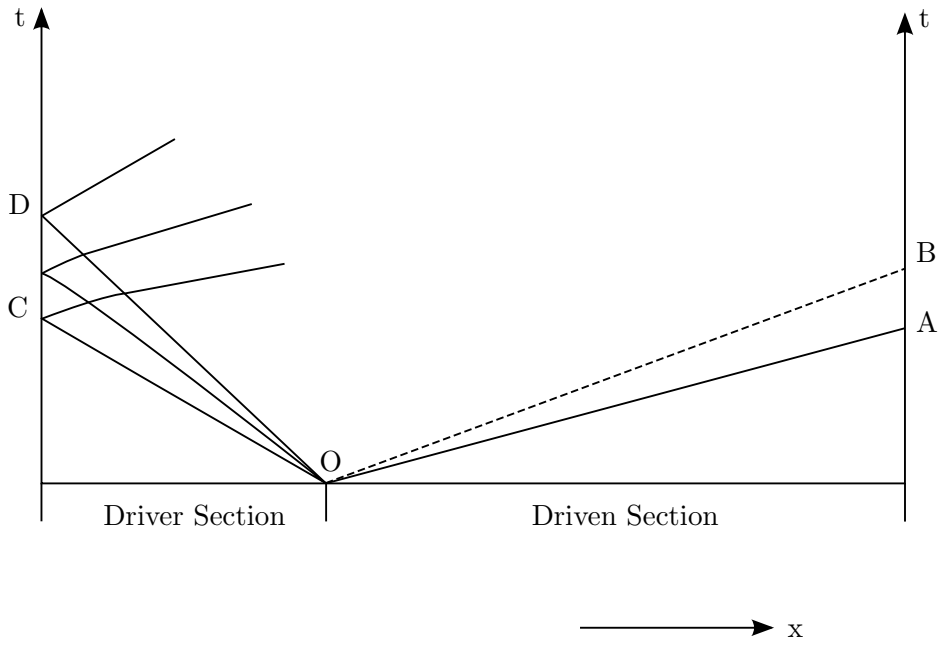

Figure 2.20: Wave diagram of shock tube operation

The line OA shows the trajectory of the shock wave into the driven section, while the line OB is the trajectory of the contact surface. These will reflect as expansion waves at the end of the tunnel as long as the end of the shock tube is open.

The line OC shows the head of the expansion wave travelling into the driver section and OD shows the tail of the expansion wave. These undergo reflection off the end of the driven section and reflect back down the shock tube.

The relationship for the pressures are given by Equation 2.15 [**12**].

$$\frac{a_1}{a_4}\frac{(1-\mu_0)(\frac{P_2}{P_1}-1)}{\sqrt{(1+\mu_0)(\frac{P_2}{P_1}+\mu_0)}} = \frac{2}{\gamma_4-1}\left[1-\left(\frac{P_0}{P_4}.\frac{P_2}{P_1}^{(\gamma_4-1)/2\gamma_4}\right)\right] \tag{2.15}$$

Using this formula with accurate pressure measurements the shock wave Mach number could be determined, however it is easier to record pressure spikes across a known distance and measure time between these pressure spikes to calculate the Mach number of the shock wave.

2.6 Real Flow Effects

There are a few limitations that are presented by the use of shock tubes. Due to viscous effects, there is attenuation of the shock wave during testing. This means it loses energy and subsequently the Mach number changes slightly during the testing. However, this effect is small and is usually disregarded. The affect of attenuation is neglected due to the short duration of a test, as typically a test will last between 0.5 - 0.7 milliseconds as the shock wave passes through the test section.

Secondly, under compression, the diaphragm bows as can be seen in Figure 2.21. The way that the diaphragm bows is not planar and so when it ruptures, the flow cannot be one-dimensional as the fluid particles are accelerating in a three-dimensional trajectory [**12**].

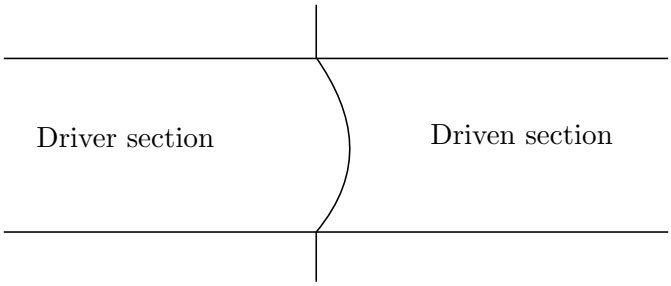

Figure 2.21: Diaphragm position before rupture

Figure 2.22 shows the diaphragm just after rupture. It can be seen that the pieces rupture in different directions. Therefore, transverse waves are created as the flow is being directed towards the walls of the shock tube instead of along its axis. Additionally the diaphragm pieces block the flow of the fluid initially and may travel down the tube a few metres before a well-defined shock wave is formed. To create a well defined shock wave it is suggested that the shock tube length is at least twenty times the width of the shock tube.

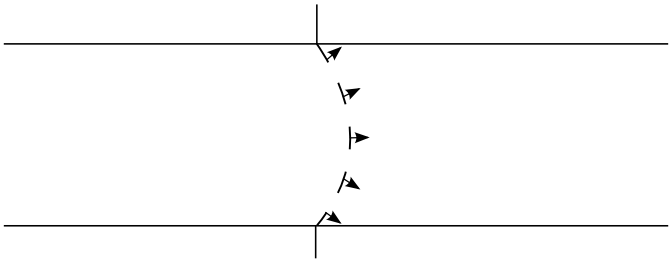

Figure 2.22: Point of diaphragm rupture

2.7 Flow Visualisation

Schlieren photographic methods are primarily used to visualise gas dynamic systems in order to represent the shock waves and any other patterns created by the reflections. Schlieren principles rely on the refractive properties of gasses. The refraction of light is based on the relative density of the gas. Due to the high discontinuity in density at a shock wave, this is an effective way to visualise the flow system.

This method is beneficial as the visualisation equipment does not interfere or impede the flow of the fluid. These methods are superior to probing methods such as Pitot tubes, as a Pitot tube will change the local flow properties where it is contact with the flow. Additionally shock wave reflections will occur off the Pitot tube. Therefore, a pitot tube will severely alter the downstream conditions.

Schlieren photography will produce an image where the change in the refractive index of the fluid is proportional to the change in the density of the fluid. For the testing proposed, shadow photography will be used, as only the shock waves and reflection topology needs to be visualised to measure reflection angles. The density gradients do not need to be accurately known. Shadow photography works in the same manner, however unlike Schlieren photography, the change in density is proportional to the derivative of the gradient in refractive index [**13**].

The optical configuration to be used is shown in Figure 2.23, which is known as a Z-configuration.

The elements of the optical set up are:

- Light source
- 2 converging lenses
- Knife edge/Iris
- Cylindrical lens
- 2 parabolic mirrors
- Camera

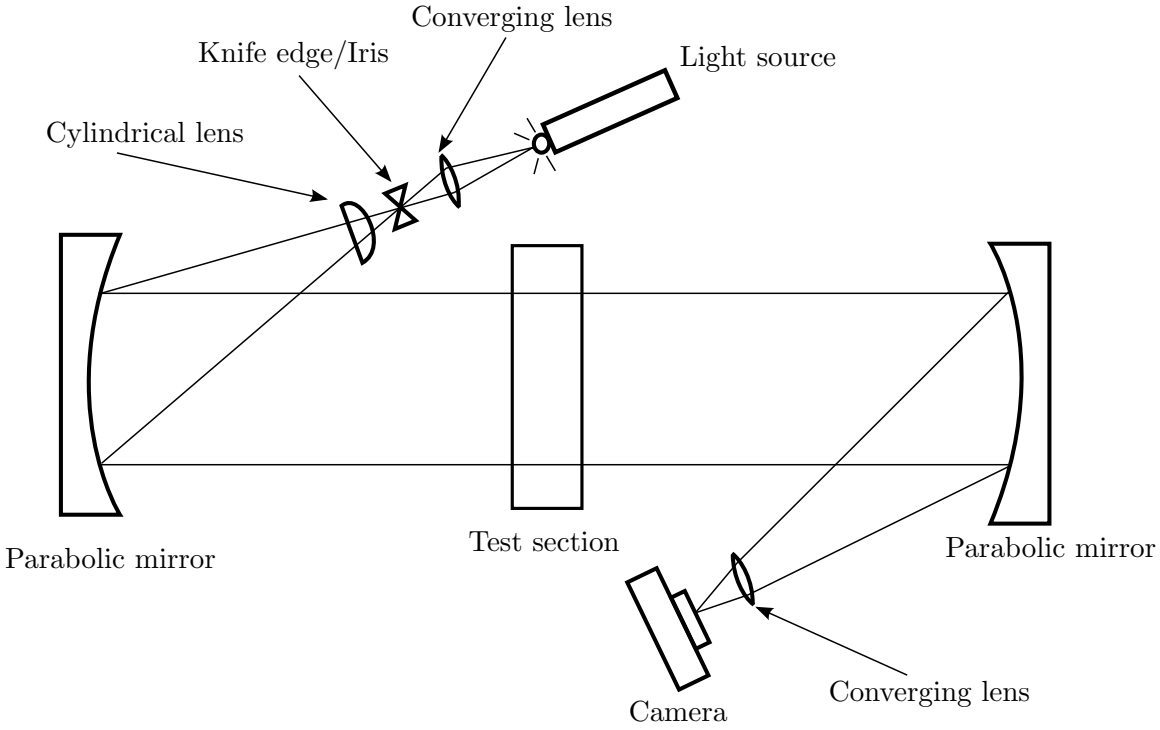

Figure 2.23: Z-configuration shadow photography set up

The path of the light is as follows. The light source produces light that is focused by the first converging lens, on to the knife edge or through an iris placed at the focal length of the parabolic mirrors. This is done to create a point source of light and to eliminate excess light created by the light source that may affect the photograph. The light passes through the cylindrical lens, this lens is used to make sure the aspect ratio of the beam is 1, so that there is no distortion in the vertical and horizontal planes. The light then reflects off the first parabolic mirror. The light paths leaving this mirror are now parallel to each other and perpendicular to the test section. These light paths pass through the test section, if there is a change in density based on the presence of shock waves or other gas properties, the parallel light paths will be diffracted creating shadows. The light then reflects off the second parabolic mirror and is focused through the second converging lens onto the CCD screen of the camera. This is done to reduce the amount of space required for the optical set up. The shadows seen in the photographs represent the location of shock waves when the light source is activated.

2.8 Boundary Layers

Viscous and thermal boundary layers are thought to account for a significant effect in the shock wave reflection topology, therefore a brief introduction into each is given below.

2.8.1 Viscous Boundary Layers

Hydrodynamic viscous boundary layers are the result of real fluid properties in fluid flows, close to a body in the flow.

In general fluid dynamics, the fluids are taken to be perfect fluid. These are frictionless and incompressible, which means that there are no tangential forces, or shearing stresses, acting between layers or streamlines of the fluid. This is an adequate assumption for flows that are distanced away from a body within the flow as only normal pressure forces are accounted for. However, close to the body, the fluid offers internal resistance to the change in shape of the fluid volume. This in turn accounts for the drag of the body of the flow. This is a real fluid effect, whereas in a perfect flow, a body moving through a fluid would experience no drag [**14**].

In a perfect fluid that is frictionless, the fluid is allowed to "slip" past the body therefore inducing no drag. However, in a real fluid, there are molecular attractions between the fluid and the body. This leads to the no-slip condition where, the fluid particles match the velocity of the body along the surface of the body. The fluid must reach the far field velocity at a certain distance away from the body, this means that shearing stresses are set up within this layer of fluid. This is the viscous boundary layer in the fluid and is shown in Figure 2.24.

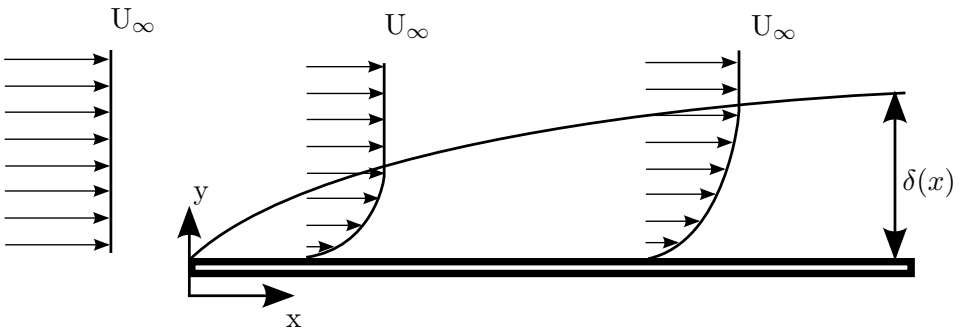

Figure 2.24: Boundary layer formation on a flat plate in a moving fluid flow

Where: U_∞ is the free stream velocity and δ is the boundary layer thickness.

The viscous boundary layer grows based on the location from the leading edge of the plate. It will transition from a laminar boundary layer to a turbulent boundary layer based on

Reynold's number.

Another effect of a viscous boundary layer is the small displacement of the outer streamlines away from the wall of the body. This is present to satisfy the conservation of mass between the incoming flow and outgoing flow. This is known as the displacement thickness and is denoted δ^*. In an inviscid case this would mean moving the flow away from the wall by this distance [**15**]. This effect is shown in Figure 2.25.

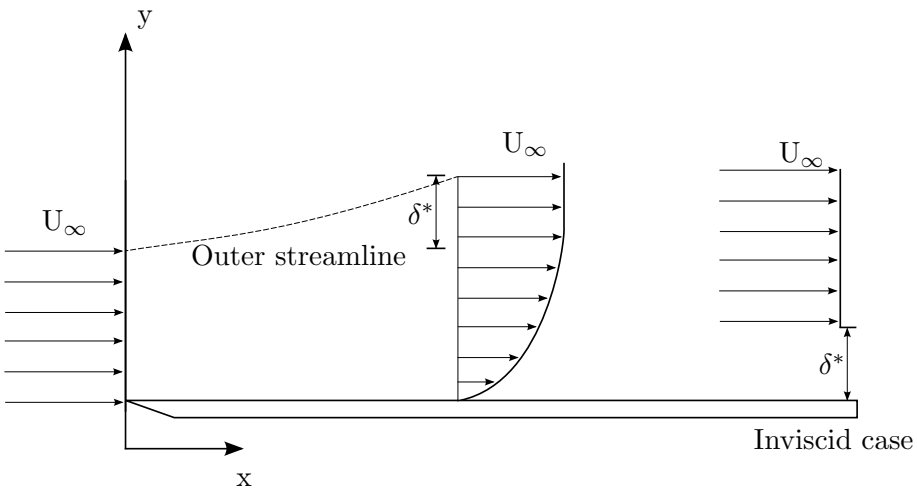

Figure 2.25: Effect of displacement thickness in a boundary layer

The case where a shock wave impacts on a plane wedge is shown in Figure 2.26 with the associated fluid velocity distribution behind the reflected shock wave.

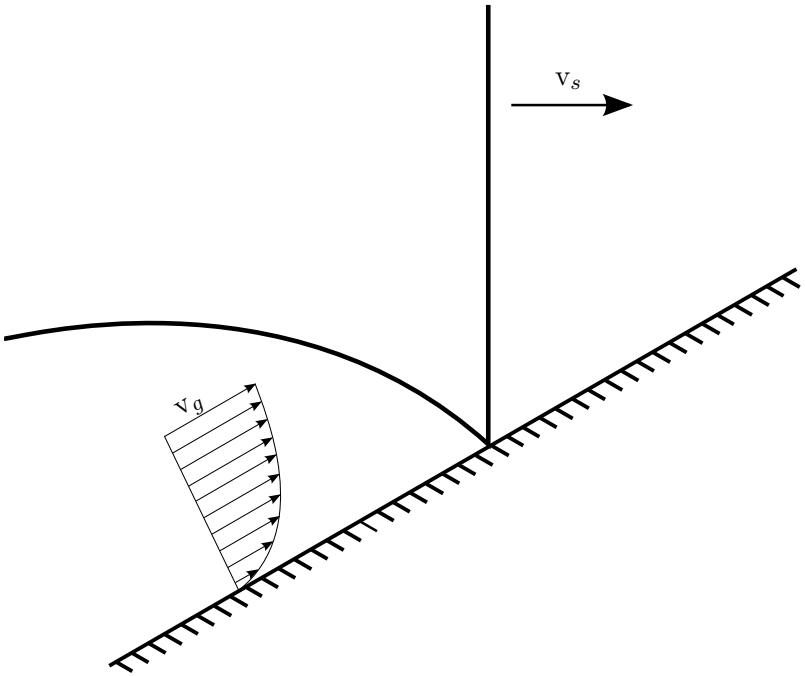

Figure 2.26: Wall-shock wave interaction with associated velocity profiles

The shock wave is travelling towards the wall at a velocity of v_s. After the reflected shock the fluid has a velocity of v_g which follows the same velocity distribution as can be expected for a boundary layer, as the no-slip condition must be satisfied. For a surface to be considered hydraulically smooth, where viscous boundary layers are assumed insignificant, the surface roughness of the reflecting surface must be below 50 microns [**10**]. Further discussion of the viscous boundary layer effects will be addressed in section 2.9.

2.8.2 Thermal Boundary Layers

Thermal boundary layers are similar in nature to viscous hydrodynamic boundary layers. In a fluid flow, where a solid and fluid are at different temperatures, there is heat transfer between the two materials by conduction. This conduction is present as the fluid at the wall is stationary due to the no-slip condition [**16**]. The heat transfer will occur due to the thermal conductivity of the material. The heat transfer will occur at a flux rate as shown in Equation 2.16.

$$q = k\Delta T \tag{2.16}$$

Where:

- q - Heat flux density [W/m^2]
- k - Thermal conductivity [W/m.K]
- ΔT - Temperature gradient [K/m]

It is assumed that the fluid travelling behind the reflected shock wave is isothermal (for the short duration of the shock wave passing over the test piece) at a temperature higher than the ambient original flow conditions ahead of the initial shock wave (room temperature). Therefore, the fluid will be at a constant temperature higher than the reflection surface, however due to conduction of heat into the wall, the reflection surface can no longer be assumed to be adiabatic.

This is a disagreement with traditional two-shock theory, as theory assumes that the reflection process is totally adiabatic and that all reflection surfaces and fluids are non-conductive for the duration of the testing. However, in reality there should be a smooth temperature gradient into the material as far-field conditions are met, similar in structure to a viscous boundary layer.

This disagreement between theory and reality has been suggested to have an effect on the reflection process. Based on the thermal conductivity the rate of heat transfer may affect the

reflection angles of the reflected shock waves as energy is transferred from the fluid into the material.

2.9 Previous Work

In their work, Hornung and Taylor, experimentally proved that the transition from Regular to Mach reflection of strong shock waves is significantly influenced by the viscosity of the fluid [**17**].

Figure 2.27 shows the shock wave reflection process in the transient flow with the dotted line representing the displacement thickness of the outer streamlines.

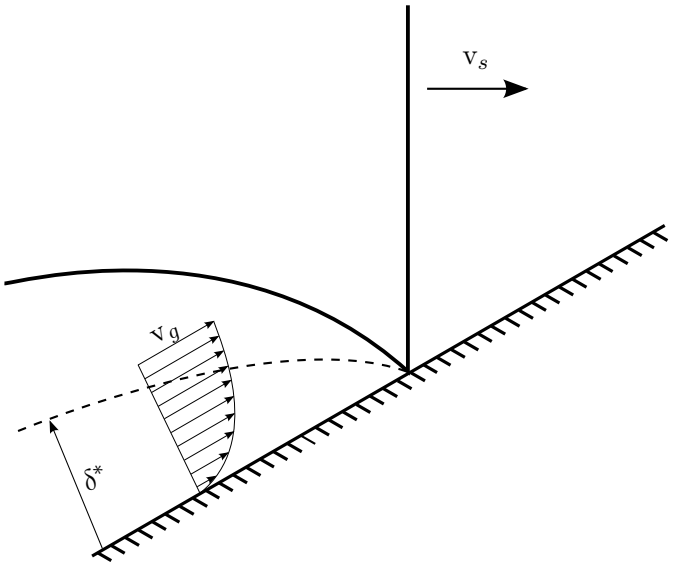

Figure 2.27: Transient wall-shock wave interaction

Thereafter, performing a Gaussian transformation to bring the case into a pseudo-steady reference frame the reflection process will occur as in Figure 2.28. Here the fluid travels towards the stationary incident shock wave at a velocity of v_s and the fluid moves away from the reflected shock wave with a velocity profile shown. The shape of this velocity profile is due to the wall moving faster than the fluid and there will be shearing of the fluid due to the no-slip condition.

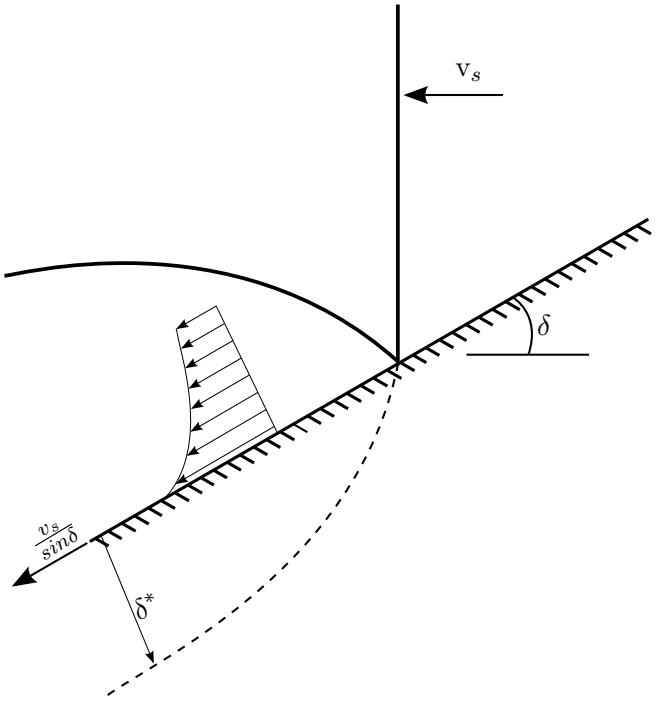

Figure 2.28: Pseudo-steady wall-shock wave interaction

In this case, the displacement thickness must be negative as is shown in the figure, and is directed into the reflection surface, to satisfy mass conservation.

The negative displacement thickness therefore acts as a mass sink. In an inviscid pseudo-steady analogue this would be represented as a displaced wall, which creates a fan of characteristics to produce the reflected shock wave as is shown in Figure 2.29.

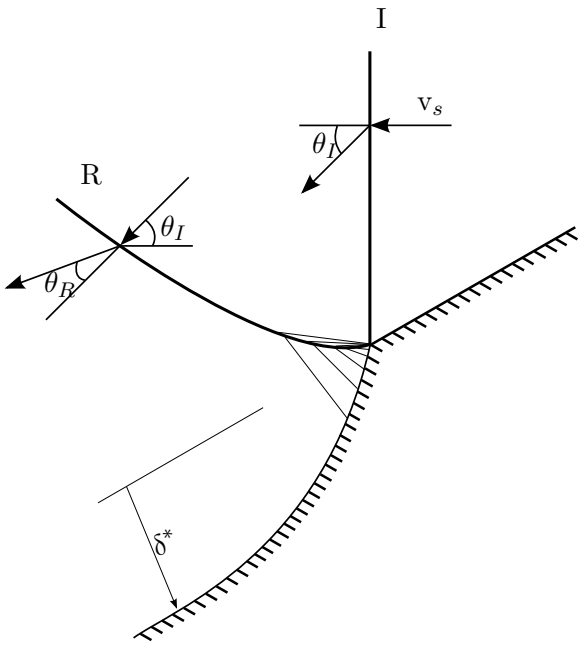

Figure 2.29: Pseudo-steady inviscid analogue wall-shock wave interaction

The effect of viscosity on the displacement thickness thus alters the flow deflection angle such that:

$$\theta_R \neq \theta_I$$

This changes the reflection angle based on the $\theta - \beta - M$ relation. The viscous boundary layer that is created is dependant on many different flow conditions and is highly non-linear in the fully turbulent case. Fluid viscosity, surface roughness of the reflection surface and Reynold's number are some of the major contributors to the development of the viscous boundary layer [**18**].

Van Netten, Dewey and von Haimberger investigated the effect that surface temperature of reflections surfaces had on the shock wave reflection process [**19**]. They concluded from their experiments that changing the temperature of the wedge with respect to the ambient temperature created reflection topologies that were not self-similar. This was due to a boundary layer being produced and introduces a length scale into the experiment.

By cooling the wedge with liquid nitrogen and heating it with a blow torch, the trajectory of the triple point changed in the Mach reflection cases for the different temperatures. It also altered the shape of the Mach stem to be non-perpendicular to the wedge. In the cases where the wedge was cooled, the Mach stem was tilted forward to a maximum of 8°. It was thought that the non-perpendicularity was due to energy being taken away from the flow when the wedge is cooled.

When Helium was used (to change the speed of sound), non-perpendicularity was not observed, leading to the assumption that the effects were mainly due to conduction of heat rather than the thermal boundary layer itself.

The results from this experimentation are considered to be erroneous as the cooling was performed by pouring liquid nitrogen into a channel below the surface of the material and heating was performed using a blow torch as uniformly as possible. Both these methods could not ensure that heating and cooling of the wedge was performed uniformly and that the test pieces were completely isothermal up to the point at which the test was run. There was the possibility of buoyancy effects at the surfaces due to the differential heating and cooling of the surfaces before the tests could be run.

Henderson, Crutchfield and Virgona investigated, numerically, the effect of thermal conductivity and viscosity of argon gas when shock waves diffracted over rigid ramps [**20**]. Although the study was primarily based on the transition between regular and Mach reflection, important results were found in the boundary layer of the fluid close to the reflection surface. The initial temperature of the system was set at 293.15 K which corresponded to the

isothermal surface of the ramp. After the shock wave interaction the maximum temperature was increased to 1400 K. It was seen that due to the isothermal surface, there was significant cooling of the gas close to the ramp surface, with an increase of density of a factor greater than 4. This work performed numerically was the basis for the purpose of the study presented in this dissertation, to experimentally determine the effects of thermal conductivity.

2.10 Earlier Experimentation, Results and Conclusions

The experimentation referenced in section 1.1 will be further discussed in this section. The work was performed in the Michael Seitz automated shock tube at the University of the Witwatersrand, using glass and copper test pieces with a test apparatus that allowed the test piece incidence angles to be altered. Glass and copper were used for their large differences in thermal conductivity.

The test pieces were set within hydraulic smoothness limits by polishing and verification of the surface roughness. High speed shadow photography was used to visualise the reflection topologies at different stages during the test.

The results from the experimentation showed that the reflection topologies were not entirely pseudo-steady as the reflection patterns were not self-similar in time. The images were analysed with Autodesk Inventor 2014 Computer Aided Design Package to measure the reflection angles. The angles measured at an earlier stage in each test were found to be different than at a later stage in the test. This lack of self-similarity, was a confirmation of the results presented by van Netten et al. It was noted that in all cases the reflection angle at the glass test piece was slightly larger than at the copper test piece.

Qualitative results were based on the symmetry present in the reflection patterns propagating into the space between the two test pieces. There was asymmetry noticed in the images, which was a positive result in the testing.

It was concluded that repeatable results were obtained and that the thermal conductivity of the walls influence the shock wave reflection topology. However, the indications are small due to the scale of the experiment. The resolution of the imaging equipment limited the accuracy of the results [**21**].

Chapter 3 Objectives

The objectives of this study of thermal conductivity effects in shock wave reflection are:

- To investigate the effect of reflection surface thermal conductivity on the reflection topology of shock waves.
- To analyse the reflection topologies of various materials with set surface roughness's, at varying wedge angles and incident shock wave Mach numbers (within reproducible range of the Large-Scale Diffraction Shock Tube (LSDST)).
- To compare theoretically and experimentally attained shock wave reflection angles to determine the accuracy with regards to two-shock theory.
- To identify if the behaviour is consistent within the Irregular and Regular reflection domains.
- To analyse the images quantitatively and qualitatively to determine the effects of thermal conductivity of the reflection materials.
- To validate or revoke experimental results and conclusions found in undergraduate study.

Chapter 4 Apparatus

4.1 Introduction

Experimental testing was performed in Room F7, in the North West Engineering building located on the East Campus of the University of the Witwatersrand. Testing was performed using an existing shock tube already in place with modifications made to the shock tube to improve both the safety of operation as well as repeatability of the experimentation as is outlined in section 4.2. This chapter outlines the test rig design, the shock tube facilities as well as the instrumentation used in the experimentation.

4.2 Shock Tube

The Large Scale Diffraction Shock Tube (LSDST) was used for the experimental testing for this dissertation. The shock tube is a modular design of a driver section, driven tunnel and test section.

The driver section is made up of a cylindrical pressure vessel 2010mm long and a diameter of 500mm with wooden inserts mounted on a rail with wheels. The wooden inserts are to reduce the volume of air required at higher pressures, whilst still maintaining the pressure required to generate shock waves. Additionally the wooden inserts create the same cross-section as the driven tube. The wheels and rails allow for the driver to be separated from the driven section so that diaphragm can be loaded and removed for each test. The driver is attached to the driven section by 15, M24 bolts at a flange connection.

The driven tunnel is rectangular in shape and has internal cross section dimensions of 450×100mm with the height being the larger dimension. The tunnel is constructed with 20mm thick steel in order to provide support under the pressure loads as well as mechanical support in bending over the large lengths of the tube. The driven tunnel is separated into

3 lengths of 2m joined with rectangular flanges. The first of two ports is located 4.9m from the connection between the driver and the driven tunnel The ports have a spacing of 50mm allowing pressure transducers to be used in order to calculate the shock wave speed and Mach number.

The driven tunnel is connected to the test section with a rectangular flange connection and 10, M14 bolts. The test section is a large rectangular section with the following internal dimensions: width of 100mm, height of 1960mm and length of 2000mm. There is a channel placed within the test section in order to limit the area where gas flow can occur to maintain the dimensions of the driven tunnel. There is a muffler located at the rear of the test section in order to reduce shock wave strength as it is vented into the testing venue. This is a safety precaution as well as to reduce the operating noise of the shock tube.

There are circular plates forming the side walls of the test section with two holes for the placement of optical windows available in each plate. Each of these holes has a diameter of 351mm. The plates are able to rotate in order to visualise any area within the area of these two large plates. During testing the plates are secured in place with 24 cap screw secured locks on each plate.

For testing the two central holes were sealed with steel plate assemblies. The two outer holes housed the optical window assemblies in order to visualise the flow conditions during the testing. These are sealed using BK-7 Glass within steel frame assemblies. The allowable viewing area within the frames has a diameter of 317mm.

All sections of the shock tube are mounted on wheels to allow them to be transported easily. However, during testing all sections are raised off their wheels and secured on blocks to prevent the shock tube from moving during a test.

A schematic of the shock tube is shown in Figure 4.1 below.

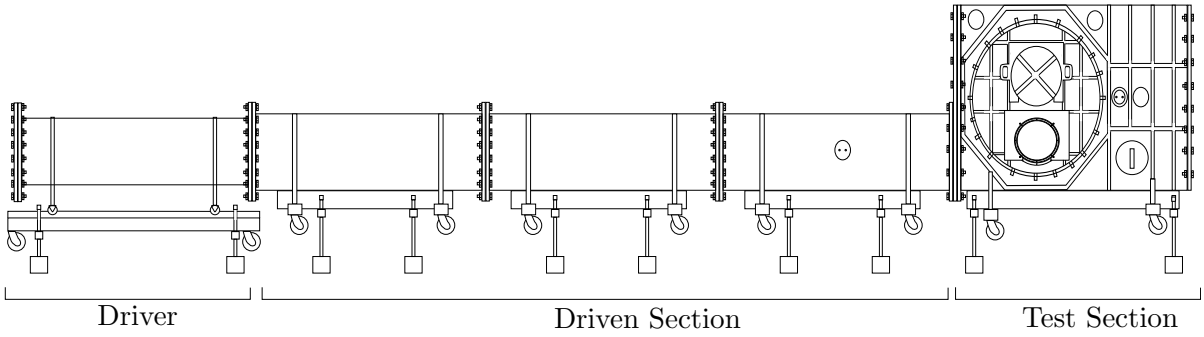

Figure 4.1: Schematic of Large Scale Diffraction Shock Tube assembled and raised off the ground

4.2.1 Shock Tube Repair and Safety Measure Design

During testing procedures in 2015 an incident occurred where the bolted connection holding one of the viewing windows and window frame, failed. This led to the window and frame being expelled from the test section, with the window breaking against a stand holding a parabolic mirror.

The frame to hold the window was redesigned in order to increase the safety of operation of the shock tube. The frame is now held in place using 6, M10 studs and bolts, with 4, M12 bolts attached through slots in steel angles welded to the shock tube. These M12 bolts will act as a catching mechanism in the event of the studs failing. This will allow the pressure to be released, whilst preventing the window from falling and damage. The engineering drawings for the new mounting design can be found in Appendix D

4.2.2 Diaphragm Pneumatic Pricker

In previous testing a spring loaded sharpened pricker was used to burst the diaphragm at predetermined pressures. This system was found to be ineffective, as the release mechanism would occasionally let go early and an early burst would occur, additionally this mechanism was prone to sticking and would delay the bursting process. This meant that the bursting of the diaphragm was not accurate and reproducible over a large number of tests.

A new pricker system was designed in order to increase the accuracy and reproducibility of the bursting of the diaphragms at set pressures. The new pricker is actuated using a pneumatic cylinder with a sharpened rod. Drawings for the pricking system can be found in Appendix D.

4.3 Test Rig

The main focus of this research was to test two materials at the same incident angles with the same Mach numbers. This was achieved by designing a test rig that could accommodate two different test pieces in the shock tube simultaneously.

4.3.1 Test Rig Description

The test rig is made up of seven main assemblies: a support structure, two adjustable spacing arms, two sliding mounts and two test piece assemblies.

The support structure is made up of 20mm mild steel plates that allow for the structure to be mounted within the shock tube as well as provide structural rigidity during testing. The plates are machined and use bolted connections for easy production and assembly. 45° braces are used in order to provide support for the rear mounting plate under loading from shock waves. A separate spacing plate is used at the bottom of the support structure in order to provide a base against the bottom of the shock tube, without firmly attaching it. This also restricts the structure from flexing during testing. Parts of this structure form mounting points for the sliding mounts and spacing arms. These mounting points connect to the sliding mounts and spacing arms using pins that are specified as interference fits in order to reduce backlash whilst still allowing the angle of the test pieces to be changed for different conditions. An isometric view of the support structure is shown in Figure 4.2.

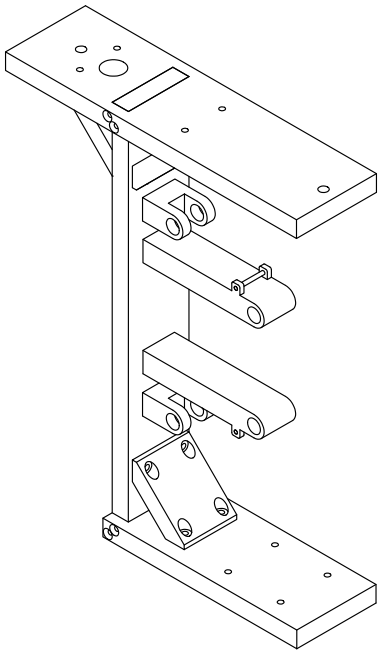

Figure 4.2: Isometric view of the support structure

The spacing arms are used in order to alter the angle of the test pieces to the incoming flow. These are made up of mounting blocks which allow attachment to the sliding mounts and the support structure again with pins that are specified as interference fits. These are connected to each other with threaded rods and a collar. Each spacing arm has a left and a right-threaded rod. This allows adjustment of the angle by rotating the collar to extend or retract the spacing arms allowing the sliding mount to rotate about the mounting point on the support structure. The collar is locked in place on each end by two locking nuts to provide rigidity and to eliminate backlash during a test. An isometric view of a spacing arm is shown in Figure 4.3.

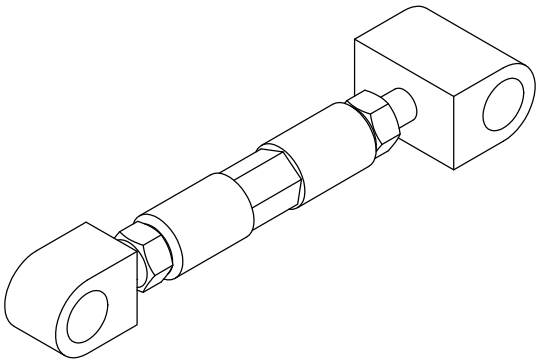

Figure 4.3: Isometric view of a fully assembled spacing arm

The sliding mounts are made up of two, sliding brackets with threaded holes attached together using interference fitted pins. The threaded holes are used to adjust the position of the leading edge of the test pieces by tightening one end and doing the opposite on the alternate side. This is essential so that accurate results can be achieved in the experiment as shock waves will encounter the leading edge of both test pieces simultaneously. An isometric view of a sliding mount is shown in Figure 4.4.

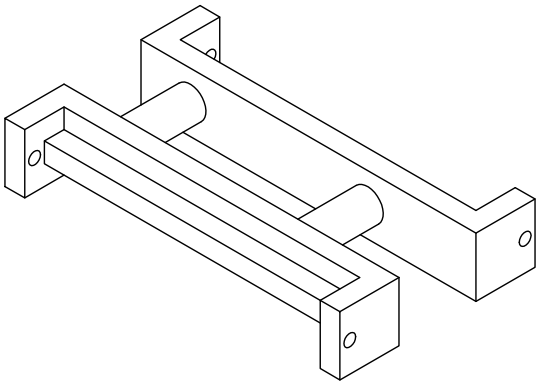

Figure 4.4: Isometric view of a fully assembled sliding mount

The test piece assemblies are made up of two sliders which are able to slide on the sliding mounts allowing the test piece leading edge location to be adjusted and then secured. These are attached to mounting blocks via pins with an interference fit. These blocks are produced with a dovetail profile to allow accurate mounting to the test pieces and to provide support to the test pieces during testing. On each assembly there is a spring pin. This pin allows a spring to be attached with a spring pin located on the main support structure. This is used in order to remove any backlash in the assembly during the testing procedures. A description of the test pieces is given in subsection 4.3.2. An isometric view of a test piece assembly is shown in Figure 4.5.

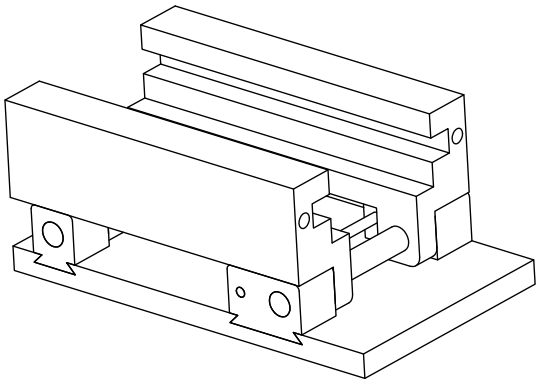

Figure 4.5: Isometric view of a test piece and mounting assembly

An isometric view of the entire test rig assembly (without fasteners and springs) is shown in Figure 4.6. Additionally, engineering drawings and Computer Aided Design files of the test rig design can be found in Appendix D.

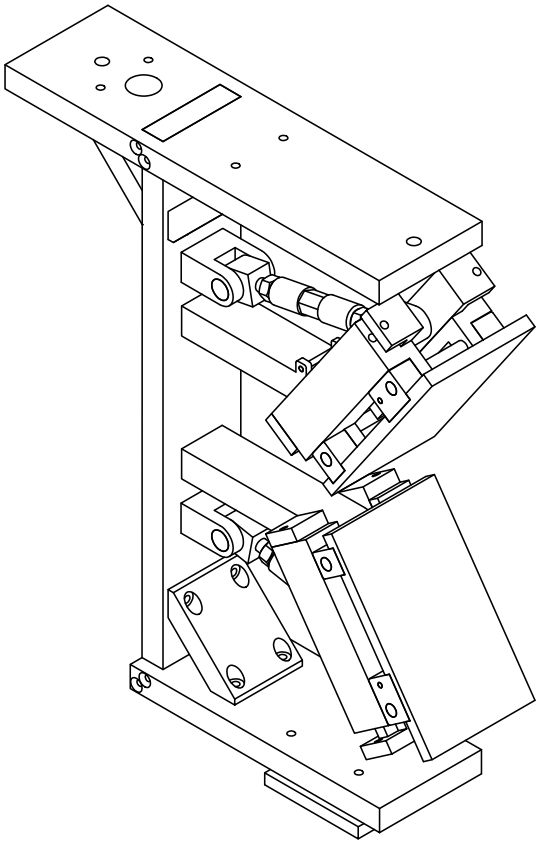

Figure 4.6: Isometric view of the fully assembled test rig

4.3.2 Test Piece Description

The test pieces are made of various materials with different thermal conductivities as shown in the Table 4.1.

Table 4.1: Materials used and their Thermal conductivities [**22**]

Material	Thermal Conductivity (W/mK)
BK-7 Glass	1.13
Copper	401
Mild Steel	43
Brass	109
Aluminium	205

The test pieces are all 170mm long, 99mm wide and 10mm thick. This represents a length that is 2.125 times larger than in previous experimentation. This will allow a longer time in which any thermal effects may affect the reflection process.

The mounting of the test pieces is achieved by using an epoxy adhesive to secure the mounting blocks to the test piece. The metal test pieces have dovetail profiles machined into them in order to provide an accurate and secure location of the test pieces. Due to the difficulty in machining glass, the glass test piece is located using a rectangular profiled mounting block slotted in to the side. This still provides an accurate location that is slightly less secure than a dovetail profile. The engineering drawings of the test pieces may be found in Appendix D.

The metal test pieces were polished at Airbus Defence and Space, Optronics division in Irene, Pretoria, to ensure that surface roughness and viscous boundary layers are not affecting the reflection patterns between the different materials. Surface roughness tests were performed in the direction of shock wave propagation, to check that all material specimens are hydraulically smooth in the Metallurgical Engineering laboratory at the University of the Witwatersrand.

Five values of average surface roughness (R_A) along a 12.5mm sample length, were taken on each test piece and the results from these tests can be found in Table 4.2. These results are averaged to provide an average roughness over 62.5mm of each test piece in varying locations.

Table 4.2: Material surface roughness

Material	BK-7 Glass	Copper	Mild Steel 1	Mild Steel 2	Brass	Aluminium
Test 1 (μm)	0.009	0.264	0.141	0.171	0.438	0.367
Test 2 (μm)	0.017	0.214	0.094	0.164	0.733	0.320
Test 3 (μm)	0.015	0.439	0.310	0.155	0.497	0.275
Test 4 (μm)	0.033	0.322	0.109	0.143	0.584	0.286
Test 5 (μm)	0.007	0.272	0.167	0.154	0.568	0.296
Average (μm)	0.016	0.302	0.164	0.157	0.564	0.309

From these results it is evident that the test pieces are well below the limit of hydraulic smoothness in shock wave testing, thus having no effect on the shock wave reflection topology [**10**].

4.3.3 Test Rig Constraints

Due to the design of the Large Scale Diffraction Shock Tube test section windows, certain design choices of the test pieces were made in order to offer the longest possible test piece whilst allowing a large enough range of incidence angles to be tested with one test rig set-up. The 170mm long test pieces are able to be set at angles ranging from 0°-55° relative to the

longitudinal plane of the shock tube. This allows a range of shock wave incidence angles varying from 35°-90°. With this range of incidence angles it is possible to test for cases that are in both the Regular and Irregular Reflection domains, whilst increasing the length of the test pieces from previous studies.

4.4 Pressure Transducers and Oscilloscope

The pressure transducers and oscilloscope are used in order to determine the Mach number of the shock wave. This is done by calculating the speed of sound, using a thermometer in the laboratory for each test and Equation 2.3. The transducers are known to be 50mm apart, and using the oscilloscope, the time taken for the shock wave to traverse this distance can be measured. This measurements are recorded in spikes of voltage from two channels on the oscilloscope, corresponding to the two pressure transducers. Thereafter the shock wave velocity (V_s) is known and the shock wave Mach number (M_s) can be calculated using equation Equation 2.4.

4.5 Optics

For visualising the reflection process over the different materials, a standard Z-configuration shadowgraph (depicted in Figure 2.23) set up was used to view the flow field. The light source is a white light with an exposure time of 1.5 microseconds. Glass acromat lenses were used to obtain the focusing of the light as was needed. The following focal lengths were used for the lenses:
80mm Effective focal length on the light source side of the test section.
160mm Effective focal length on the camera side of the test section.
All instrumentation and their respective details used in the testing can be found in Appendix A.

Chapter 5 Methodology

The procedures for performing any test on the Large-Scale Diffraction shock tube are set out below:

5.1 Pre-Test Check List

The following procedure is performed at the beginning of each testing day, in order to check if the equipment is operational and safe to use.

1. Walling downstream of shock tube exhaust undamaged (excludes minor scratches, chips etc.).
2. Shock tube clear of debris and other loose materials.
3. Muffler fitted to shock tube exhaust.
4. Lateral barriers placed at exhaust of shock tube.
5. Downstream barrier placed at exhaust of shock tube and casters locked.
6. Test section window frames secure.
7. Supply valve and connection inspected for leaks.
8. Supply hose inspected for leaks or other damage.
9. Supply hose is not twisted or severely bent.
10. Control panel valves and connections inspected for leaks.
11. Driver free of loose materials and undamaged.
12. Driver gaskets in good condition.
13. Driver closing nuts and bolts in good condition.

14. Whistle available and in working order.
15. All required personal protective equipment (PPE) [vibration-damping gloves, hearing protection, goggles] present and in good condition.
16. User headlamps present and in working order.
17. Instrumentation cabling secured off floor of working area.
18. Venue is clear of all unauthorised personnel.
19. Magnetic interlocks and test lights have been enabled.

5.2 Testing Procedure

The following procedure is the order of events followed in order to run a successful test. It has been amended slightly from the Large-Scale Diffraction (450mm) Shock Tube testing procedure (LSDST-01) in order to apply specifically to the tests performed.

1. Workshop air receiver must be charged to supply driver of shock tube.
2. Before any given day's testing the pre-test inspection (LSDST-04) must be made and signed by the first operator for the day.
3. Switch on all instrumentation.
4. Set the test pieces at the required angle using the adjustment collars and secure with the securing nuts.
5. Fit and tighten test section windows to the shock tube.
6. Close all valves on control panel except ball valve for driver venting.
7. Open pressure line for both the driver and wrench/pricker pressure circuits.
8. If a flow visualisation is set up and the xenon lamps are being used as the light source these must be switched to external mode, i.e. must not flash repeatedly.
9. Ensure the diaphragm pricker is fully retracted.
10. After greasing the top and bottom of the diaphragm material (to improve sealing and to secure it for closing the driver), fit a new, undamaged diaphragm sheet across the inlet to the expansions section.

11. Ensure that fingers and limbs are not in the diaphragm clamping area of the tube and then close driver slowly and carefully from the rear.

12. Loosely fit all driver securing nuts manually.

13. Open torque wrench ball valve.

14. Using the supplied pneumatic wrench and P.P.E. (vibration-damping gloves, goggles, visor and hearing protection), tighten the driver securing nuts in the sequence labelled on the driver flanges i.e. 1-1-1, 2-2-2, 3-3-3 etc. as per the driver clamping procedure (LSDST-03).

15. Close torque wrench ball valve.

16. Switch on operator headlamp and switch off test area lights.

17. The oscilloscope must be triggered on (must say "waiting for trigger") and the delay time must be input on the delay box and the delay box armed.

18. Hearing protection as provided must be worn by all persons inside the testing room from this point on until the end of each test. Check that no unauthorised persons have entered the venue and that interlocks are still active.

19. Close the driver vent ball valve.

20. The control globe valve must be opened slowly to pressurise the driver section. Sound the siren at approximately half the required driver pressure to alert persons outside of the venue of the impending test in case of a premature burst.

21. Close the driver ball valve once the required driver pressure has been attained.

22. Sound the siren again and wait 3-5 seconds before opening pricker cylinder supply ball valve to actuate the pricker. If flow visualisation is required, the operator headlamp must be switched off and the camera hand trigger must be closed and held closed until the blast can be heard.

23. The operator headlamp must be switched on and the panel supply globe valve immediately closed.

24. The driver vent ball valve must be opened to allow remaining air in the driver to be vented.

25. Switch on test area lights.

26. Close the pricker cylinder ball valve and open the pricker cylinder vent ball valve. The pricker should retract and reset to its original position. Close the pricker vent ball valve.

27. Loosen the driver section securing nuts as per the driver clamping procedure (LSDST-03).
28. Remove the loosened nuts manually and open the driver by pushing it slowly and carefully at the rear.
29. Remove and dispose of the burst diaphragm.
30. Fill out required sections of test log.

5.3 End of Day Check List

The following operations are performed at the end of each day's testing and signed off by a duly authorised responsible person:

1. Workshop supply valves closed.
2. All vent valves on control panel opened.
3. All instrumentation covered.
4. Optics covered.
5. Test venue locked.

5.4 Precautions and Operation

Figure 5.1 shows the pressure circuit diagram of the control board for the Large-Scale Diffraction Shock Tube.

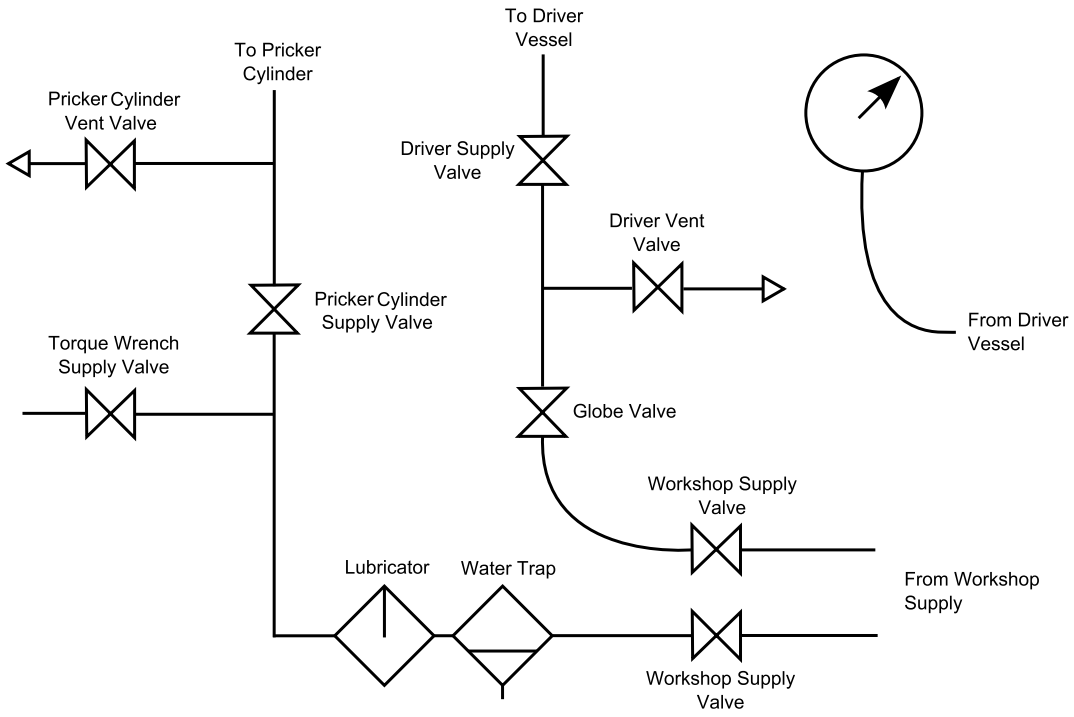

Figure 5.1: Pressure circuit diagram of control board for LSDST.

The following precautions have been identified in order to mitigate any risks identified in the risk assessment of operating the Large-Scale Diffraction Shock Tube. These are from Testing Precautions for Large-Scale Diffraction (450mm) Shock Tube (LSDST-02).

1. In the event of a failed diaphragm burst (diaphragm does not rupture or only slowly leaks following trigger release), the panel supply globe valve must be closed and the driver vent valve slowly opened to safely vent the driver. As venting may cause the diaphragm to rupture, the siren must be sounded at the start of this procedure and all hearing protection must be worn.

2. Make sure all the bolts for the driver section are screwed in correctly so as not to strip the bolts.

3. Apply grease on bolts every 20 tests to ensure long-life of bolt threads.

4. When placing diaphragm between gaskets, make sure the diaphragm grain direction is correct, the grain direction must be vertical.

5. All doors must be locked and if any unauthorised person enters the testing room, the testing procedure must be aborted immediately. The unauthorised person must be asked to leave the room for testing to proceed.
6. Blast barriers must be placed correctly and under no circumstances may anyone walk in-front of the shock tube outlet when testing.
7. Always make sure the pricker cylinder is re-set (retracted) before clamping the driver section with the new diaphragm set.
8. Make sure the oscilloscope has recorded a pressure trace before commencing the next test.
9. The siren must be sounded at least 30s before testing of the shock tube.
10. Hearing protection must be worn before testing of the shock tube.

The risk assessment and test logs of the tests performed can be found in Appendix D.

Chapter 6 Data Processing

6.1 Experimental Testing Observations

Data gathered during testing is tabulated in Table B.1. This table shows the date the test was performed, the test number of the day (for reference to manual test log), the material pair that was used, the diaphragm thickness used, the angle that the test pieces were set at using a digital inclinometer, the temperature of the laboratory at the time of the test and the Mach number of the test.

The labelling of the material pair is specified in the order the test pieces were loaded in to the shock tube. The material that is named first was loaded at the bottom of the shock tube and the material named second was loaded at the top. This convention is carried through into the experimental pictures, since in the shadowgraph images, the material type can not be identified. The last two tests performed were for glass and copper in the reverse set up, therefore the glass was loaded at the top and the copper at the bottom.

Diaphragm thickness was made up of either $100\mu m$, $130\mu m$ or $2 \times 100\mu m$ dielectric plastic. Calibration of the Mach number to natural burst was performed before testing with any materials took place. The results of the calibration can be seen in Figure B.1. The bursting pressure used in the testing was determined to be at 90% of natural burst (250kPa) for the $100\mu m$ and 85% of natural burst for both 130 and $2\times100\mu m$ diaphragm (300kPa and 415kPa respectively). These bursting pressures were chosen for repeatability as well as safety in operation of the shock tube.

The angle of the test pieces are referenced to the bottom of the shock tube, which is assumed to be perpendicular to the shock wave generated. To obtain the actual intended shock wave angle the following formula should be used:

$$\beta_{incident} = 90 - Angle \tag{6.1}$$

Where $\beta_{incident}$ is the shock wave incident angle, measured in degrees and Angle is the value tabulated in Table B.1.

6.2 Experimental Data Collection

Data was collected from the experimental images as follows:

All the images had adjustments applied to them to rectify rotation imposed by the optical set up as well as converting to grayscale. This was done to better identify the shock waves and shear layers. The contrast of the images was also increased to provide a clearer picture for measurements. All image adjustments were performed in Corel Photo-Paint X4. The adjusted images and original experimental images can be found in Appendix D

All angle measurements were performed in Autodesk Inventor Professional 2014 Computer Aided Design (CAD) package. This was done as there is a large degree of angular measurements within the sketch domain.

6.2.1 Regular Reflection Quantitative Data Collection

For incidence angles of 36 and 40°, the following method was used to measure the angle between the reflected shock wave and the surface, as these incidence angles were used to provide regular reflection data.

1. Create a new Autodesk Inventor Part file.
2. Import the adjusted experimental image onto the default sketch created.
3. Sketch lines along the wedge surfaces.
4. Sketch 4, 10mm lines.
5. Place the sketch lines at the location of the incident and reflected shock waves.
6. Align the sketch lines with the shock waves.
7. Dimension the angles between the wedge surfaces, incident shock waves and reflected shock waves.

8. Save part file with image and sketch.

Steps 1-8 were repeated for each test 5 times. The purpose for repeating the measurement 5 times was to provide statistical accuracy based on the standard deviation of the measurements. Additionally, the sketch lines were placed at the front, middle and back of the shock waves in order to provide a range of possible angles. The uncertainty analysis can be found in Appendix C. 10mm sketch lines were specified for measuring the angles to maintain the same level of uncertainty when measuring angles in each test. The measurements were done close to the reflection point to provide as much accuracy as possible and to take away any bias from any small curvature of the incident shock wave based on the real flow effects created when generating the shock wave as well as attenuation during the passage of the shock wave during the test.

The incident angles are recorded at both surfaces as it could not be guaranteed that the shock wave and shock tube are perfectly normal. Additionally, the inclinometer used to align the test pieces which had an accuracy of $\pm 0.1^\circ$ was aligned to the bottom of the shock tube for a zeroed reading. These measurements were verified using the CAD software.

The results shown in Table B.2 to Table B.25 are averaged readings with the standard deviation and error of readings. To see all the measurements performed please refer to the Excel spreadsheet and relevant part files in Appendix D.

An example of the regular reflection measurements is shown in Figure 6.1. This was the first measurement of glass vs copper at an intended incidence angle of 36° at a Mach number of 1.3058.

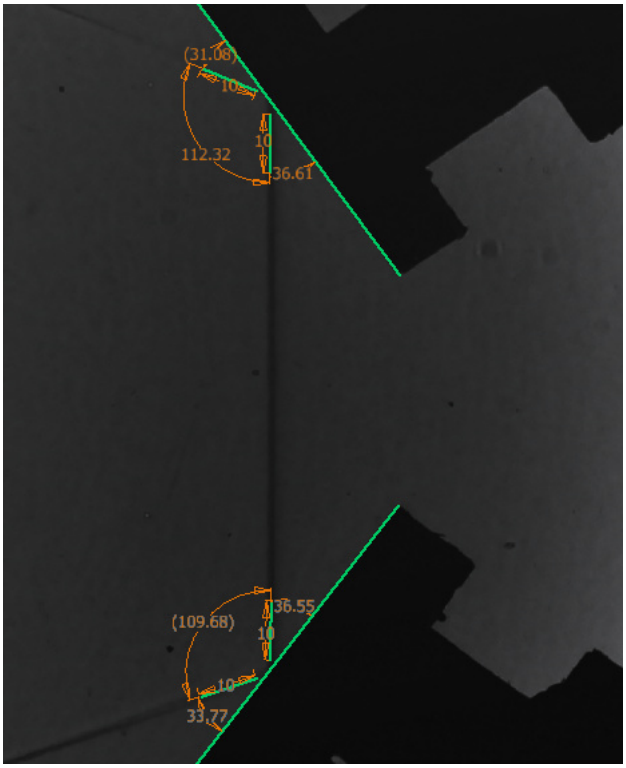

Figure 6.1: Example of regular reflection angle measurements

6.2.2 Irregular Reflection Quantitative Data Collection

For incidence angles of 60 and 70°, the following method was used to measure the angles between the incident and reflected shock waves, as these incidence angles were used to provide irregular reflection data.

1. Create a new Autodesk Inventor Part file.
2. Import the adjusted experimental image onto the default sketch created.
3. Sketch lines along the wedge surfaces.
4. Sketch 4, 10mm lines.
5. Place the sketch lines at the location of the incident and reflected shock waves.
6. Align the sketch lines with the shock waves.
7. Dimension the angles between the wedge surfaces and incident shock wave.
8. Dimension the angles between the incident shock wave and reflected shock waves.
9. Save part file with image and sketch.

Steps 1-9 were repeated for each test 5 times.

An example of the irregular reflection measurements is shown in Figure 6.2. This was the first measurement of brass vs aluminium at an intended incidence angle of 70° at a Mach number of 1.3038.

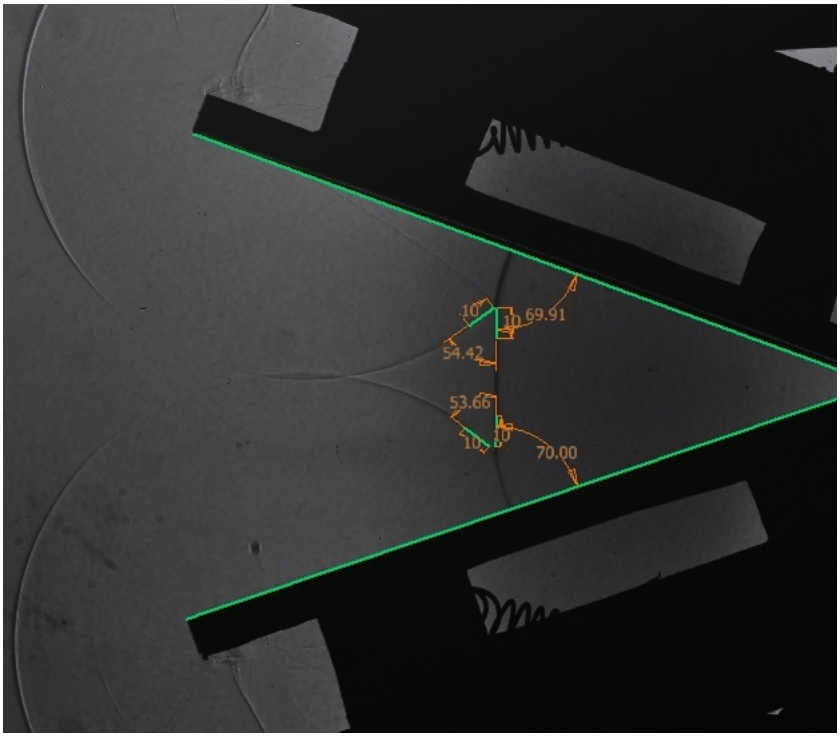

Figure 6.2: Example of irregular reflection angle measurements

The angle between the incident and reflected shock waves was recorded as this was a better measure of the comparison in the irregular reflection domain than the angle between the reflected shock wave and the Mach stem. This is due to the large curvature of the reflected shock wave. This decision was made from experience gained from previous work.

6.2.3 Theoretical Data Calculation

The theoretical reflection angles for regular reflection was calculated using Matlab. Matlab was used for its ability to implicitly solve equations. The process and code that was applied was reused from previous work [**1**]. The process is as follows:

1. Shock wave number and incident shock wave angle are input by the user.

2. Galilean transformation is performed to change reference frames (see Literature survey).
3. Specific gas constant is stated.
4. Normal Mach number moving into the shock wave is calculated.
5. The normal Mach number exiting the shock wave is calculated.
6. The $\theta - \beta - M$ relation is used to calculate the flow turning angle (θ).
7. The Mach number exiting the shock is calculated.
8. The reflected shock wave angles are solved implicitly for a weak and strong solution.
9. The pressure ratio across the shock wave is calculated.

The Matlab code can be found in Appendix D.

The following nomenclature is used in the Matlab code:

- M0 - Shock wave Mach Number
- Wi - Shock wave incident angle to reflection surface
- Gamma - specific gas constant ($\gamma = 1.403$ air)
- M0n - Normal Mach number moving into the shock wave
- M1n - Normal Mach number exiting the shock wave
- Theta - Flow turning angle (radians)
- Thetadeg - Flow turning angle (degrees)
- M1 - Mach number of gas exiting the shock
- Wref - Weak reflected shock angle solution
- Wref2 - Strong reflected shock angle solution
- Pressratio - Pressure ratio across shock wave

The theoretical data is presented in the regular reflection graph results shown in section 8.2. These calculations were performed at the average incidence angles of all the tests at the 36° and 40° intended angles, which was 36.16°1 and 40.170° respectively.

6.3 Qualitative Image Processing

To provide qualitative results, the following process was performed:

Images were adjusted in the same manner as in the quantitative data collection. Then the images were created using CAD as follows:

1. Create a new Autodesk Inventor Part file.
2. Import the adjusted experimental image onto the default sketch created.
3. Sketch 2 lines between two corresponding points on the wedge surfaces.
4. Sketch a line from the midpoints of the two lines created in the previous step.
5. Extend this line to the edges of the image.
6. Align the sketch lines with the shock waves.
7. Save part file with image and sketch.

The images were then saved as JPEG images to be included in this dissertation. The images can be found in section 8.5. Certain images could not have a centreline created as the trailing edges of the test pieces are distorted due to vortices created by the shock waves. They are still included in the dissertation for discussion.

Chapter 7 Results

This section contains the quantitative results obtained from the angle measurements in the Autodesk CAD package. The qualitative images are shown in chapter 8, as they can be discussed and displayed simultaneously.

7.1 Regular Reflection Results

The data that follows is displayed in the following order:

- The intended incidence angle
- The test piece material used
- The Mach numbers of the tests
- The average actual incidence angles measured from CAD, averaged from the 5 readings
- The standard deviation of the measured incidence angles
- The average reflection angles measured from CAD, averaged from the 5 readings
- The standard deviation of the measured reflected shock wave angles
- The error in each reflection angle measurement (calculated from standard deviation)

Table B.2 to Table B.7 show the results for the materials placed at an intended incidence angle of 36°.
Table B.8 to Table B.13 show the results for the materials placed at an intended incidence angle of 40°.

7.2 Irregular Reflection Results

The data that follows is displayed in the following order:

- The intended incidence angle
- The test piece material used
- The Mach numbers of the tests
- The average actual incidence angles measured from CAD, averaged from the 5 readings
- The standard deviation of the measured incidence angles
- The average angles between incident and reflected shock waves measured from CAD, averaged from the 5 readings
- The standard deviation of the measured angles between incident and reflected shock waves
- The error in each reflection angle measurement (calculated from standard deviation)

Table B.14 to Table B.19 show the results for the materials placed at an intended incidence angle of 36°.
Table B.20 to Table B.27 show the results for the materials placed at an intended incidence angle of 70°.

Chapter 8 Discussion

8.1 Introduction

This chapter contains the graphical representations of the experimentally obtained, quantitative data, as well as the images of the qualitative experiments. These sections are separated so as to easily identify features of the separate cases.

In the quantitative cases for each intended incidence angle, the graphs of the reflected angles vs. Mach number is shown for the combinations of the steel test pieces, the glass, aluminium and copper test pieces (with and without error bars), the brass test piece alone and lastly the brass and aluminium test pieces combined.

These graphs were chosen to provide clarity when analysing the data, as if all results are displayed on one graph no discernible, clear trends are observed. The steel graph is used as steel was used as a control material in the testing procedure. This was done to prove that reproducible results could be obtained in the shock tube using two test pieces of the same material. Glass, aluminium and copper results are shown together, to show the differences of reflection angles between the different materials. These are shown both with and without error bars to show the trends as well as the confidence of the information. Brass was omitted from these graphs as the brass did not behave in the same manner as the other materials. Therefore, the brass results are shown separately and compared to aluminium. This is done as one set of the test cases in the test matrix was to test brass and aluminium at the same time in the shock tube.

Possible reasons for the brass behaving differently are the surface roughness as well as the flatness of the test piece used.
The roughness of the brass may have had a slight affect on the size of the reflection angles. Although the materials were below the proposed limit of hydraulic smoothness, a viscous boundary layer is still present even though it is small. The brass test piece was the only material with an average surface roughness value higher than 0.5 μm, which may account for

the unexplained results. Additionally in polishing the materials it was noted that the brass test piece was not perfectly flat. All of the test pieces were polished on 0° tables and all but the brass test piece were polished to a flat surface. The brass test piece was flat longitudinally down the centre, however on the sides there was a slight transverse curvature roughly 2-3mm from the outer edges. This transverse curvature may have had a slight impact, by locally changing the incident angle of the shock wave, leading to a change in the reflection angle of the reflected shock wave. With the shadowgraph visualisation technique used, this would have been displayed in a shadow that may have not represented the reflected shock wave, reflecting off the majority flat surface.

After consideration it is deemed unlikely that the alloying of copper and zinc to make the brass was responsible for the different readings. This is due to brass being made in large quantities with an expected uniform distribution of component elements within the material.

The error bars that are displayed are 2 standard deviations above and below the average readings of each test measured. This provides a 95% confidence interval for each measurement.

8.2 Quantitative Regular Reflection

8.2.1 36° Intended incidence angle

For the 36° cases, the theoretical line is calculated at an incidence angle of 36.161°. This is the average incidence angle measured from all the measurements of each material pair. The average standard deviation from this incidence angle is 0.181°, which is considered to be accurate as it allows for only 2 of the smallest divisions allowed by the inclinometer used in the set-up of the experiment.

Figure 8.1 shows the results of the steel test pieces for different Mach numbers, at the intended incidence angle of 36°. It can be seen that the test pieces that were loaded at the bottom and top of the test tube produced similar reflection angles with large overlaps in their error bars. This suggests that the results at the top and bottom of the shock tube are valid and that the position of a test piece in the shock tube does not influence the shock wave reflection topology. It appears that within the range of Mach numbers generated during testing the steel test pieces did not follow the trend of reducing reflection angle with increased Mach number as compared to the theoretical line, instead the reflection angles off the steel test pieces seemed to be fairly consistent.

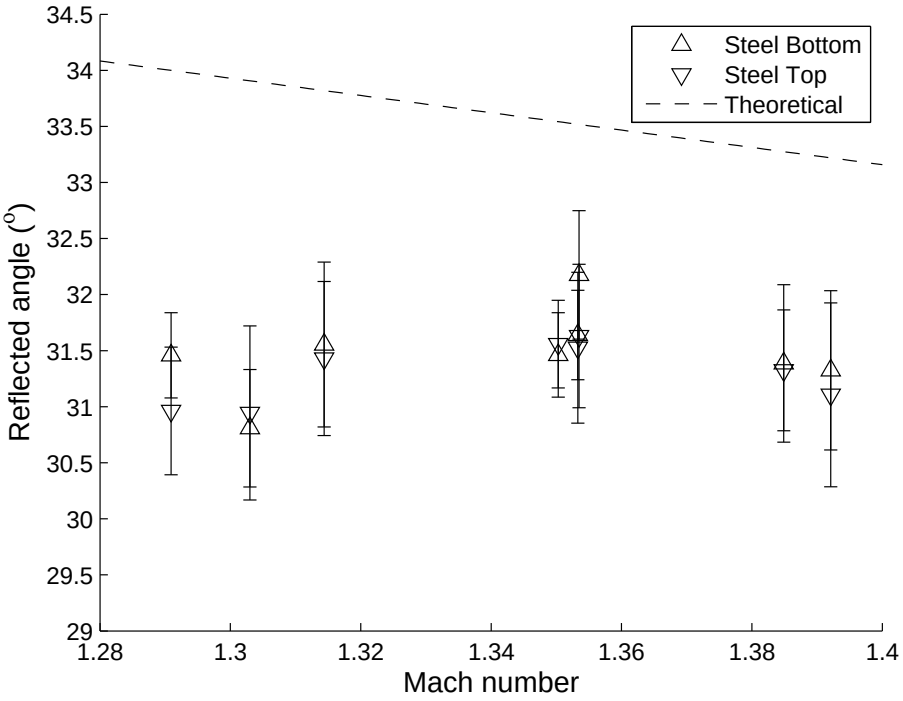

Figure 8.1: Graph of steel results at 36°

Figure 8.2 and Figure 8.3 show the results of glass, aluminium and copper at an intended incidence angle of 36°. It can be seen in Figure 8.2 that there is a difference in the reflection angles of the different materials with glass having the largest, copper the smallest and aluminium being a value in the middle at all Mach numbers tested.

The glass and copper results follow the theoretical trend of decreasing reflection angle with increasing Mach number, while the aluminium results stayed fairly consistent with increasing Mach number. The rate at which the reflection angle of the glass decreased with increasing Mach number was larger than that of copper.

In Figure 8.3 there is evidence that the error bars of the glass and copper results do not overlap at any of the Mach numbers tested. It is also seen that the glass results are the closest to the theoretical line with one result at ≈M1.305 having an overlap with the theoretical line. The aluminium error bounds do overlap with the glass and copper results especially at the higher Mach numbers. This is to be expected, as large confidence intervals were used.

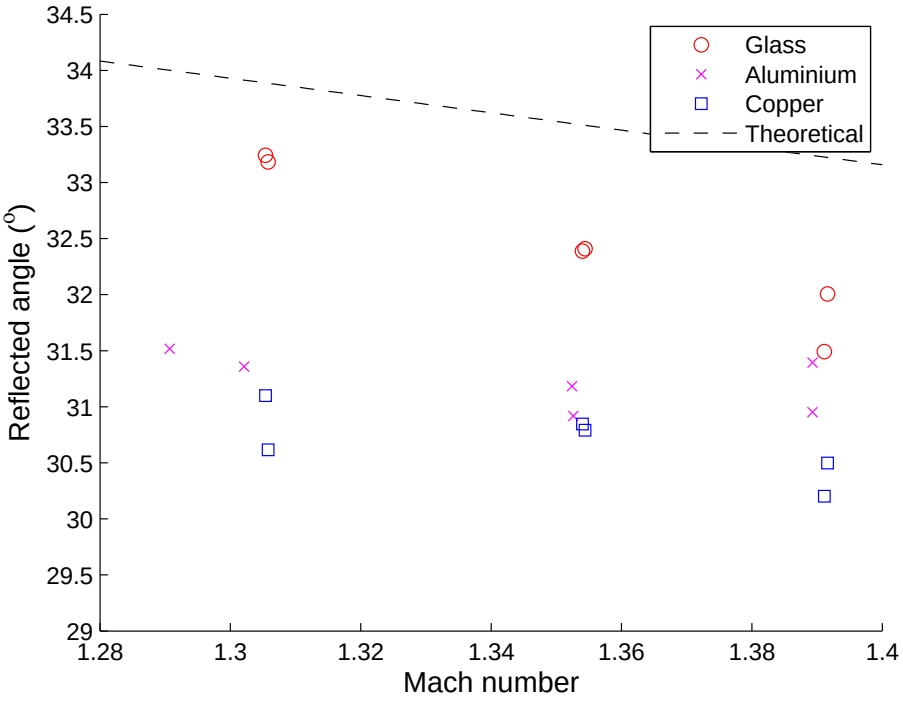

Figure 8.2: Graph of glass, aluminium and copper results at 36° without error bars

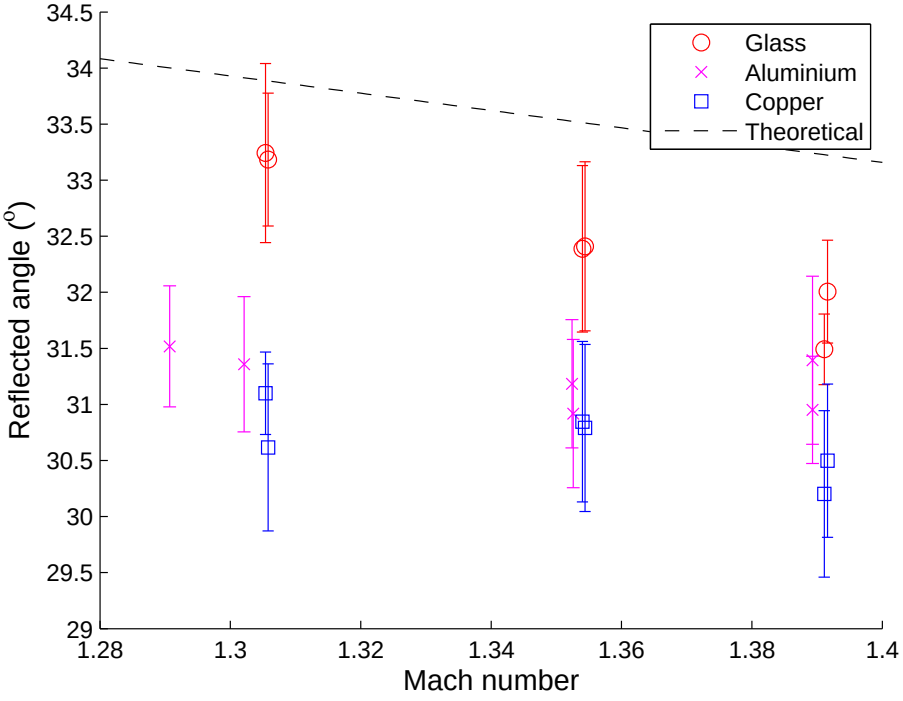

Figure 8.3: Graph of glass, aluminium and copper results at 36° with error bars

Figure 8.4 shows the results of brass at intended incidence angle of 36°. There is little change in reflection angle with increasing Mach number. Comparing the values to glass, the brass has smaller reflection angles than glass at Mach numbers lower than 1.355. After which, the reflection angles at the brass test piece were larger than at the glass test piece.

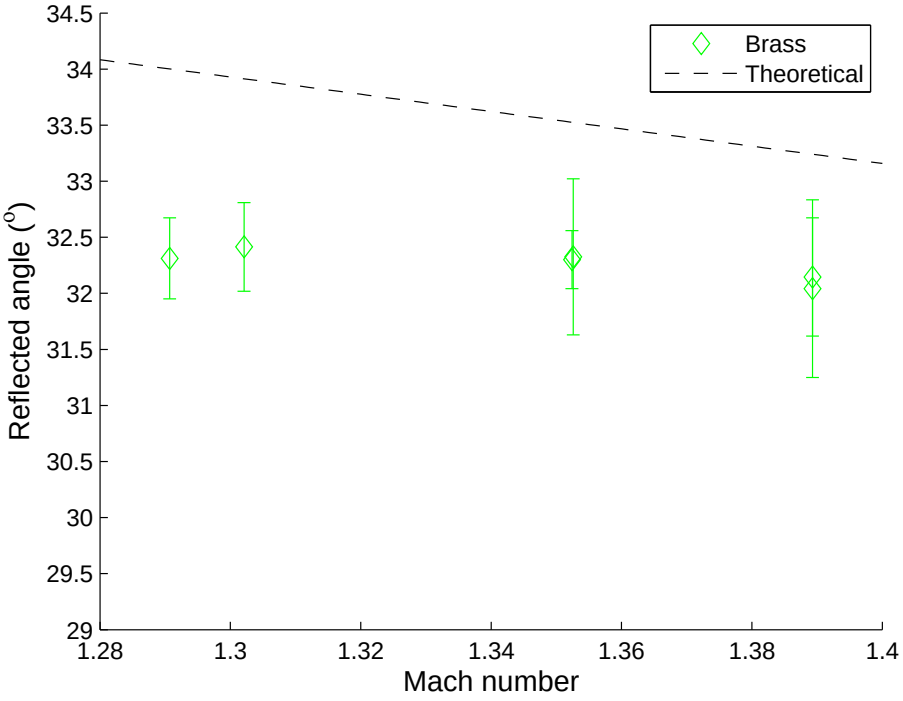

Figure 8.4: Graph of brass results at 36°

In Figure 8.5 the comparison between brass and aluminium indicates that the reflection angles of the brass tests were larger than those of the aluminium.

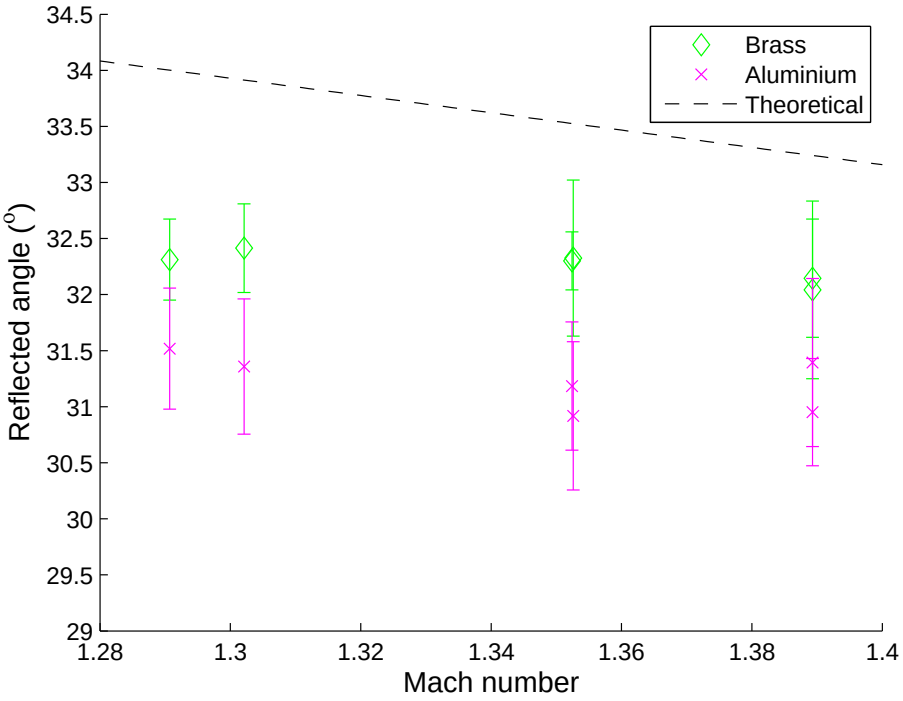

Figure 8.5: Graph of brass and aluminium results at 36°

8.2.2 40° Intended incidence angle

The average actual incidence angle for the 40° tests was 40.170°, with an average standard deviation of 0.182°. This is deemed accurate as the intended and actual incidence angles are within one standard deviation of each other. Additionally the theoretical line is calculated at 40.170° in each of the 40° graphs.

Figure 8.6 shows the results of the steel control experiments for the 40° case. In these tests there is a larger variation in the actual reflection angles than seen in the 30° case in the range M1.305-M1.360, however it is observed that there is still a large overlap in the error bars, therefore the confidence intervals indicate that the placement of the test pieces in the shock tube does not alter the reflection angle of the reflected shock waves.

The steel reflection angles do not follow the theoretical trend of increasing reflection angle with increasing Mach number. These results indicate that there is a slight decrease in the reflection angle with increasing Mach number.

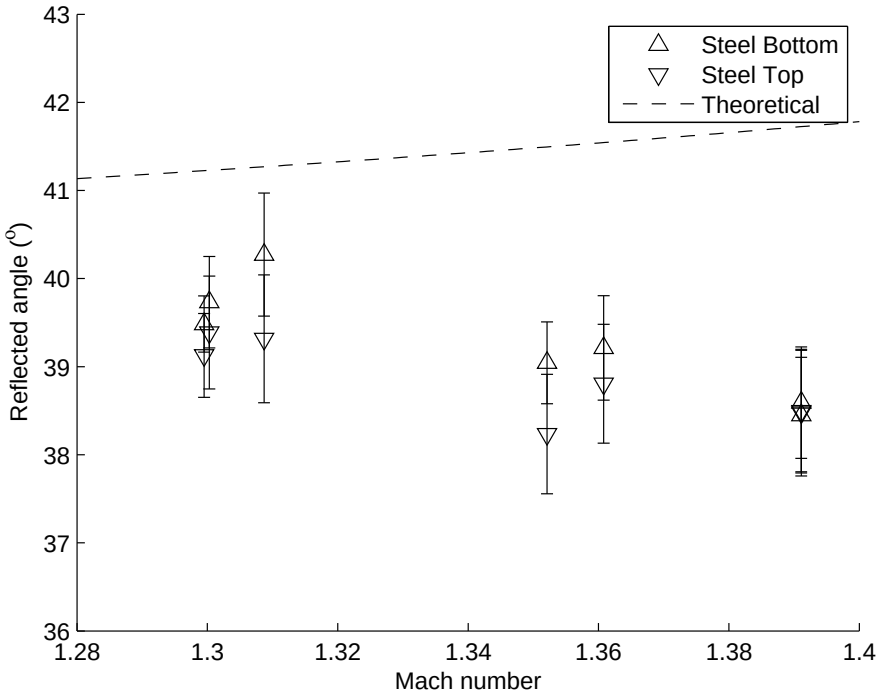

Figure 8.6: Graph of steel results at 40°

Figure 8.7 indicates similar results as the 36° for glass, aluminium and copper. It is evident that there is a clear difference in the reflection angles at the different material surfaces, with glass being the largest and copper being the smallest. Glass is the only material that follows the theoretical trend of increasing, reflection angle with increasing Mach number. However, its rise is not as steep as the theoretical line. Whereas, the aluminium and copper reflection angles decrease slightly with increasing Mach number. All of the results show good repeatability except for the copper reflection angles around a Mach number of 1.3 where a scatter can be seen of reflection angles between 37.36° and 38.36°. These results are substantially lower than the glass reflection angles and so are still valid and won't be considered as outliers.

Figure 8.8 again indicates the error bounds of the results obtained. The scatter of the copper reflection angles discussed earlier is largely negated due to the overlap of the error bounds. It is evident that there is only a small overlap of the aluminium and glass results at the lower Mach numbers tested, otherwise, the error bounds of all the materials don't intersect with each other showing a clear difference in reflection angles between the different materials.

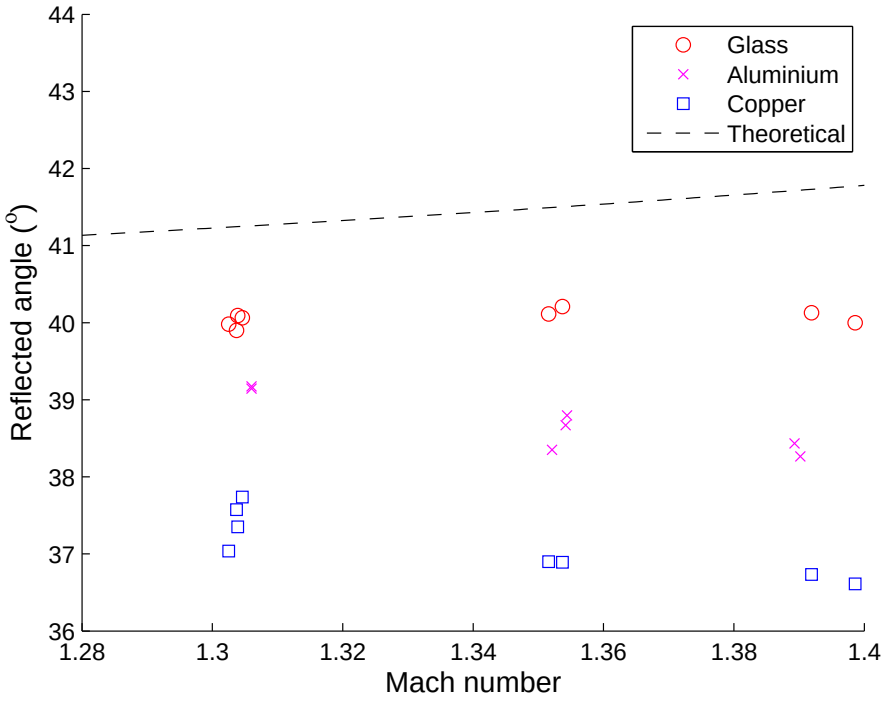

Figure 8.7: Graph of glass, aluminium and copper results at 40° without error bars

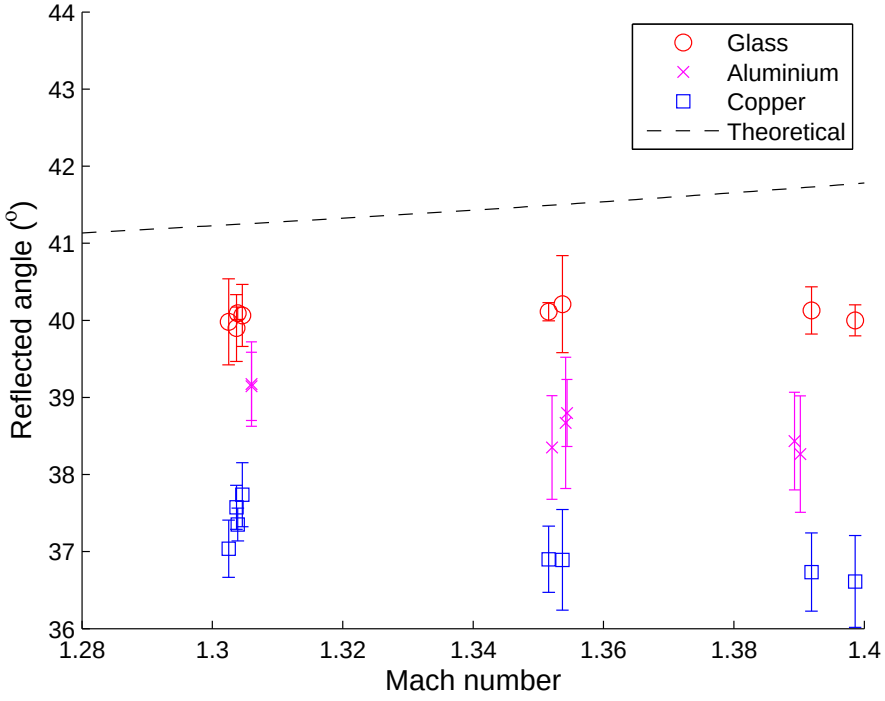

Figure 8.8: Graph of glass, aluminium and copper results at 40° with error bars

Figure 8.9 indicates the behaviour of the reflected shock wave off the brass test piece and again the trend of the reflection angle is to stay constant with increasing Mach number. When compared to the values of the glass, the brass results are marginally larger and are closer to the theoretical value line, which is not expected due to the higher thermal conductivity of the brass test material.

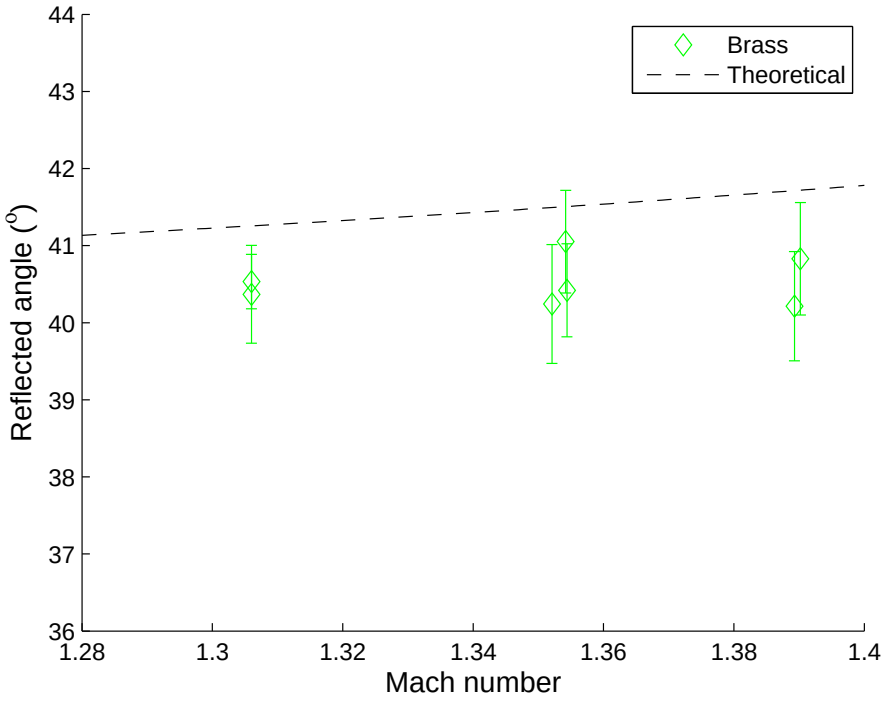

Figure 8.9: Graph of brass results at 40°

In Figure 8.10 there is a difference in reflection angles in the tests that were performed with brass and aluminium. There is only a small intersection of the error bars in two of tests at ≈M1.58. The difference in the reflection angles between the brass and aluminium is to be expected with the difference in thermal conductivity of the two materials.

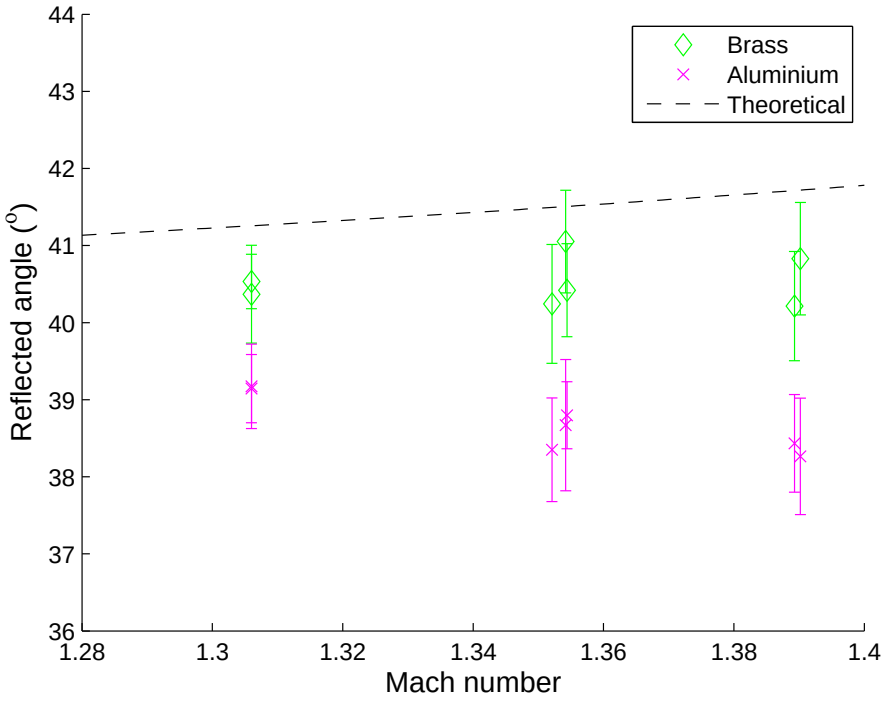

Figure 8.10: Graph of brass and aluminium results at 40°

8.3 Quantitative Irregular Reflection

As mentioned earlier, the measurements for the irregular reflection cases were performed between the incident and reflected shock waves, in order to provide a measurement with a higher degree of accuracy, rather than measuring between the reflected shock wave and Mach stem as was done in previous work. The graphs do not display any theoretical value lines as two-shock theory does not apply to irregular reflection.

8.3.1 60° Intended incidence angle

At an intended incidence angle of 60° the average incidence angles measured from all tests was 60.034° with an average standard deviation of 0.088°. This is more accurate than hoped for as it is less than one of the smallest increments that can be measured by the inclinometer in the set up of the experiments.

The steel control results for 60° are shown in Figure 8.11. There is a clear collection of the data at discrete points based on the Mach numbers, with very little scatter. Most of the variation of the average readings is contained within the error bounds of the other readings. There is a general trend of increasing angle between the incident and reflected shock waves with increasing Mach number, with an exception at approximately M1.315. However, both test pieces display similar results, which indicates that the positioning of the test pieces did not affect the results.

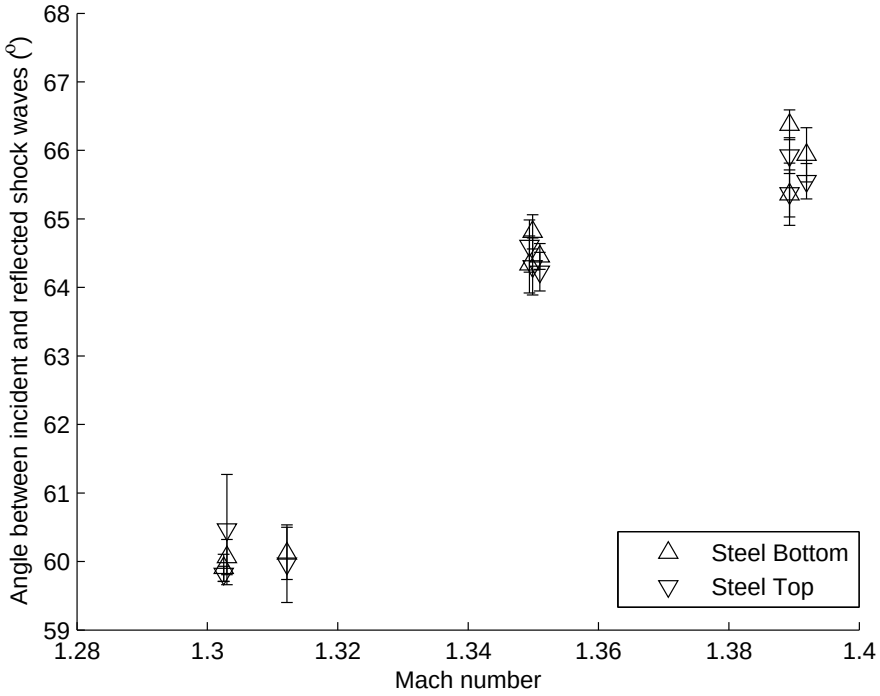

Figure 8.11: Graph of steel results at 60°

The trend of increasing angle with increasing Mach number is seen again in the results of copper, aluminium and glass as is shown in Figure 8.12. There is a large difference in angle size between the copper and glass results. The aluminium angles are not intermediate values at lower Mach numbers as was seen in the regular reflection results. However, at the highest Mach numbers tested this behaviour is seen again. The aluminium does have an outlier at M1.38, where the data value does not increase from the values at M1.36.

The rate at which the glass angles increase is higher than both the copper and aluminium, while the aluminium has the slowest rate of angle increase when compared to the Mach number.

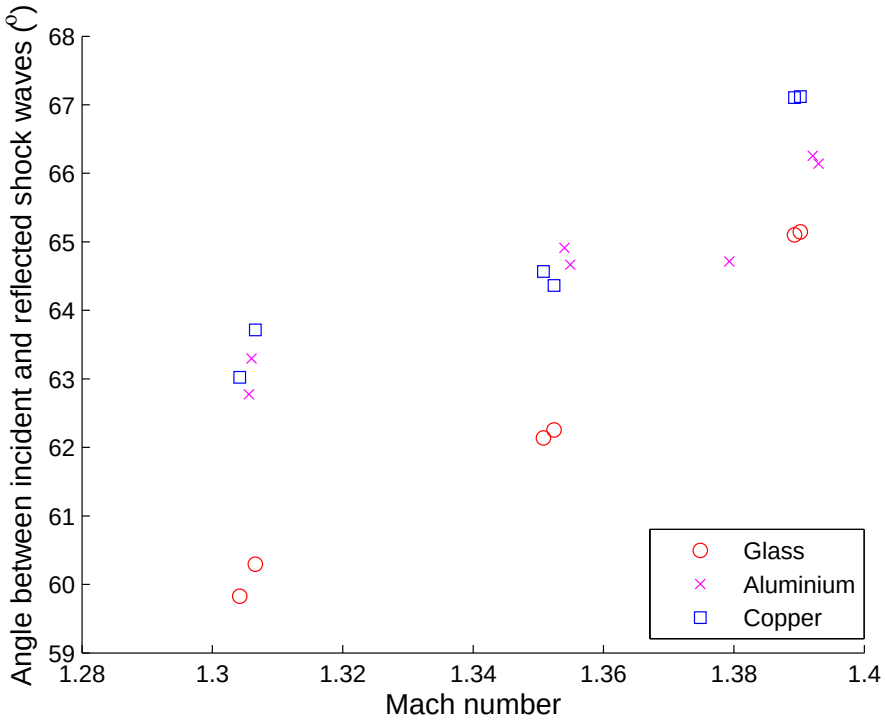

Figure 8.12: Graph of glass, aluminium and copper results at 60° without error bars

The error bounds in Figure 8.13 show the glass and copper results lying far from each others 95% confidence intervals with the aluminium values and error bounds matching the copper at the lower Mach numbers of M1.31 and M1.355. At M1.39 there is no crossing of the error bars of any materials shown in this graph.

The brass results at this incidence angle follow the same trend as the glass when compared between Figure 8.14 and Figure 8.13. The brass values are slightly higher and form intermediate values between the glass and copper angle values.

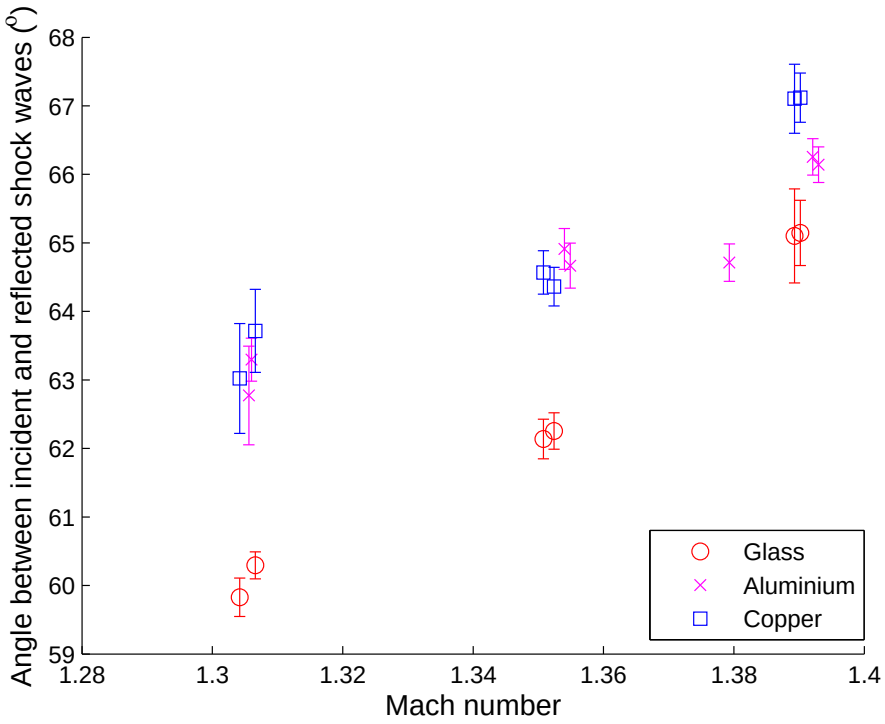

Figure 8.13: Graph of glass, aluminium and copper results at 60° with error bars

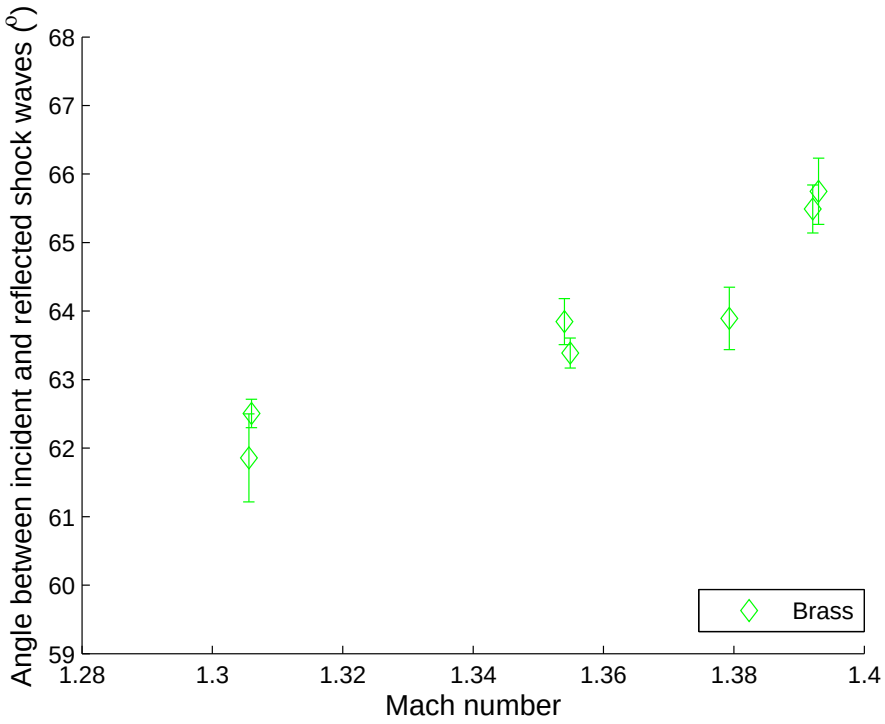

Figure 8.14: Graph of brass results at 60°

This trend is displayed again in Figure 8.15 where the brass and aluminium have a similar gradient of increasing angle between the reflected and incident shock waves with Mach number. The brass, has a similar outlier to the aluminium at M1.38, which indicates a single test where conditions may have been different in the shock tube than experienced in other tests. There is some overlap between the brass and aluminium error bounds. However, the angles of the aluminium are larger than the brass for the majority of the tests performed.

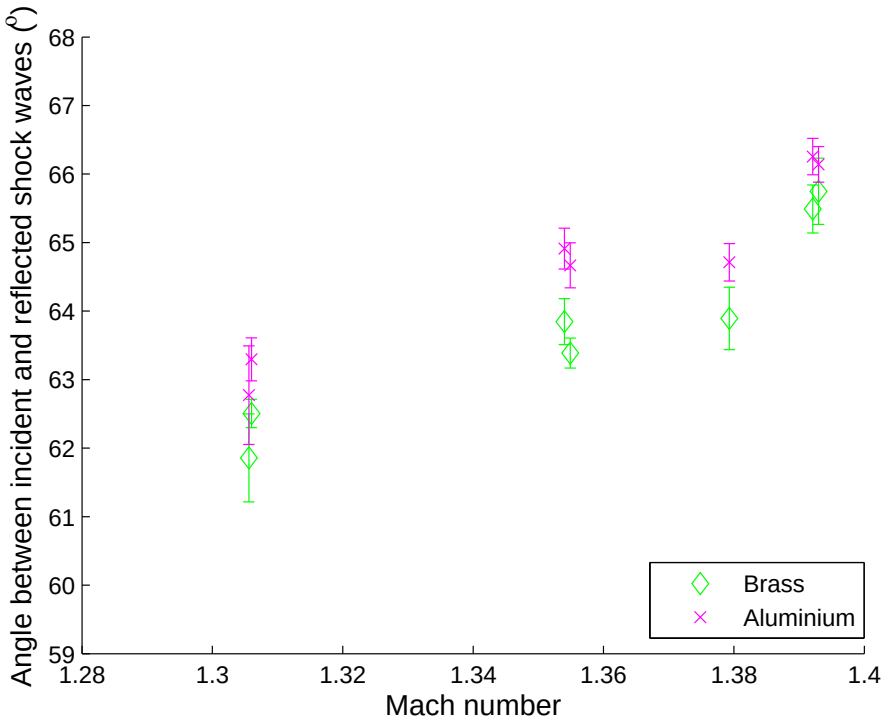

Figure 8.15: Graph of brass and aluminium results at 60°

8.3.2 70° Intended incidence angle

The last set of tests performed for each pair of materials was done at an intended incidence angle of 70°. The average actual incidence angle from all the measurements was 70.044° with an average standard deviation of 0.089°. This was a degree of accuracy that was better than hoped for.

The steel control results shown in Figure 8.16 indicate a slightly bigger variation in the angles between the incident and reflected shock waves than what was experienced in the 60° tests. However, there was a large overlap of error bars for both the test pieces at all Mach numbers, providing confidence in the set up of the experiment. Apart from the results at M1.318, there is very little affect on the angle with an increase in Mach number. At M1.318 two tests indicated that the the angle is slightly smaller at this Mach number than at other Mach numbers.

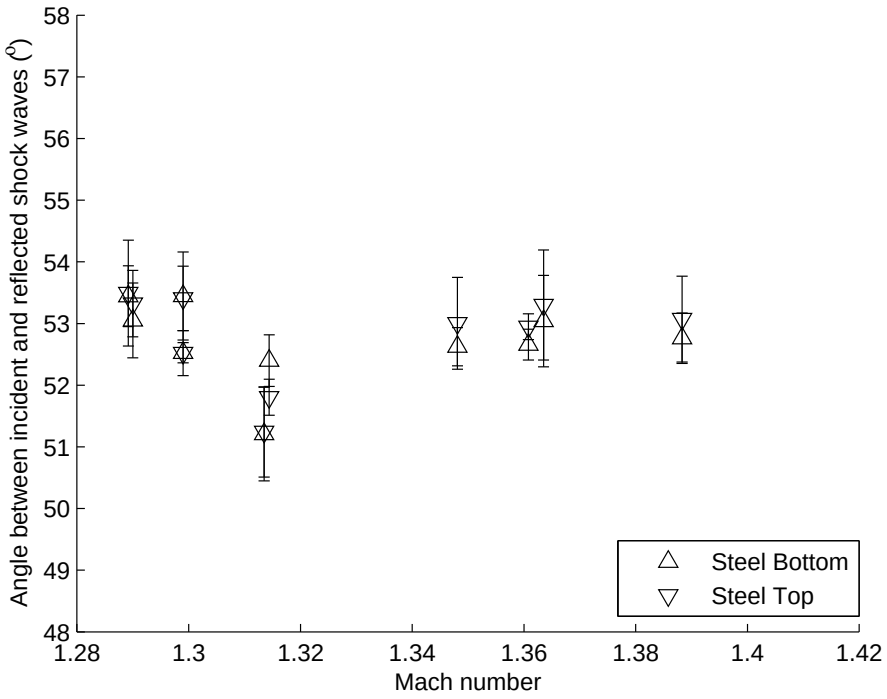

Figure 8.16: Graph of steel results at 70°

The comparison of the glass, aluminium and copper results in Figure 8.17 show the difference in angles between all three of the materials displayed. With aluminium being an intermediate value between the copper and the glass and the copper displaying the largest angles between the incident and reflected shock waves. There appears to be a very slight increase in the size of the angle for the glass and aluminium cases with increasing Mach number, where the copper results remain fairly constant. One test seems to be an outlier at M1.39 where there is a jump in both the glass and copper's angles as compared to the trends of the other results.

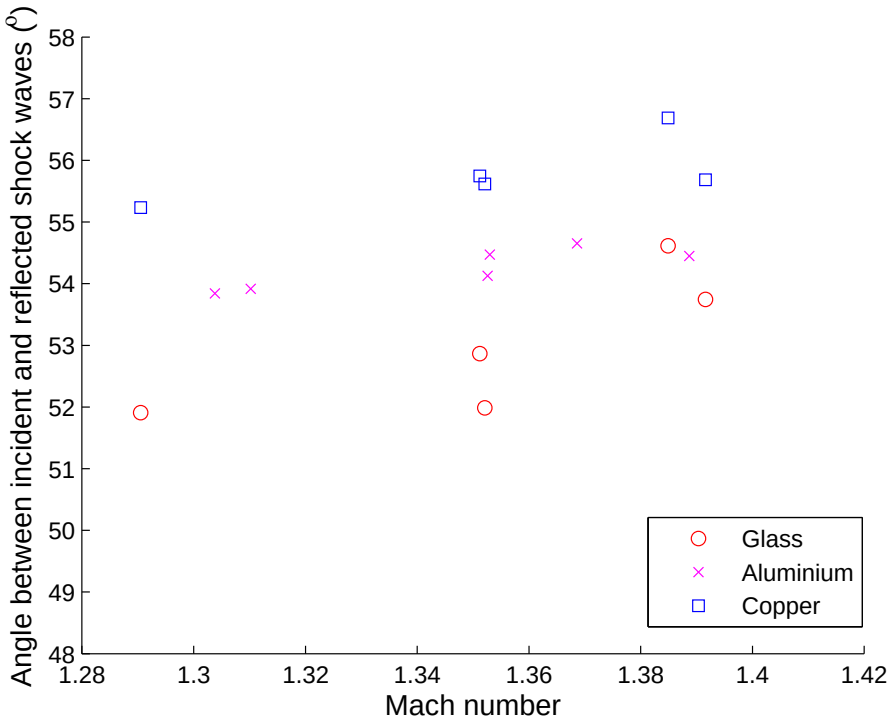

Figure 8.17: Graph of glass, aluminium and copper results at 70° without error bars

If that result is ignored, the error bounds of the glass, aluminium and copper do not intersect except for one case at ≈M1.395 where the aluminium and glass results overlap by 2 standard deviations. These error bounds can be seen in Figure 8.18. It is evident that there is a large difference in the error bounds of the copper and glass leading to confidence that that their large difference in thermal conductivity could be the cause of the difference in angles.

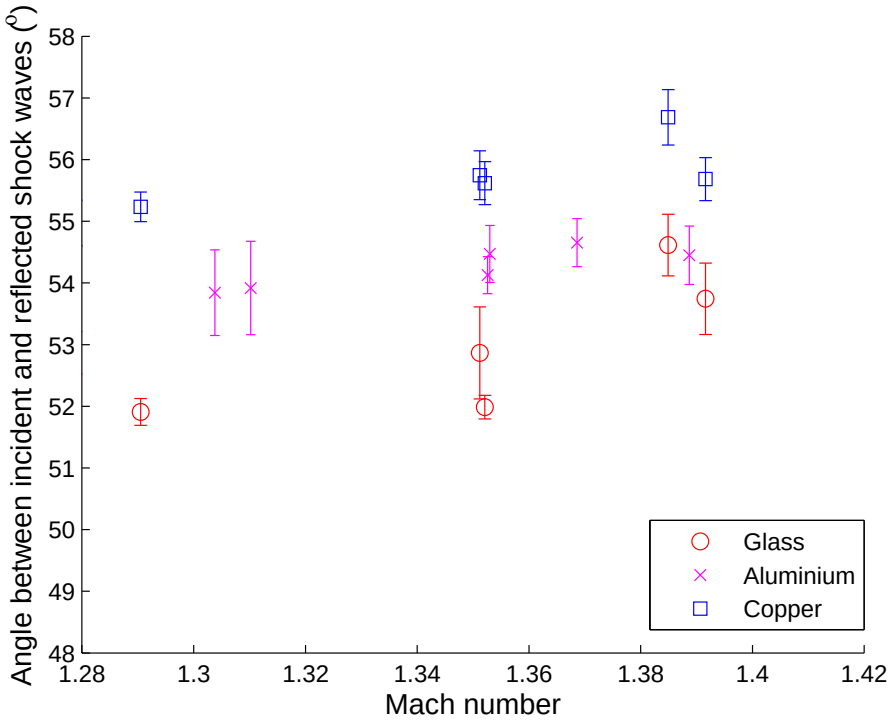

Figure 8.18: Graph of glass, aluminium and copper results at 70° with error bars

For the brass results in Figure 8.19 there is a slight trend for the angle values to increase with increasing Mach number, however this is very small. Again as seen in the 60° case, the brass values are larger than the glass ones and form intermediate results between the glass and copper.

In Figure 8.20 the brass values are generally smaller than those of the aluminium, however the overlap in the error bars is larger than previously experienced.

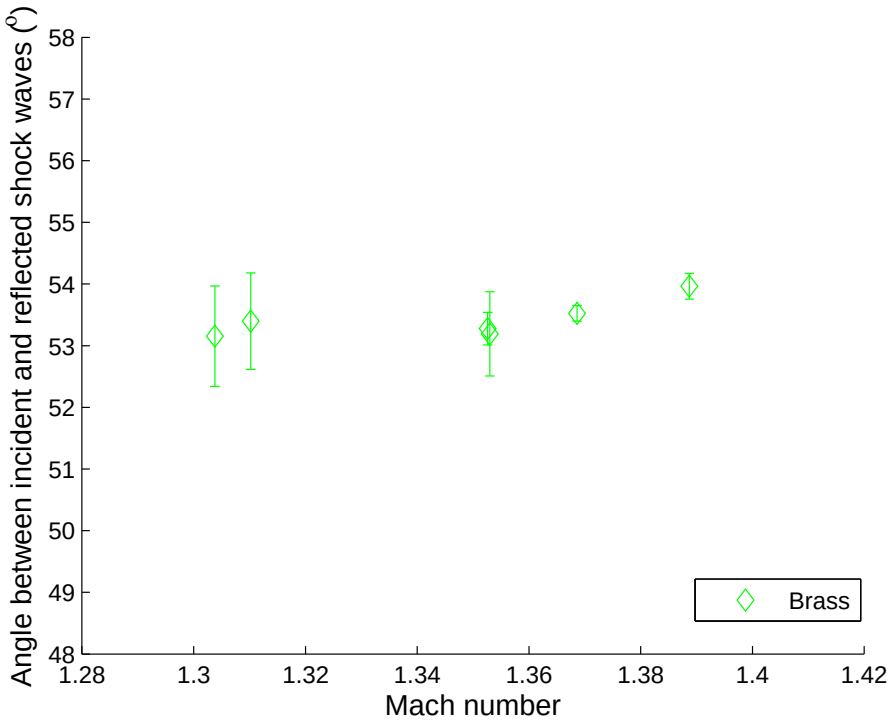

Figure 8.19: Graph of brass results at 70°

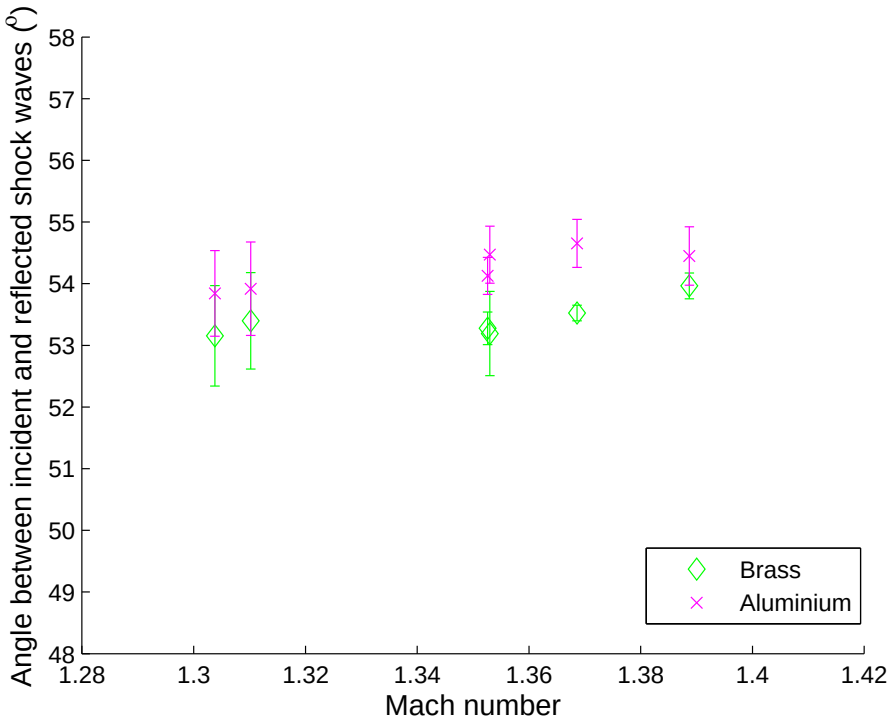

Figure 8.20: Graph of brass and aluminium results at 70°

8.4 Quantitative Trends and Analysis

From all the quantitative results it is observed that there is a difference in angular measurements based on the material that the shock wave is reflecting off.

In the regular cases glass had the smallest reflection angles and was generally the closest to the theoretical values calculated from two-shock theory. This is to be expected as the glass was the smoothest and has the lowest thermal conductivity. This means it should behave as close to a frictionless and adiabatic surface as is possible. However, there is still a difference to the theory as the glass did have a surface roughness and thermal conductivity even though these are very small and considered to be under the hydraulic limit for smoothness.

Thereafter it can be seen that with increasing thermal conductivity the reflection angle got progressively smaller with aluminium and copper being smaller than glass and copper being the smallest. This corresponded to copper having the highest thermal conductivity of the materials tested.

The brass results are not considered as part of the overall results. This was based on its behaviour being different to the other materials. Yet, when compared to aluminium, which was tested simultaneously, it follows the same trend based on thermal conductivity as the other materials.

In the irregular reflection experiments the opposite behaviour is noted, where the larger the thermal conductivity, the larger the angle was between the incident and reflected shock waves. This is to be expected when compared to the regular reflection results, as based on geometry, if the angle between the reflection surface and reflected shock wave is smaller, the angle between the reflected and incident shock waves must be larger.

This indicates that the behaviour of the reflected shock wave does not change between the regular and irregular reflection cases based on thermal conductivity. This is a benefit as the irregular reflection cases then substantiate the results seen in the regular reflection cases.

The results when the copper and glass test pieces were reversed was not included in the graph to keep the results clear and concise. The results that follow were when the copper was placed at the bottom and glass at the top at an intended incidence angle of 70° and a Mach number of 1.3141. The angle between the incident and reflected shock wave for the copper was 54.272° with an error of 0.242°. At the glass the average angle measurement was

50.972° with an error of 0.514°. These results lie outside of each others error bars, further when compared to the original results of the glass at the bottom and the copper at the top there is only a small variation (less than 1°), leading to the assumption that local buoyancy effects at the surfaces are not a factor in the reflection topology in this testing.

There is only one quantitative and one qualitative test for when the glass and copper was reversed. This was due to the glass test piece breaking after these tests were performed. The test piece broke as the epoxy adhesive used to hold the test piece to the mounting blocks, failed after fatigue loading from the tests performed and introduced uneven stress on the test piece leading to fractures in the glass.

8.5 Qualitative Regular Reflection

For the qualitative analysis of the regular reflection, vortices caused by the shock waves around the trailing edges of the test piece, obscured the corners. Additionally, no accurate edge could be used as the leading edge of the test piece is out of the frame due to the zooming of the optical set up. Therefore, no centreline could be drawn. However, other observations could be made and will be discussed in this section. White arrows placed on images indicate points of interest that will be discussed.

8.5.1 Steel vs. Steel

In Figure 8.21 at the arrows marked 1 it can be seen that the diffracting incident shock wave has rounded the back corner of the test pieces and is impacting the support structure of the test pieces at roughly the same position for both of the test pieces. In between the two trailing edges of the test pieces, marked 2, the shape of the reflected waves is the same in the lower and upper halves, and there does not appear to be any difference in the vortex patterns at the trailing edges.

Figure 8.21: Shadowgraph of steel vs. steel at 40° and M1.3519

Figure 8.22 displays a centreline, which was placed as accurately as possible, with the available features in the shadowgraph. Points indicated 1, show different shadows above and below

the test pieces. This was due to the tape that was protecting the optical windows moving due to the force of the shock wave. Only tests where the tape moved below and downstream of the reflecting surfaces were considered, as the tape here would have no affect on the shock wave reflection topology. This should be noted for shadowgraphs that follow with similar differences in the images.

The points marked 2 show that the incident wave has diffracted around both of the steel test pieces to the same degree and is reaching the support structure at the same location for both the bottom and top test pieces. In this image the reflected shock waves intersect with each other in two locations marked 3, along the centreline between the two images indicating that there is a symmetry of the reflection patterns of both of the test pieces.

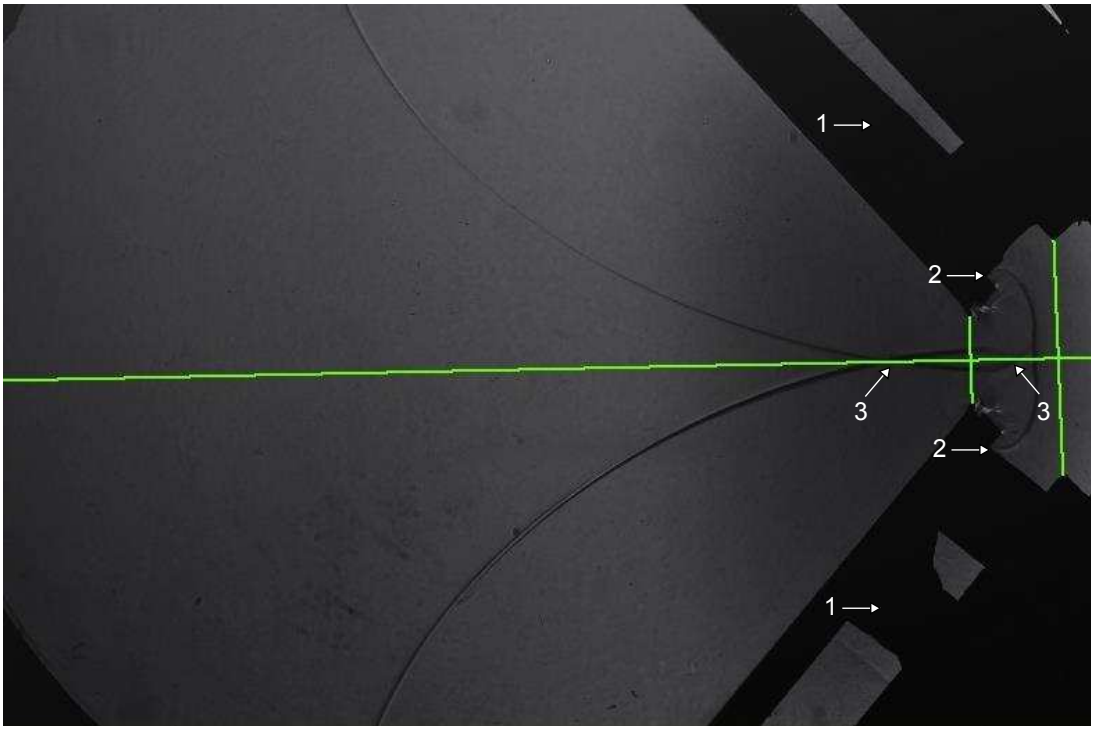

Figure 8.22: Shadowgraph of steel vs. steel at 40° and M1.3907

8.5.2 Brass vs. Aluminium

Measurement of the brass and aluminium test pieces after manufacturing, revealed that the brass was 9mm thick and the aluminium test piece was 10mm thick. This limits the images that can be analysed, as images where the incident shock wave has passed the bottom corner of the trailing edge are invalid. This is due to the difference in flow effects produced by the diffraction of the shock wave around the corners at different points in time. However, images where the shock wave has only diffracted around the top corner can be discussed as the same conditions have been experienced by the incident shock wave at both test pieces up until the point in time when the photograph was taken.

In Figure 8.23 and Figure 8.24 the same effects can be seen in both images, where the incident shock wave has gone past the trailing edge and is diffracting along the back surface of both test pieces. It can be seen at point 1 that the incident shock wave has rounded the trailing edge of the aluminium and has diffracted further along the trailing surface than the incident shock wave at the brass test piece as seen at point 2.

Figure 8.23: Shadowgraph of brass vs. aluminium at 40° and M1.3056

Figure 8.24: Shadowgraph of brass vs. aluminium at 40° and M1.3888

Figure 8.25 shows a case where the incident shock wave has not reached the trailing edge of either of the test pieces. However at point 1 along the aluminium test piece, the incident shock wave is closer to the trailing edge than at point 2 along the brass test piece.

Figure 8.25: Shadowgraph of brass vs. aluminium at 40° and M1.3521

8.5.3 Glass vs. Copper

In the machining of the glass test piece the thickness was altered to be 12mm to provide extra strength and reduce the machining time required in order to meet the product procurement deadline. This means that the glass test piece was 2mm thicker than the copper test piece, and therefore, similar to the brass and aluminium test cases, images with the incident shock wave diffracting around the bottom edge of the trailing surfaces can't be considered due to different surface conditions at the two test pieces. Unfortunately, all qualitative regular reflection images for glass and copper had the incident shock wave at or past the bottom edge of the trailing surfaces and won't be able to be discussed.

8.6 Qualitative Irregular Reflection

In the qualitative irregular reflections, the incident shock wave was not past the trailing edge of the test pieces. This allows the images to be analysed, with centrelines placed from Autodesk CAD in most of the images as no distortion of the corners of test pieces occurred.

8.6.1 Steel vs. Steel

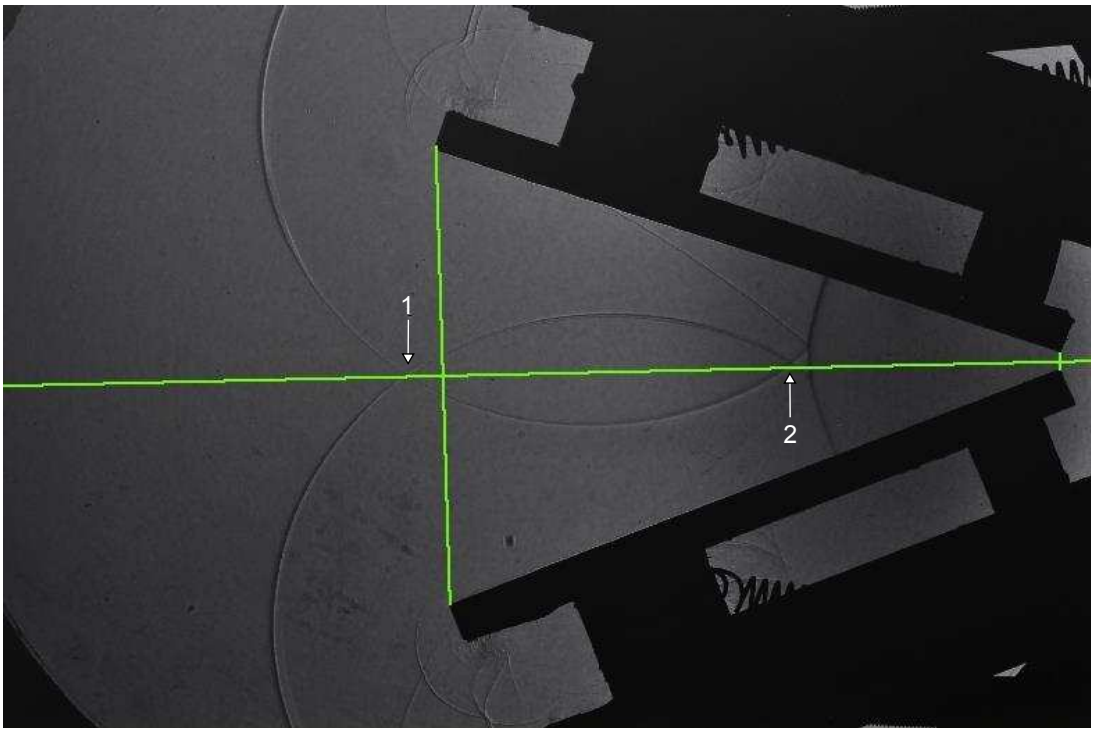

Figure 8.26: Shadowgraph of steel vs. steel at 70° and M1.3883

In Figure 8.26, the intersection points of the reflected shock waves are considered as an indication of symmetry. At point 1 this point lies on the centreline as the reflected shock waves travel back past the leading edge of the test pieces. At point 2 the intersection point lies slightly above the constructed centreline, however the shape of the Mach stems is slightly different, with the Mach stem at the top steel test piece having a small concave curvature, which could be responsible for the asymmetry so close to the triple points of both test pieces.

In contrast, Figure 8.27 shows symmetry about the centre line as can be seen at point 1 where the intersection of the reflected shock waves lies on the centreline. Additionally at point 2, the triple points arising from both test pieces, meet at the centreline, with both Mach stems having the same shape.

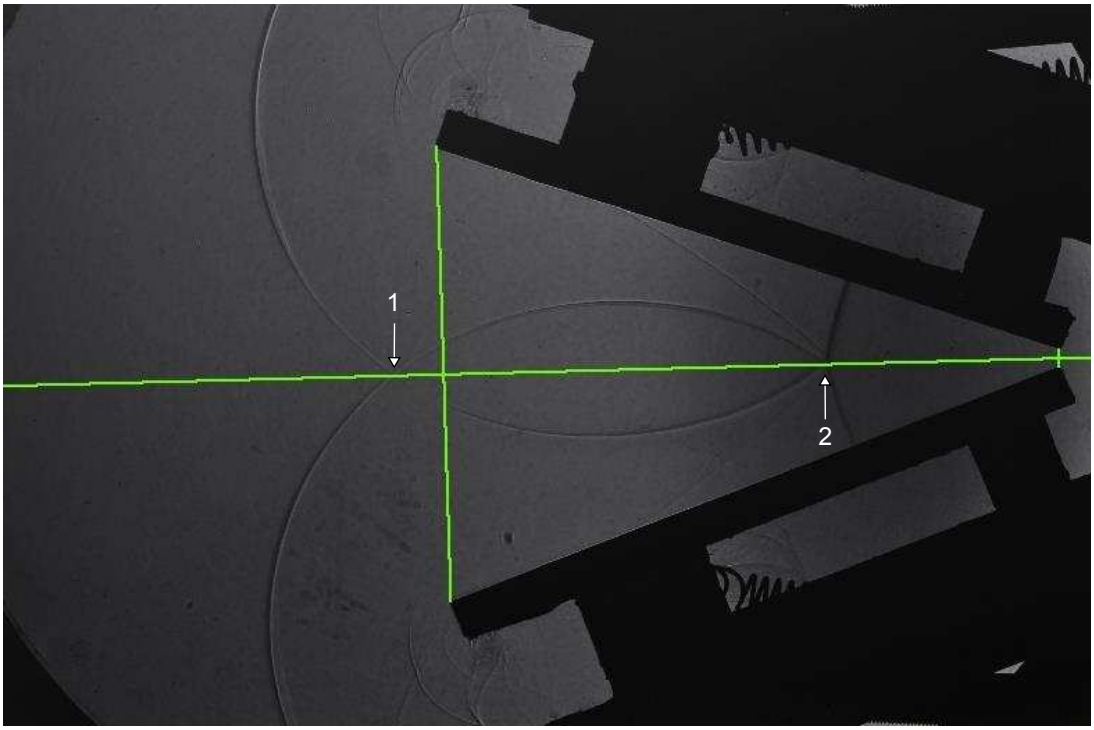

Figure 8.27: Shadowgraph of steel vs. steel at 70° and M1.4018

In Figure 8.28 the intersection of the reflected shock waves at point 1 lie on the centreline. The intersection of the two shear layers at point 2 lies above the centreline. However, the arrow marked 3 shows a transverse wave that has moved into the area, which may be changing the flow characteristics around the shear layers and offsetting their trajectory. It is unlikely that the transverse shock wave would have an effect on the reflected shock waves as it is much weaker than the reflected shock waves. The transverse shock wave is probably caused by the rupture of the diaphragm not being longitudinally aligned with the shock tube.

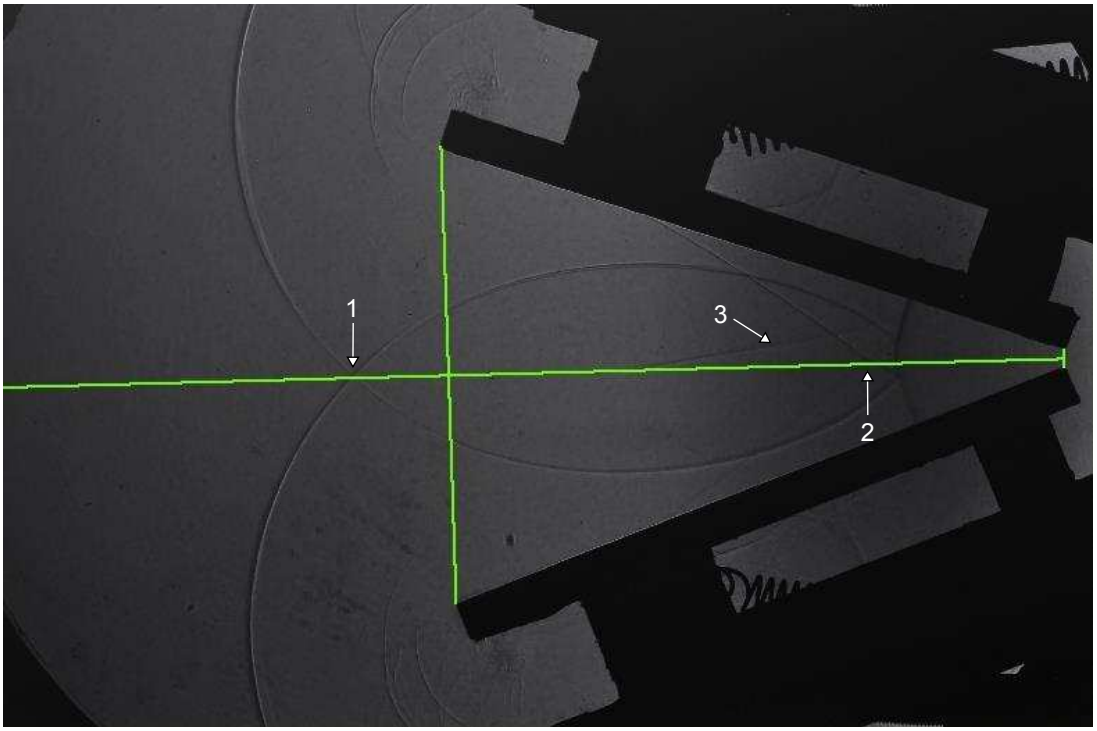

Figure 8.28: Shadowgraph of steel vs. steel at 70° and M1.3876

8.6.2 Brass vs. Aluminium

Figure 8.29 and Figure 8.30 show features of asymmetry based on the locations of the intersection of the reflection point, labelled 1 and 2. In both images these points lie slightly above the centre line, indicating a greater reflection angle at the bottom surface. Additionally, close to the triple points to the right of point 2, the space between the reflected shock wave and centre line is larger above the centreline than it is below the centreline.

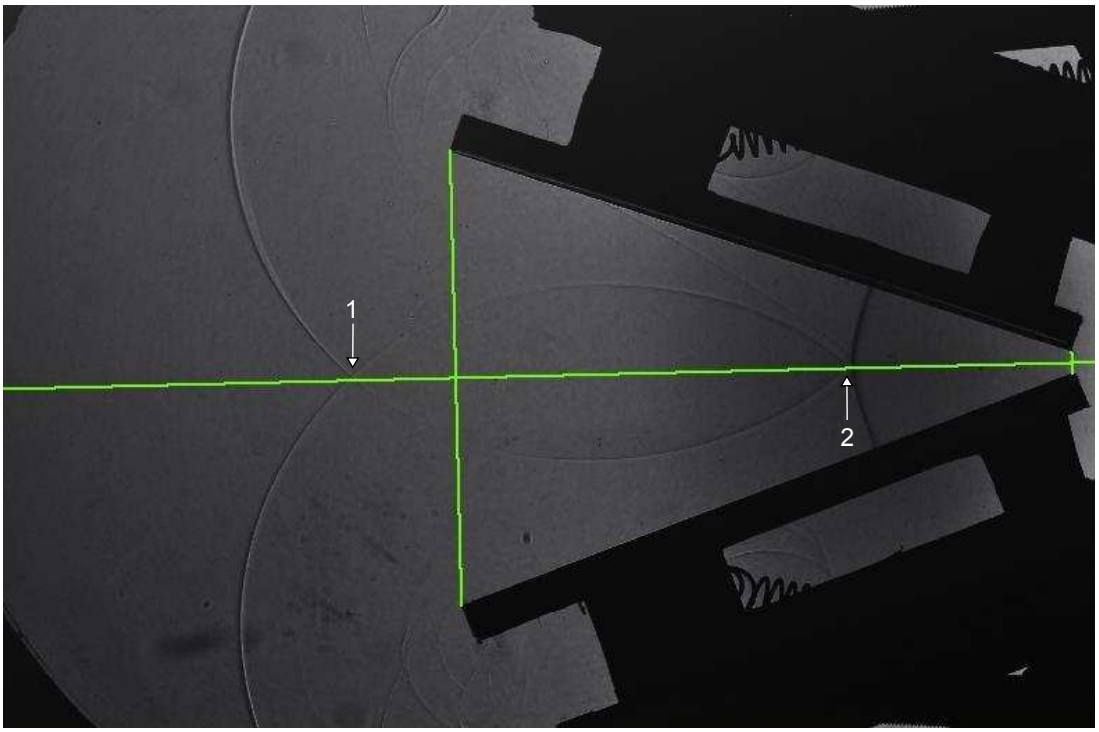

Figure 8.29: Shadowgraph of brass vs. aluminium at 70° and M1.3083

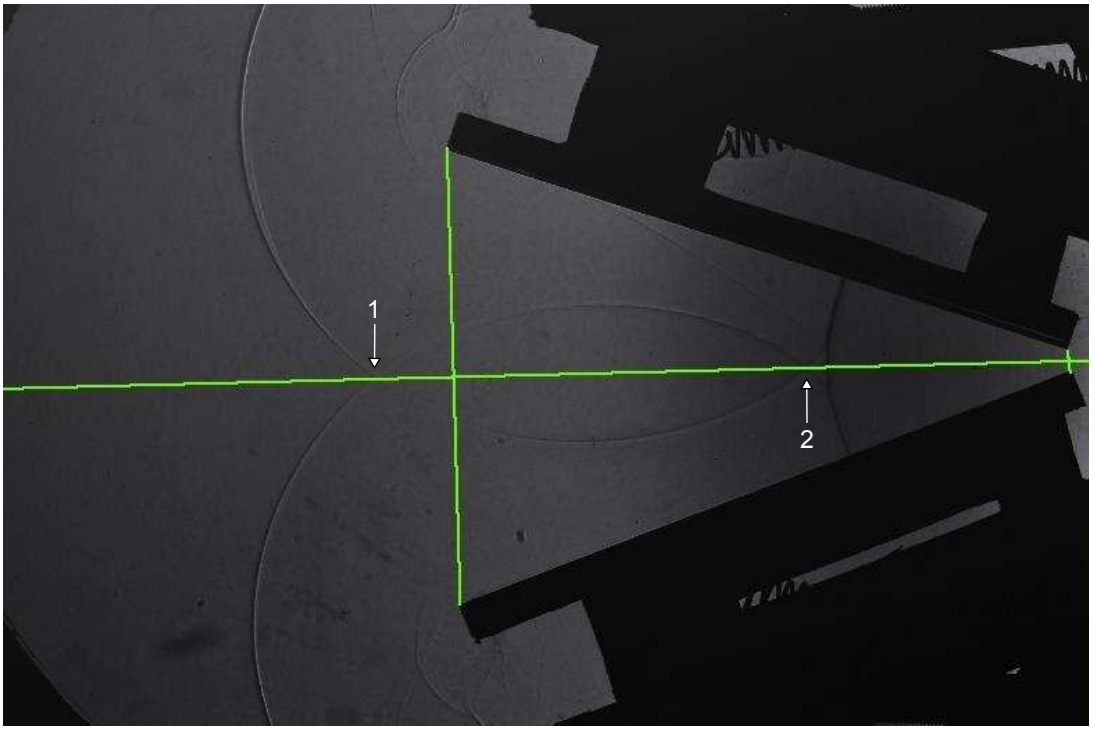

Figure 8.30: Shadowgraph of brass vs. aluminium at 70° and M1.3102

In Figure 8.31 the intersection points of the reflected waves can't be clearly seen as the centreline obstructs these points of interest. However at point 1 it can be seen that the point where reflected waves meet the centre line is different with differing gradients. The reflected wave from the brass test piece at the bottom meets the centreline at a shallower angle than one from the aluminium test piece at the top. This indicates that the intersection of the shock waves will occur above the centre line.

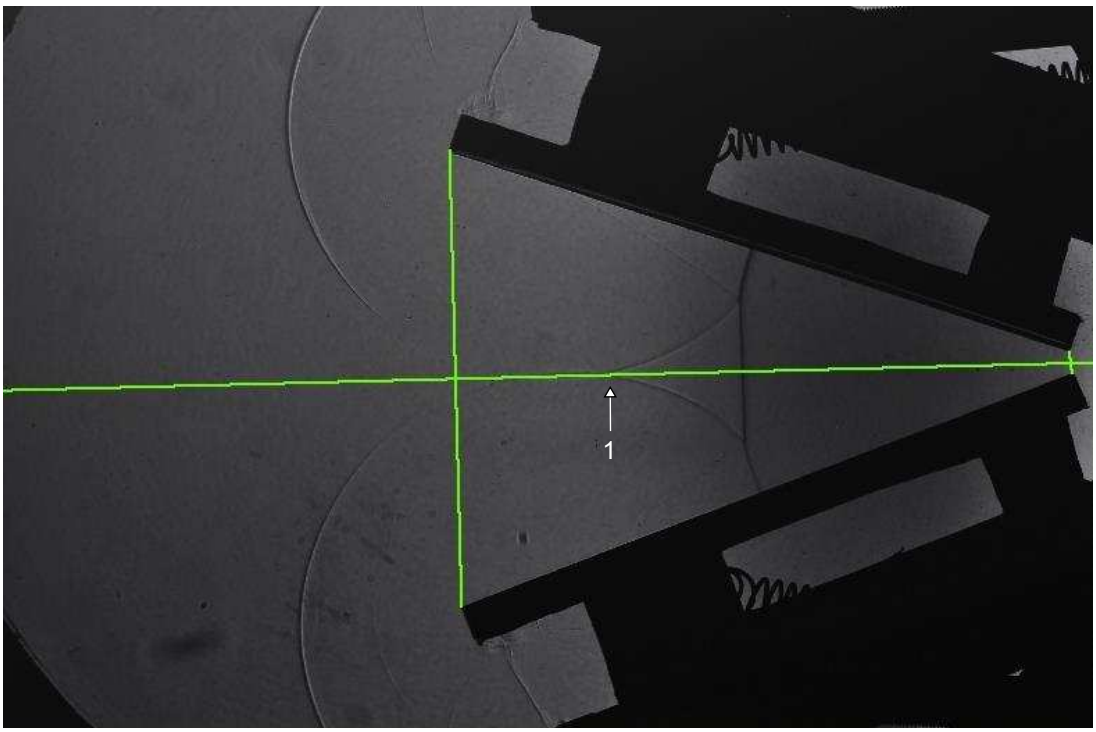

Figure 8.31: Shadowgraph of brass vs. aluminium at 70° and M1.3038

In Figure 8.32 and Figure 8.33, asymmetry can be seen in 2 main areas. In the area marked 1 which lies between the intersection points, the area above the centre line is larger than the area below the centreline. In area 2 which is between the triple points, reflected waves and incident shock wave, the area below the centre line is smaller than the area above the centreline. This indicates a larger angle of reflection from the bottom brass surface than the top aluminium surface.

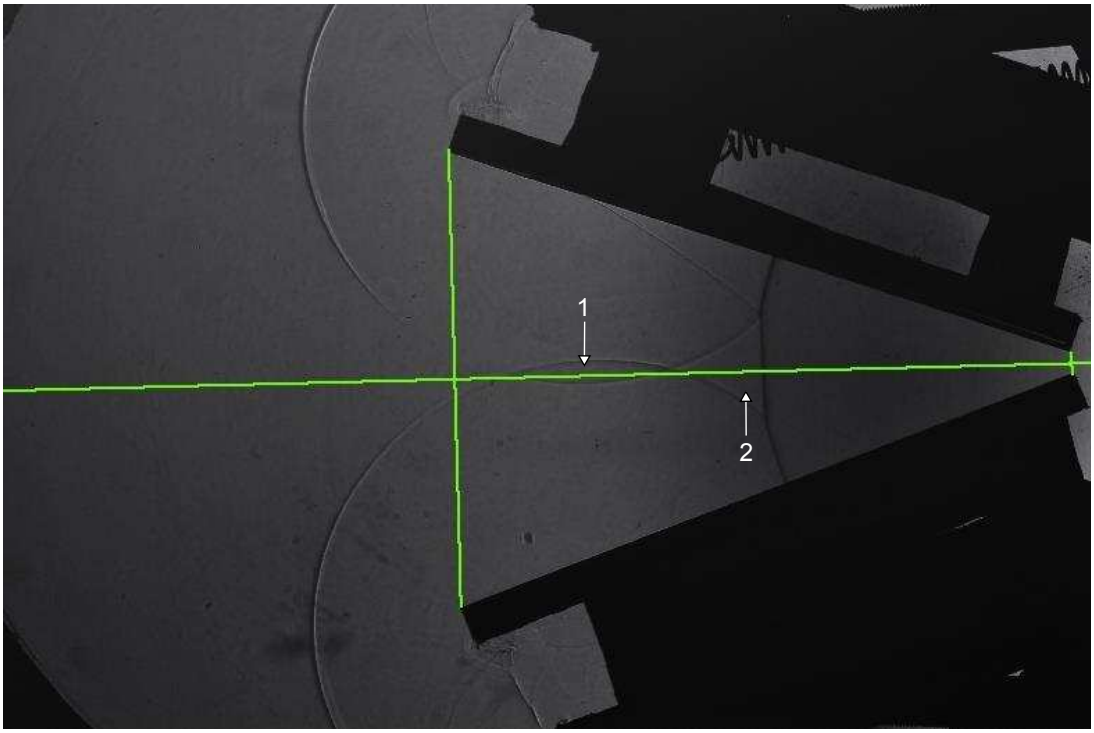

Figure 8.32: Shadowgraph of brass vs. aluminium at 70° and M1.3530

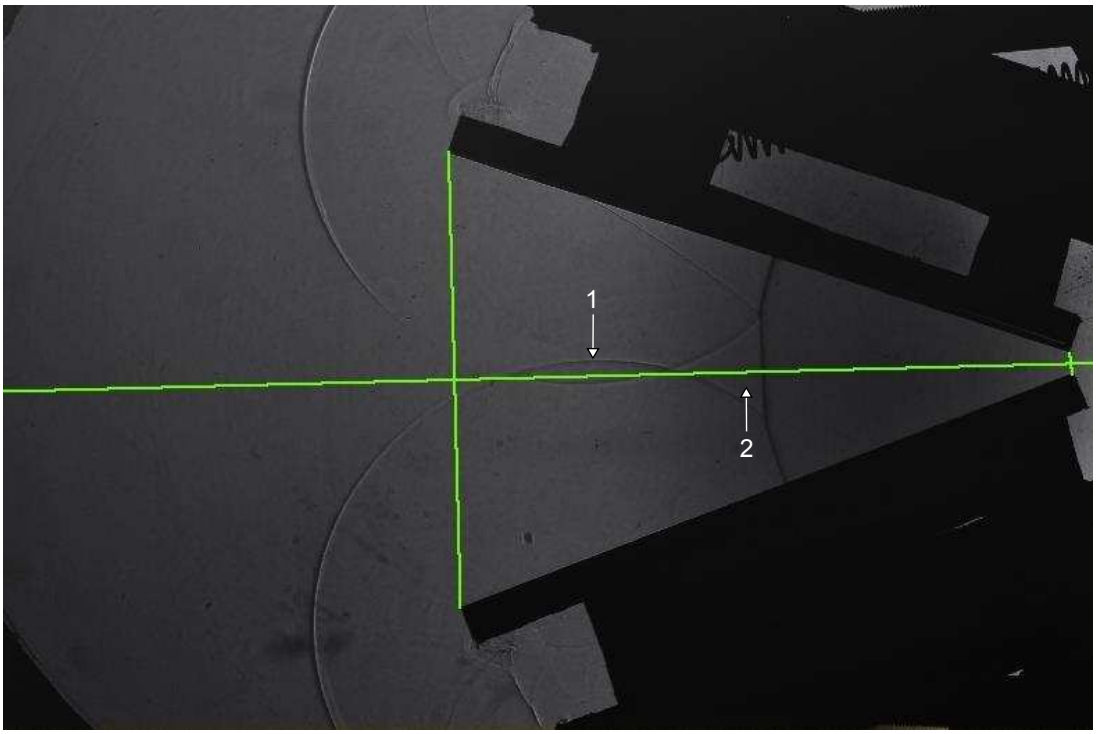

Figure 8.33: Shadowgraph of brass vs. aluminium at 70° and M1.3897

In Figure 8.34, no centreline was drawn as asymmetry in the reflection topology can be seen clearly. At point 1 the shock wave that has reflected back off the aluminium surface and shear layer intersect at a position closer to the trailing edge than at point 2 which is the corresponding intersection point of the 2nd reflected wave off the brass surface and shear layer. At point 3 and 4, the area between the surfaces and second shear layers have different sizes with the area at the top aluminium surface labelled point 3, being larger than the area at the brass surface labelled point 4. This means that more time has allowed for the triple point trajectory to develop away from the aluminium surface. This indicates that the initial reflected shock wave contacted the aluminium surface before the brass, showing that the original intersection points would have been closer to the aluminium test piece at the top.

Figure 8.34: Shadowgraph of brass vs. aluminium at 70° and M1.3954

In both Figure 8.35 and Figure 8.36 the intersection points of the reflected shock waves labelled point 1 lie slightly above the constructed centrelines. It can also be seen that the intersection of the triple points, labelled point 2 lies marginally above the centreline.

Additionally in Figure 8.36 the area between the reflected shock waves and shear layers are of different sizes with the area above the centre line shown by point 3 being larger than that below the centreline indicated by point 4.

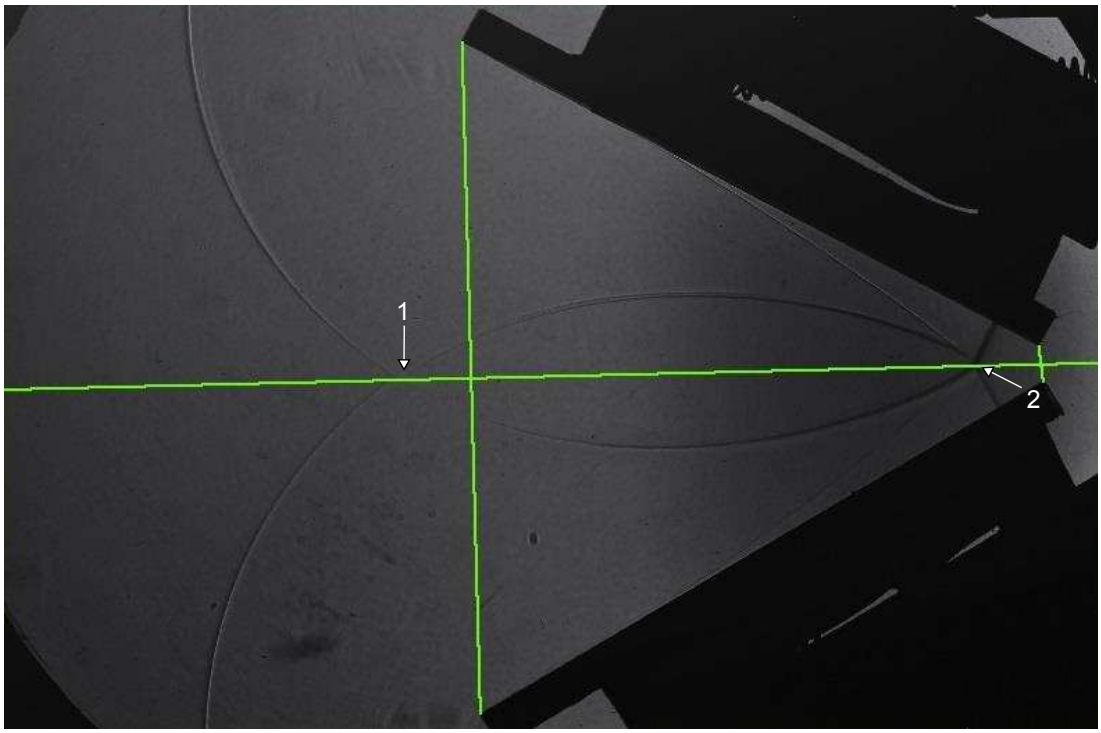

Figure 8.35: Shadowgraph of brass vs. aluminium at 60° and M1.3060

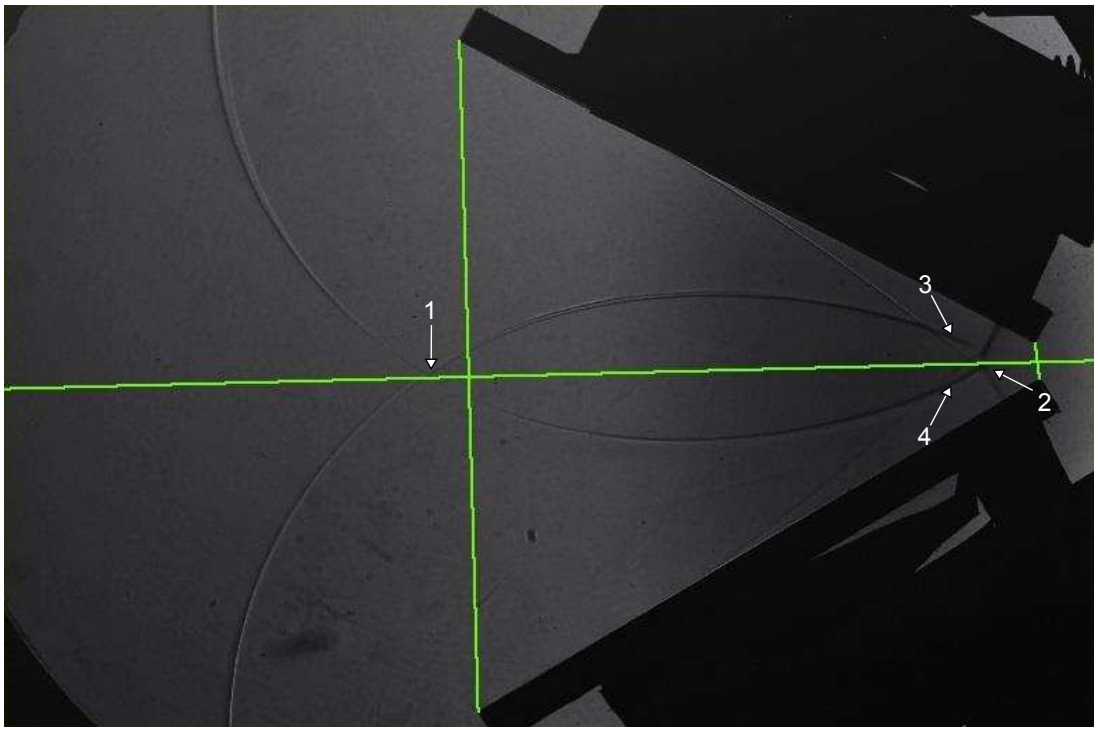

Figure 8.36: Shadowgraph of brass vs. aluminium at 60° and M1.3544

Figure 8.37 shows similar characteristics to the 70° cases seen in Figure 8.32 and Figure 8.33 where the areas between the centre line, reflected waves and incident waves are different. Additionally the intersection points of the reflected shock waves lie above the centreline.

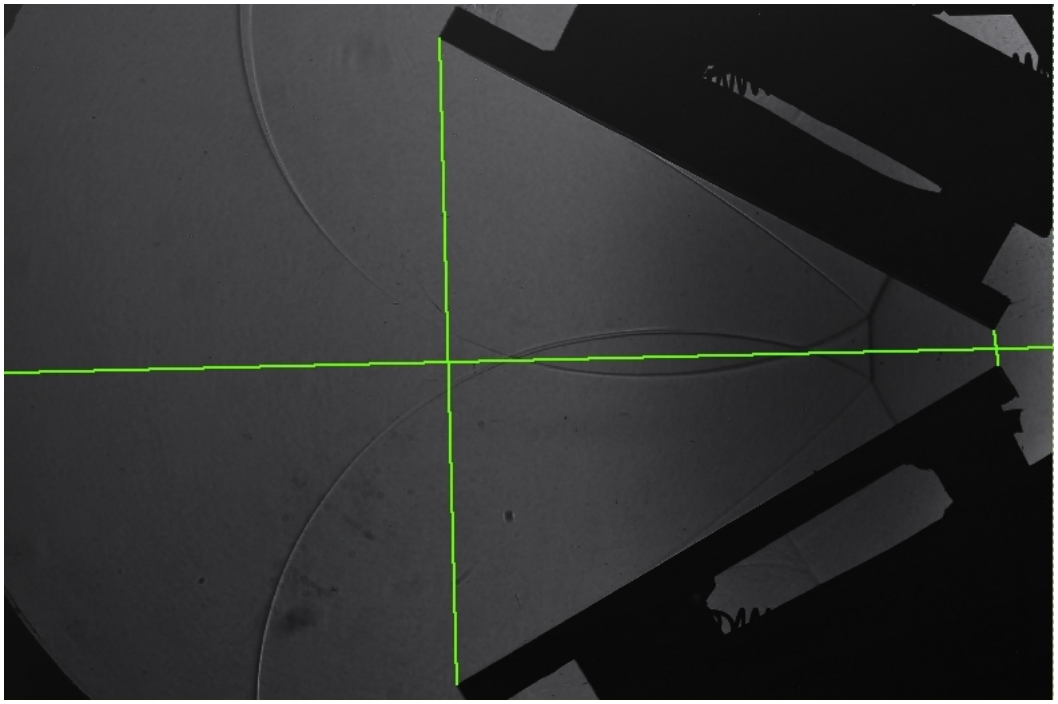

Figure 8.37: Shadowgraph of brass vs. aluminium at 60° and M1.3793

8.6.3 Glass vs. Copper

Figure 8.38, Figure 8.39 and Figure 8.40 show similar characteristics to those of the brass and aluminium test pieces, where, the intersection points of the reflected shock waves lie slightly above the centre line.

These points are not indicated on the images for clarity as they have been pointed out in previous images.

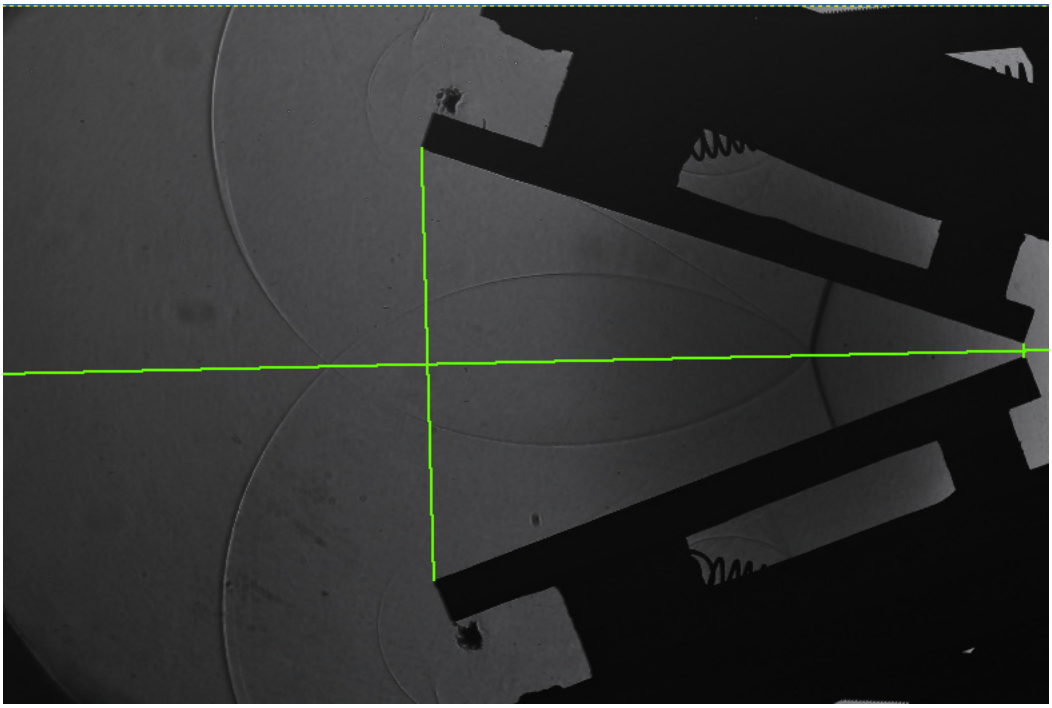

Figure 8.38: Shadowgraph of glass vs. copper at 70° and M1.3022

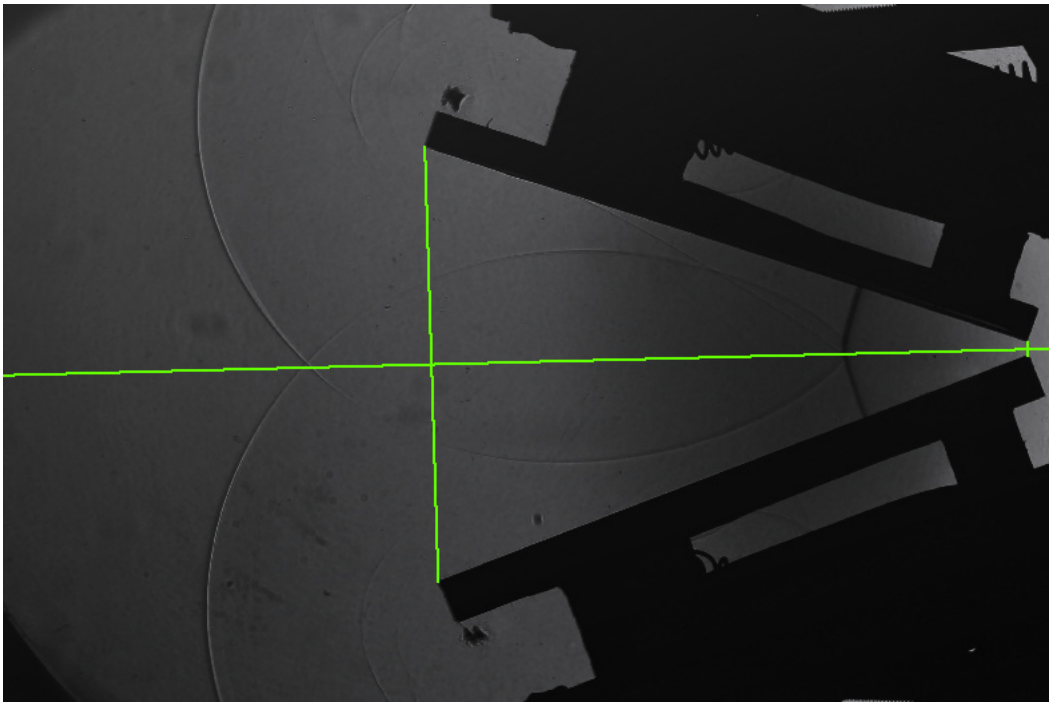

Figure 8.39: Shadowgraph of glass vs. copper at 70° and M1.3062

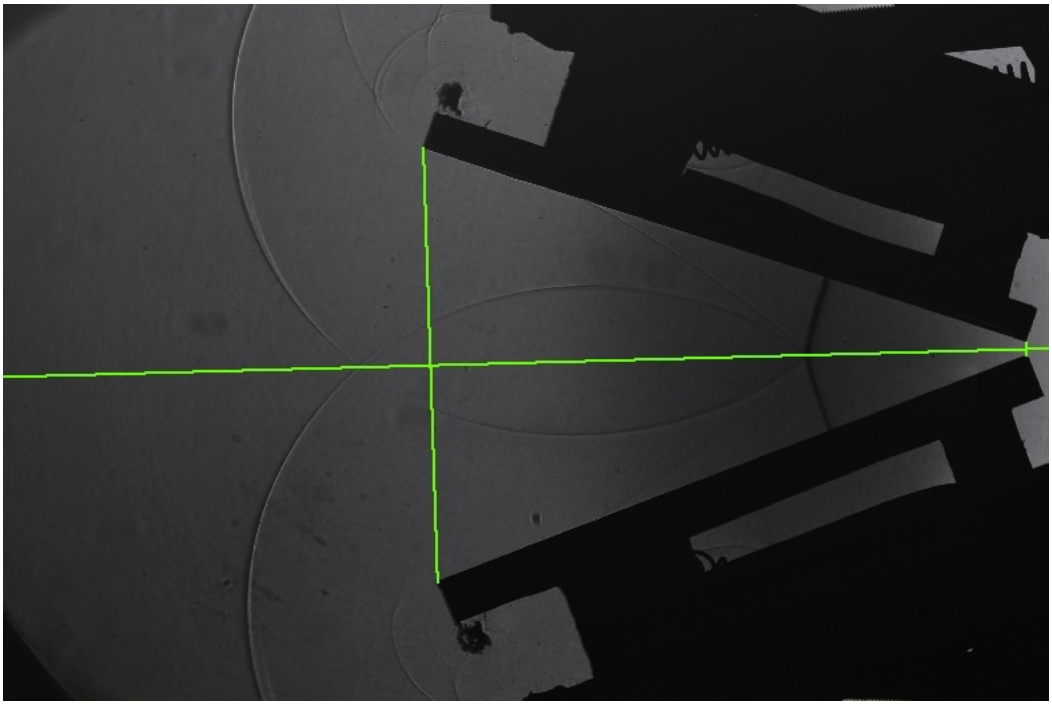

Figure 8.40: Shadowgraph of glass vs. copper at 70° and M1.3593

It can be seen in Figure 8.41, Figure 8.42 and Figure 8.43 that the intersection points of the reflected shock waves again lie above the centreline shown by points 1. Additionally there is asymmetry close to the triple points where the areas above indicated by points 2 and below indicated by points 3 the centreline, are different, with the area below the centreline being the smaller of the two.

In Figure 8.43 the area between the reflected shock waves at point 4 lies almost completely above the reflected shock wave.

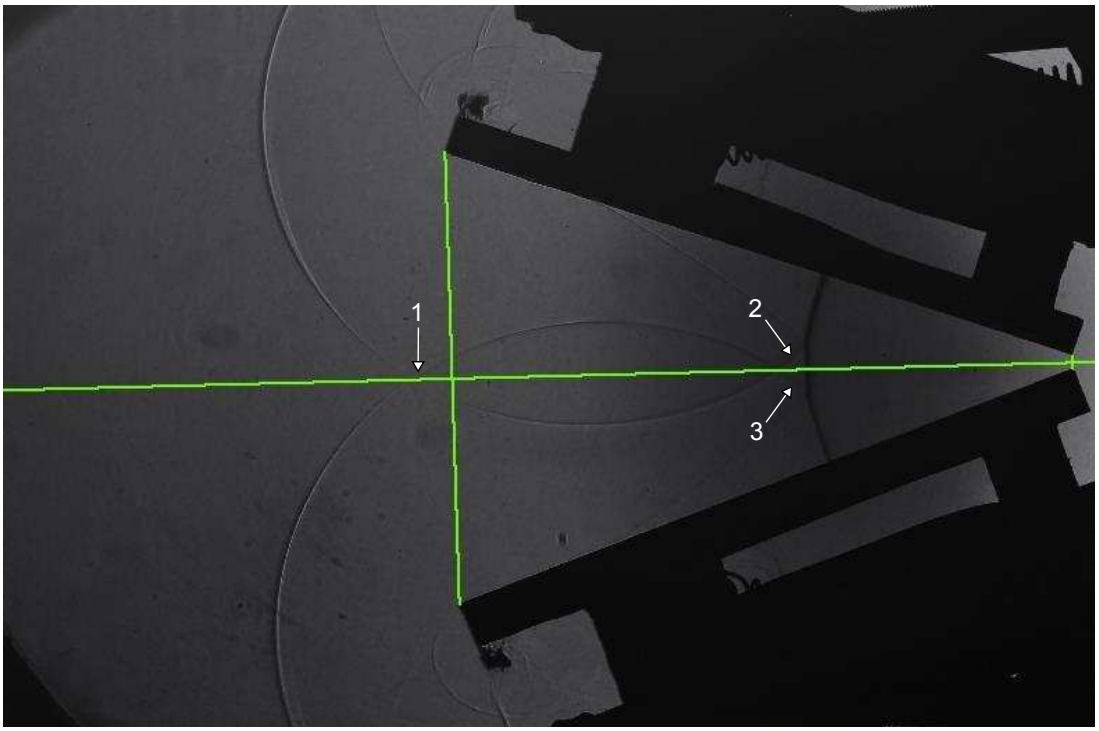

Figure 8.41: Shadowgraph of glass vs. copper at 70° and M1.3521

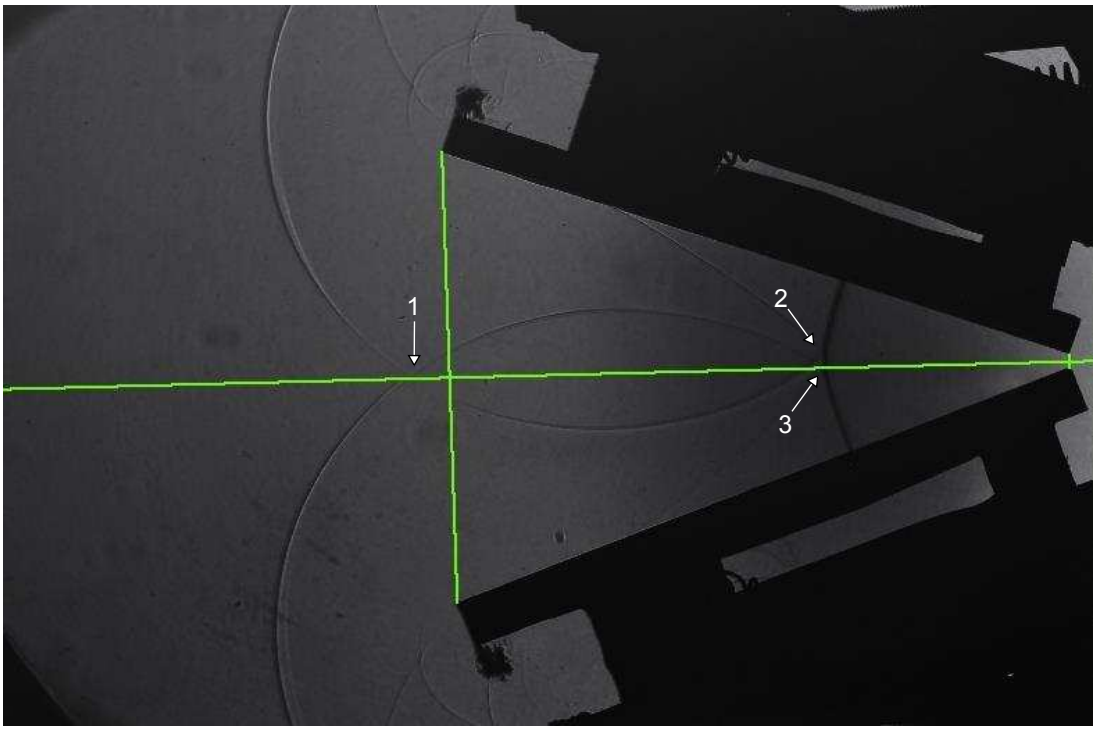

Figure 8.42: Shadowgraph of glass vs. copper at 70° and M1.3874

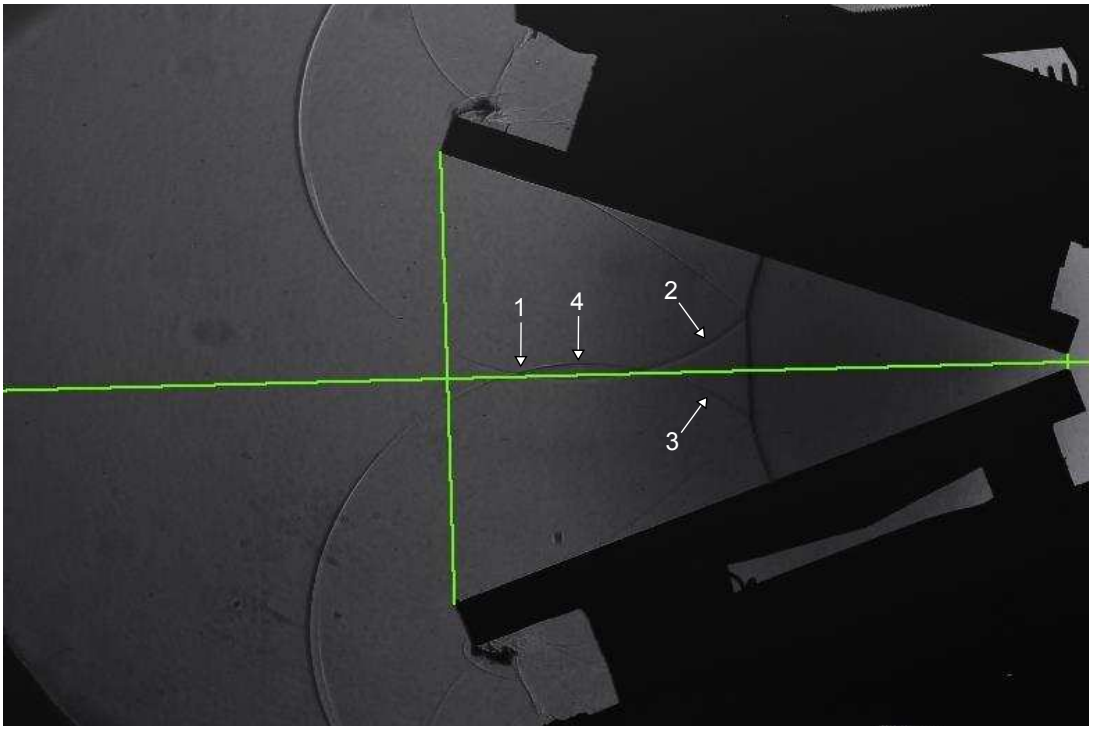

Figure 8.43: Shadowgraph of glass vs. copper at 70° and M1.3849

In Figure 8.44 two major differences can be observed that display asymmetry in the reflection topologies. The areas between the reflected shock wave and shear layer, before reflecting off the surfaces for a second time are different. These points are indicated 1 and 2. On the copper side of the shock tube at point 1 the area is smaller than the glass side at point 2.

The other major difference is the area between the shear layer and the reflected shock wave once it has reflected off the surfaces a second time, shown as points 3 and 4. At the copper surface indicated by point 3 the area is larger than at the glass surface indicated by point 4.

Both of these observations indicate that a reflected shock wave reaches the copper surface faster than the glass surface. This means that the initial intersection of the reflected shock waves is closer to the copper surface. This would be due to a larger reflection angle at the glass surface.

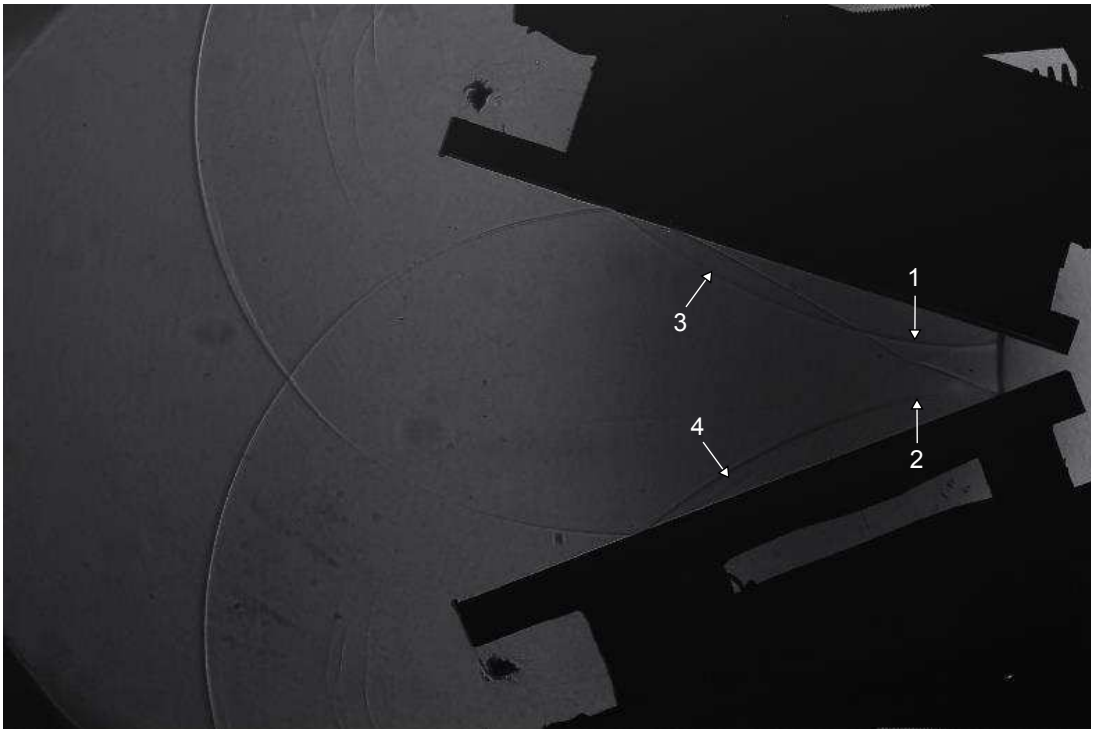

Figure 8.44: Shadowgraph of glass vs. copper at 70° and M1.3845

Figure 8.45 and Figure 8.46 both show similar asymmetry as seen in the 70° cases of the intersection points and areas being different sizes on opposite sides of the centreline.

This indicates that the qualitative results are consistent with different incidence angles as well as at different Mach numbers.

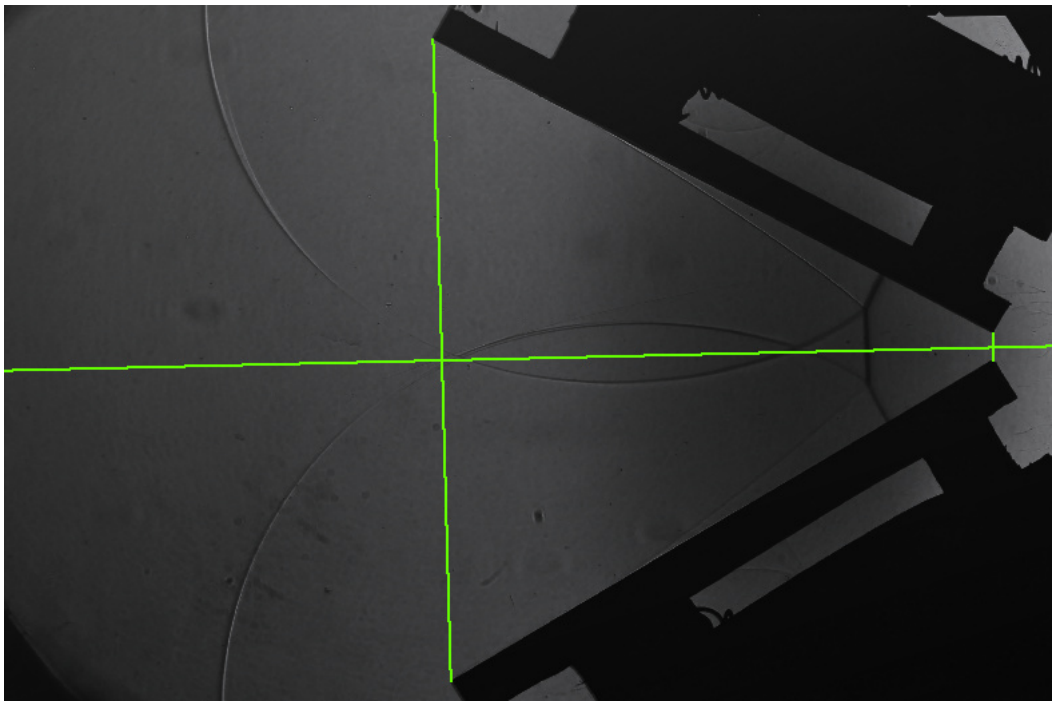

Figure 8.45: Shadowgraph of glass vs. copper at 60° and M1.3042

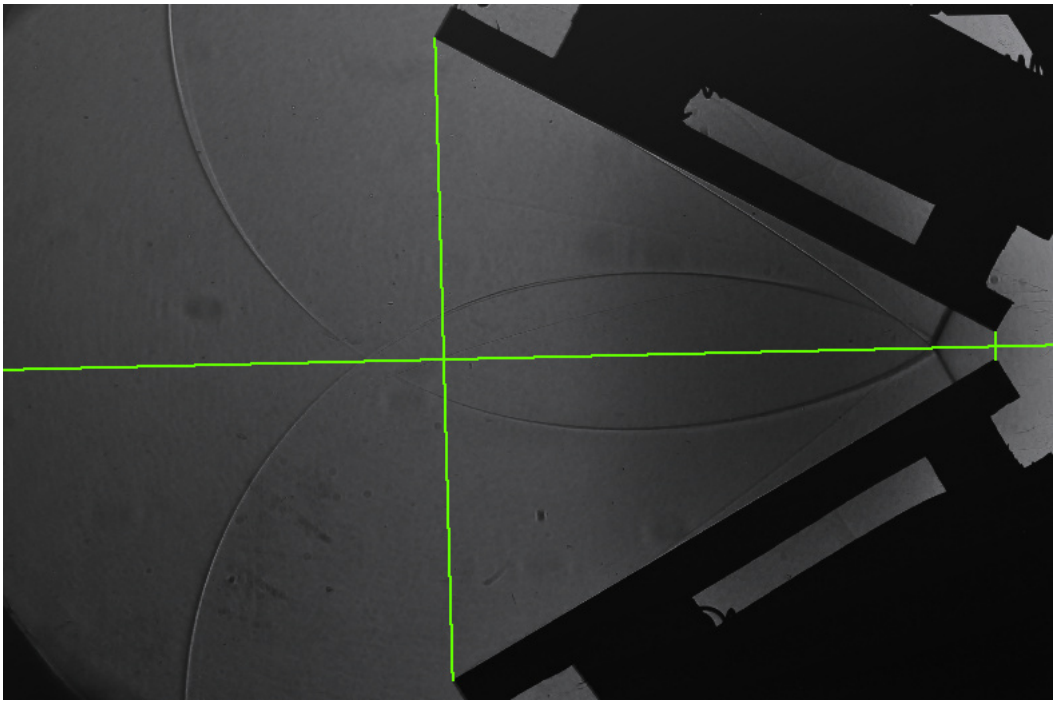

Figure 8.46: Shadowgraph of glass vs. copper at 60° and M1.3049

In Figure 8.47 the point that the reflected waves hit the surface of the two materials is different for the glass and copper. At the copper test piece labelled point 1, this point is further from the trailing edge than at the glass test piece labelled point 2.

Another observation is that the wave that reflects off the surface for a second time has progressed farther from the copper test piece than the glass test piece.

This observation is also seen in Figure 8.48. Here the distance between this second reflected shock wave and shear layer is smaller for the wave reflecting off the copper surface, than the wave reflecting off the glass surface.

Figure 8.47: Shadowgraph of glass vs. copper at 60° and M1.3534

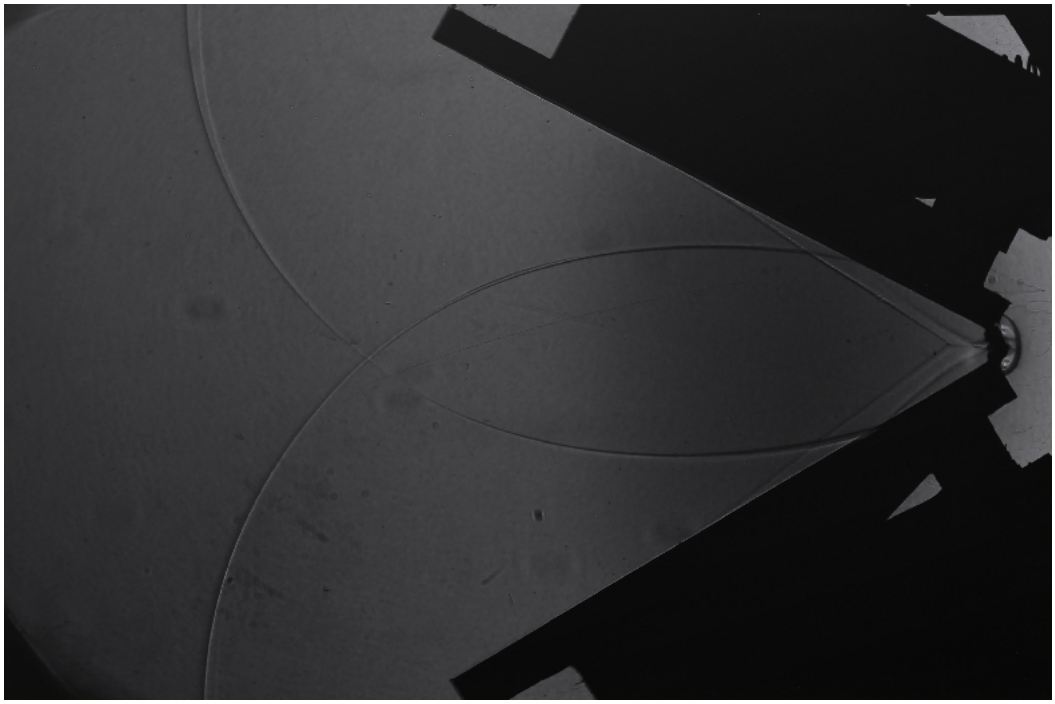

Figure 8.48: Shadowgraph of glass vs. copper at 60° and M1.3974

8.6.4 Copper vs. Glass (Reversed)

In the single qualitative test performed where glass and copper were reversed there is asymmetry visible between the reflected shock waves and shear layers as shown in Figure 8.49. As earlier mentioned, the glass test piece was broken after this test so additional tests could not be performed to verify, qualitatively that local buoyancy effects did not affect the reflection topologies. However, the limited data available from the quantitative and qualitative results do support that there is no local buoyancy effects present during a test.

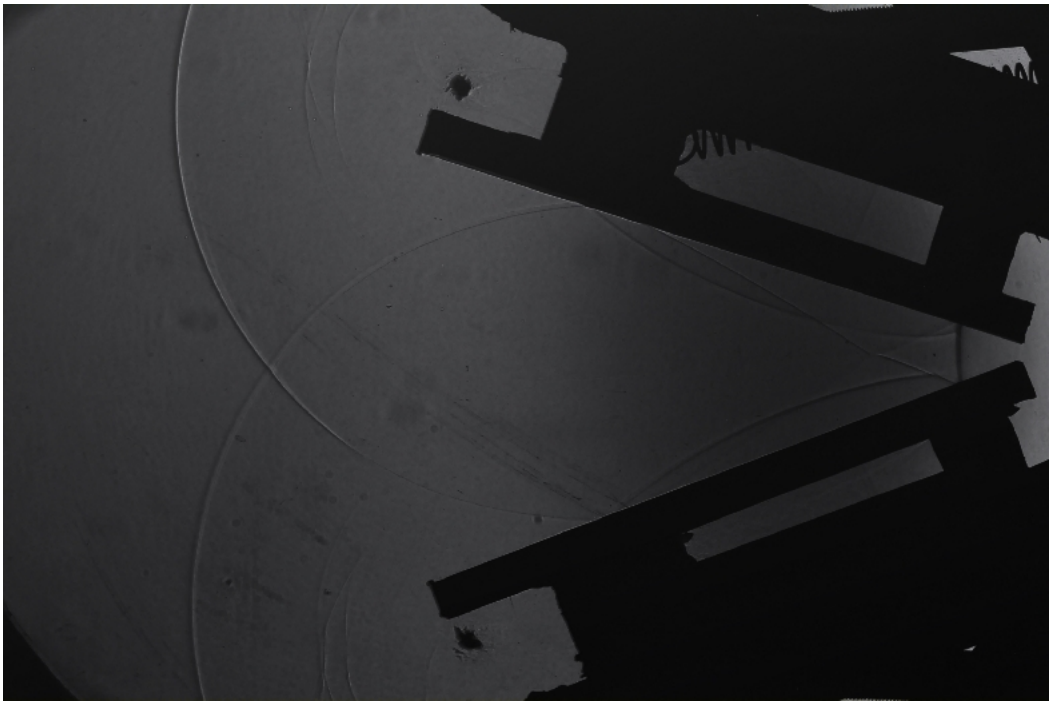

Figure 8.49: Shadowgraph of copper vs. glass (reversed) at 70° and M1.3835

8.7 Qualitative Trends and Analysis

All the images presented in the qualitative tests suggest a difference in reflection topologies based on the thermal conductivity of the materials tested.

For the control experiments of steel vs. steel, the reflection patterns were largely symmetrical about the centrelines with small deviations that could have been caused by small influences. These deviations were not present in every test and so are assumed not be a factor in the control experiments.

When materials of different thermal conductivity were used, consistent asymmetry in the reflection topologies was visible across both the brass-aluminium and glass-copper tests. In both cases, the material with a lower thermal conductivity was placed at the bottom of the shock tube. The intersection of the reflected waves being above the centre line indicates that the angle of reflection of these materials with lower thermal conductivity is larger than those with higher thermal conductivity.

The effects remain present even after the reflected shock wave has been able to reflect off the material surfaces for a second time.

These results support the quantitative results that the reflection angle is larger with a lower

thermal conductivity. It would be desirable to test other material pairs such as glass and brass or copper and aluminium. This would be beneficial in order to identify if the magnitude of the thermal conductivity affects the reflection angle as seen in the quantitative results

8.8 Leading Edges

Sample images were taken at earlier stages in tests to demonstrate that the leading edges could be adjusted to allow the shock wave to impact both leading edges simultaneously. Figure 8.50 shows that there is a slight difference in the distance between the leading edge at the top and the bottom and the incident shock wave. Figure 8.51 shows a case where the incident shock wave has just passed the leading edges and has moved evenly down both surfaces.

Figure 8.50: Shadowgraph of steel vs. steel at 70° and M1.3883

Figure 8.51: Shadowgraph of glass vs. copper at 70° and M1.3058

In the set-up of each test piece the leading edges were located using a set square referenced to the bottom of the shock tube, as it was decided that this was the most accurate way of alignment. This alignment method was chosen as it was assumed that the shock wave was normal to the longitudinal axis of the shock tube. Figure 8.52 and Figure 8.53 show that this was not always the case. In the two images, with the same materials, and the same incidence angle with comparable Mach numbers, the incident shock wave had different shapes. In Figure 8.52 the incident shock wave is straighter and is closer to touching both leading edges than in Figure 8.53, where there is a slight curve leading to the incident shock wave being closer to the bottom leading edge than the top. Although the design of the test rig and measures were taken to negate this effect, it can't be completely eliminated, as each test may have slightly different flow effects based on the real flow effects experienced in the bursting of the diaphragm. It is also not known if the shock wave will be perfectly normal to the shock tube's longitudinal axis.

Figure 8.52: Shadowgraph of glass vs. copper at 60° and M1.3062

Figure 8.53: Shadowgraph of glass vs. copper at 60° and M1.3053

Chapter 9 Conclusions

The primary investigation of this work was to determine if the thermal conductivity of the materials have an effect on the reflection angles of shock waves off these surfaces. The work was performed experimentally, as computational solvers assume surfaces to be adiabatic and smooth in the reflection process. The results obtained from the experimentation were analysed both quantitatively and qualitatively to determine the presence and magnitude of the thermal conductivity effects.

9.1 Experimentation and Material Limitations

The tests that were performed in the Large-Scale Diffraction Shock Tube, proved to be reproducible, due to the addition of a pneumatic pricker to the shock tube. This allowed bursting of diaphragms at predetermined pressures, which allowed safe operation as well as reproducible Mach numbers in the tests. The Mach numbers did vary slightly at each set diaphragm burst pressure, however this behaviour is to be expected as the temperatures in the laboratory varied slightly during hours of operation. These variations were small and are unlikely to have any effect on the results that were collected.

The use of a single-shot shadowgraph optical set-up produced results that were more accurate based on the measurement of quantitative results and the statistical approach than used in previous work. The resolution of the system was greatly improved and allowed for better visualisation of the flow fields.

It is noted though that the size of the test pieces as well as the observable flow field is limited by the size of the viewing area possible in the shock tube.

The materials were polished to as close to a smooth surface as was possible, yet there was still a variation in the surface roughness of the materials. Although this variation in roughness is present and viscous boundary layer growth will be different for the different materials, these

effects are considered to be negligible as the surface roughness of the materials are well below the hydraulic limit for smoothness proposed [**10**]. The only exception is that of brass, as the test piece was known not to be perfectly flat due to manufacturing limitations.

9.2 Comparison of Theoretical and Experimental Results

The comparison between the two-shock theory and experimental results is only applicable within the regular reflection domain. It was seen that glass, which had the lowest thermal conductivity and surface roughness, produced results that were the closes to the theoretical values as well as following the theoretical trends with increasing Mach number. This was to be expected as glass was the closest to a perfectly smooth, adiabatic surface as assumed in the theory. The materials with higher thermal conductivity all had smaller reflection angles than the theoretical values and did not always follow the theoretical trends with increasing Mach number.

9.3 Result Consistency Within Regular and Irregular Reflection Domains

It was evident in the regular reflection domain that with a higher thermal conductivity, the angle between the reflecting surface and the reflected shock wave was smaller. This was a consistent result in all of the regular reflection results, except for brass. The results from the brass test piece were displayed separately due to the constraints in its manufacturing.

For the irregular reflection cases, the angle between the reflected and incident shock waves was measured. This angle was larger for materials with a higher thermal conductivity. These results confirm the regular reflection cases, as based on the geometry of reflection topologies the angles between the reflection surfaces and the reflected shock waves would be smaller for materials with a higher thermal conductivity.

9.4 Pseudo-steady Reflection Topologies

In the testing used for this dissertation, only a single shot optical set up was used in order to visualise the flow field. This prevents a single test being analysed at multiple times.

It is seen though that there are small variations in the quantitative results at discrete Mach

numbers when tests were repeated. These small variations could indicate that the reflection patterns are not self-similar during the tests, however it is not conclusive proof.

Further testing with high speed imaging equipment could be used in addition to the single shot tests to verify these effects.

9.5 Quantitative and Qualitative Analysis

Both the quantitative and qualitative results indicate that there are thermal conductivity effects in the reflection of the shock waves off the surfaces. The qualitative tests showed this by asymmetry in the reflection topologies when test pieces of different materials were used. These results substantiated the angle measurements taken in the quantitative tests. The materials used show that there is graded difference in reflection angle based on the magnitude of the thermal conductivity of the material. This can be seen in the differences between the reflection angles off glass, copper and aluminium, with aluminium being an intermediate result between the copper and glass. This is to be expected as it has a thermal conductivity that lies between the thermal conductivities of the copper and glass.

The control experiments performed with two steel test pieces provided confidence in the experimental set up and test rig as the measured angles were the same at the top and bottom of the shock tube. Additionally for the steel experiments there was symmetry in the shadowgraph images.

It is also noted that there may have been slight curving of the incident shock waves due to flow effects in testing that are out of the shock tube operator's control. These were seen to be insignificant based on the very small standard deviation of the incidence angle measurements performed in the quantitative analysis.

The effect of the thermal conductivity allows heat to travel from the gas behind the incident shock wave into the test pieces. This causes the viscosity of the gas close to the surface to be different locally at the different materials. This would change the flow characteristics that the reflected shock waves are experiencing, causing a difference in the reflection topologies. Although this effect is due to the viscosity of the gas, it is not caused by the surface roughness and viscous boundary layer. It is due to a thermal boundary layer dependant on the thermal conductivity of the reflection surface material.

9.6 Validation of Previous Work

The results of this testing confirm the results of the previous work performed, indicating that the reflection angles of materials with higher thermal conductivities is smaller than those of larger thermal conductivities. It could not be conclusively proven if the reflection patterns where pseudo-steady throughout the duration of the test, due to the experimental set up that was chosen for testing.

Chapter 10 Recommendations

This chapter outlines the recommendations made for further research and possible improvements to the testing procedure that would investigate aspects that may not have been conclusively proven by this experimentation.

- It would be useful to perform tests with high speed imaging equipment in order to ascertain if the shock wave reflection topologies are indeed self-similar as observed in previous work.
- Although there was better resolution and accuracy in this testing, using a light source with a shorter exposure time than 1.5 microseconds would reduce the uncertainty in the results. A 532nm YAG laser with an exposure time of 20 nanoseconds was explored for this project, unfortunately, it was unable to be procured in time to complete this project.
- Thermal imaging equipment could possibly be used in order to detect the rate and magnitude of heat transfer into the test pieces as well as the change in temperature of the air close to the surfaces behind the incident shock waves.
- It is suggested that further testing be done with additional materials and to combine them in different arrangements to provide a better sampling of data.
- A larger set of incidence angles could be tested to further characterise the degree of the effect and to test the trends seen in theoretical analysis. In this testing the incidence angles were limited to the design of the shock tube used as well as to clearly define results between the regular and irregular reflection domains. Testing close to the transition region between these domains may yield results as to the persistence of regular reflection.
- A further limitation of the testing was the safe operating pressures in the shock tube, limiting the possible range of Mach numbers that could be tested. Testing at higher Mach numbers would increase the temperature difference across the shock waves, possibly increasing the heat flux into the reflection surfaces.

- It is suggested to test materials with the same surface roughnesses, at a value higher than the hydraulic limit for smoothness to confirm the thermal effects present and to determine if these effects persist past the hydraulic limits.

References

[1] R. Berry. *Wall Conductivity Effects in Shock Wave Reflection*. Research Project. School of Mechanical, Industrial and Aeronautical Engineering. University of the Witwatersrand. Johannesburg. 2015.

[2] F. Barbosa, B. Skews. *Experimental Confirmation of the von Neumann Theory of Shock Wave Reflection Transition*. pp. 263-282. J. Fluid Mech. vol. 472. Cambridge University Press. Cambridge. 2002.

[3] C. de Saxe. *Boundary Layer Effects Due to Wall Conductivity, Roughness and Surface Defects in Shock Reflection*. Research Project. School of Mechanical, Industrial and Aeronautical Engineering. University of the Witwatersrand. Johannesburg. 2009.

[4] Y. Jogessar. *Boundary Layer Effects Due to Wall Angle and Mach Number in Shock Reflection*. Research Project. School of Mechanical, Industrial and Aeronautical Engineering. University of the Witwatersrand. Johannesburg. 2009.

[5] M. Potter, D. Wiggert, B. Ramadan. *Mechanics of Fluids*. 4th Edition. Cengage Learning. Stamford. 2012.

[6] National Aeronautics and Space Administration. *Specific Heat Capacity*. Glenn Research Center. INTERNET. https://www.grc.nasa.gov/www/BGH/realspec.html. Accessed 13-06-2016.

[7] C. Tropea, A. Yarin, J. Foss & Editors. *Handbook of Experimental Fluid Mechanics*. Springer. Berlin. 2007.

[8] J. Anderson. *Modern Compressible Flow*. 3rd Edition. McGraw Hill. New York. 2004.

[9] B. W. Skews. *Course Notes-MECN4024 Compressible Flow*. University of the Witwatersrand. Johannesburg. 2015.

[10] G. Ben-Dor. *Shock Wave Reflection Phenomena*. Springer-Science+Business media. New York. 2007.

[11] B. W. Skews. *The Construction and Calibration of a Gas Shock Tube.* Masters of Science in Engineering. University of the Witwatersrand. Johannesburg. 1961.

[12] J. K. Wright. *Shock Tubes.* Methuen & Co. Ltd. London. 1961.

[13] Eastman Kodak Company. *Schlieren Photography.* New York. 1960.

[14] H. Schlichting. *Boundary-Layer Theory.* 6th Edition. McGraw Hill. New York. 1968.

[15] F. M. White. *Fluid Mechanics.* 5th Edition. McGraw Hill. New York. 2003.

[16] F. Kreith. *Principles of Heat Transfer.* 2nd Edition. International Textbook Company. Pennsylvania. 1965.

[17] H.G. Hornung, J.R. Taylor. *Transition from Regular to Mach Reflection of Shock Waves Part 1. The Effect of Viscosity in the Pseudosteady Case.* J. Fluid Mech. vol. 123 p., 143-153. 1982.

[18] Mark H. *The Interaction of a Reflected Shock Wave with the Boundary Layer in a Shock Tube.* Tech. rep., NACA TM 1418. 1958

[19] L.F. Henderson, W.Y. Crutchfield, R.J. Virgona. *The Effects of Thermal Conductivity and Viscosity of Argon on Shock Waves Diffracting Over Rigid Ramps.* J. Fluid Mech. vol.331 pp. 1-36. 1997.

[20] A. A. van Netten, J. M. Dewey, T. von Haimberger. *The Effects of Surface Temperature on the Shock Wave Reflection Process.* Proc. 11th Mach Reflection Symposium. 1994. Victoria, Canada. University of Victoria.

[21] B.W. Skews, R. Berry, R.T. Paton. *Effect Of Surface Properties on Shock Wave Reflection.* Proceedings of the 12th International Conference on Heat Transfer, Fluid Mechanics and Thermodynamics. Spain. 2016.

[22] The Engineering Toolbox. *Thermal Conductivity of Common Materials and Gases.* Glenn Research Center. INTERNET. http://www.engineeringtoolbox.com/thermal-conductivity-d_429.html. Accessed 20-06-2016.

[23] L. Kirkup. *Experimental Methods - An Introduction to the Analysis and Presentation of Data..* John Wiley and Sons Australia, Ltd. Milton Queensland. 1994.

Appendix A Instrumentation

This appendix contains the details of equipment used in the testing procedures for the experimentation performed.

Camera

Nikon D-90
Serial number: 6181747

Oscilloscope

Yokogawa DL708E 8ch Digital Scope
Model:701820
Serial number: 12W713778 G

Signal Conditioners

PCB Piezotronics I.C.P Power Supply
Model: 482A

Time Delay Box

ElectroDI Programmable Time Delay Unit
Model: Adjustable trigger and output
Min. delay: 50 microseconds
Max. delay: 99 998 microseconds

Inclinometer

Insize Digital Level and Protractor Code 2178-1
Serial number: 3101120231
Range : 0°-180°
Resolution: 0.1° (=1.745 mm/m)
Accuracy: ±0.1°

Surface Roughness Tester

Time TR220 Roughness Tester
Serial number: 911834403226
Resolution: 0.001μm
Accuracy: ±0.001μm

Appendix B Experimental Documents and Results

This appendix contains the Mach number pressure calibration chart for natural bursts shown in Figure B.1, the experimental test log data tabulated in Table B.1 and the tabulated results for the averaged readings of angles measured in chapter 7.

B.1 Experimental Documents and Observations

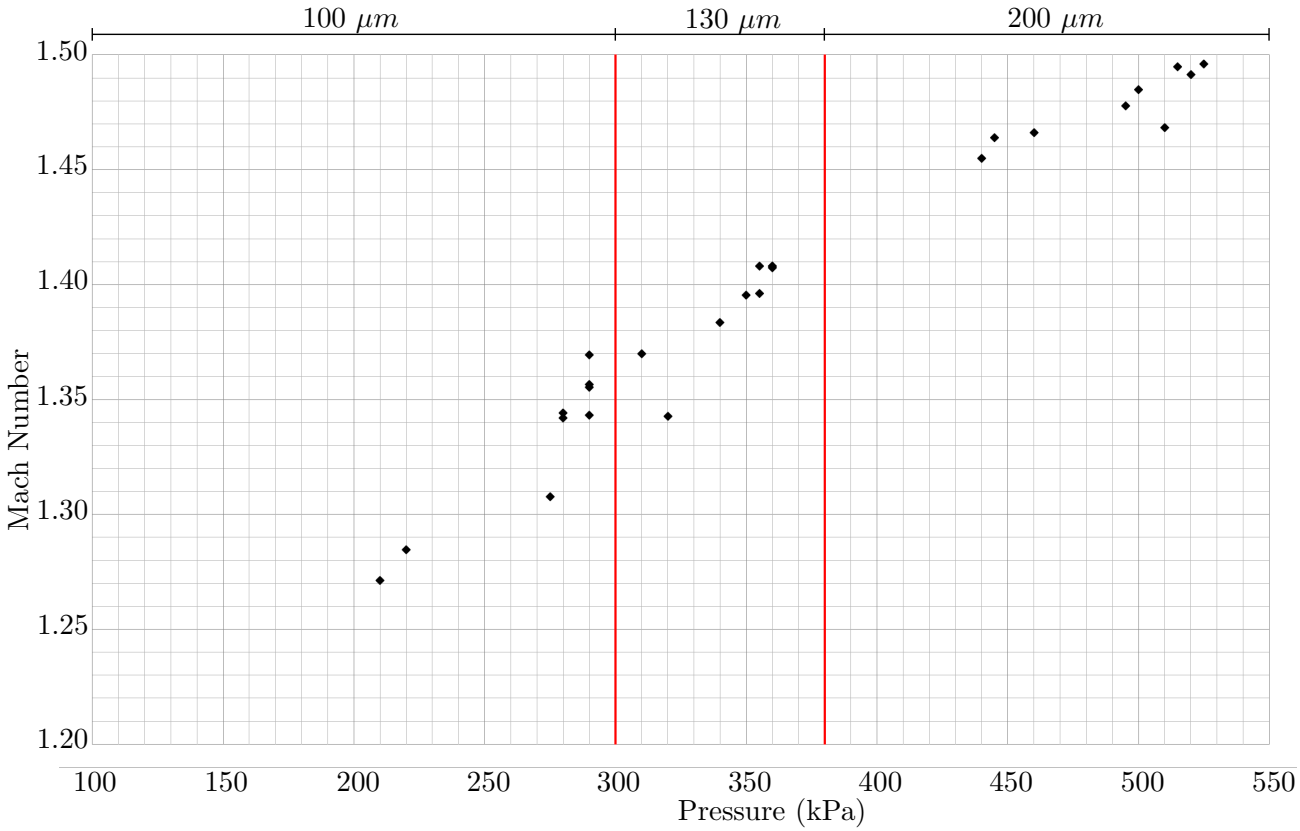

Figure B.1: Calibration of Mach number vs. Pressure for natural burst.

Table B.1: Experimental test log

Date	Test Number	Material	Diaphragm Thickness (μm)	Angle ($^\circ$)	Temperature ($^\circ C$)	Mach Number
23/01/2017	2	Steel-Steel	100	20	25.6	1.2990
	3	Steel-Steel	100	20	25.2	1.2892
	5	Steel-Steel	100	20	24.8	1.2900
	6	Steel-Steel	100	20	26.0	1.2990
24/01/2017	1	Steel-Steel	130	20	24.4	1.3144
	2	Steel-Steel	100	20	24.8	1.3135
	3	Steel-Steel	130	20	24.6	1.3635
	4	Steel-Steel	130	20	25.8	1.3481
	5	Steel-Steel	130	20	25.8	1.3608
	7	Steel-Steel	200	20	25.2	1.3883
	8	Steel-Steel	200	20	25.2	1.3883
	9	Steel-Steel	200	20	25.2	1.4018
	10	Steel-Steel	200	20	25.5	1.3876
	11	Steel-Steel	100	30	25.4	1.3122
25/01/2017	1	Steel-Steel	100	30	24.2	1.3030
	2	Steel-Steel	100	30	24.4	1.3025
	3	Steel-Steel	130	30	24.5	1.3510
	4	Steel-Steel	130	30	25.0	1.3499
	5	Steel-Steel	130	30	25.2	1.3494
	6	Steel-Steel	200	30	24.8	1.3919
	7	Steel-Steel	200	30	24.8	1.3893
	8	Steel-Steel	200	30	24.8	1.3893

Table B.1: Experimental test log

Date	Test Number	Material	Diaphragm Thickness (μm)	Angle ($^\circ$)	Temperature ($^\circ C$)	Mach Number
25/01/2017	9	Steel-Steel	100	50	27.0	1.3087
	10	Steel-Steel	100	50	25.4	1.3003
	11	Steel-Steel	100	50	25.8	1.2995
	12	Steel-Steel	130	50	25.8	1.3608
26/01/2017	1	Steel-Steel	130	50	24.0	1.3521
	2	Steel-Steel	130	50	24.1	1.3519
	3	Steel-Steel	200	50	24.0	1.3911
	4	Steel-Steel	200	50	24.0	1.3911
	5	Steel-Steel	200	50	24.2	1.3907
	8	Steel-Steel	100	54	24.2	1.3030
	10	Steel-Steel	100	54	24.4	1.2909
	11	Steel-Steel	130	54	24.4	1.3144
	12	Steel-Steel	130	54	24.8	1.3503
30/01/2017	1	Steel-Steel	130	54	23.4	1.3535
	2	Steel-Steel	130	54	23.5	1.3533
	3	Steel-Steel	200	54	23.6	1.3921
	4	Steel-Steel	200	54	23.8	1.3849
	5	Steel-Steel	200	54	23.8	1.3849
	6	Brass-Aluminium	100	20	23.8	1.3038
	7	Brass-Aluminium	100	20	23.8	1.3038
	8	Brass-Aluminium	100	20	23.6	1.3102
	9	Brass-Aluminium	130	20	23.6	1.3530

Table B.1: Experimental test log

Date	Test Number	Material	Diaphragm Thickness (μm)	Angle ($^\circ$)	Temperature ($^\circ C$)	Mach Number
30/01/2017	10	Brass-Aluminium	130	20	23.8	1.3526
	11	Brass-Aluminium	130	20	23.6	1.3530
31/01/2017	1	Brass-Aluminium	200	20	22.2	1.3887
	2	Brass-Aluminium	200	20	22.4	1.3686
	3	Brass-Aluminium	200	20	22.2	1.3954
	4	Brass-Aluminium	100	30	22.8	1.3060
	5	Brass-Aluminium	100	30	23.0	1.3056
	6	Brass-Aluminium	100	30	22.8	1.3060
	7	Brass-Aluminium	130	30	22.8	1.3549
	8	Brass-Aluminium	130	30	23.2	1.3540
	9	Brass-Aluminium	130	30	23.0	1.3544
	10	Brass-Aluminium	200	30	23.2	1.3930
	11	Brass-Aluminium	200	30	23.6	1.3921
	12	Brass-Aluminium	200	30	23.4	1.3793
1/02/2017	1	Brass-Aluminium	100	50	22.8	1.3060
	2	Brass-Aluminium	100	50	22.8	1.3060
	3	Brass-Aluminium	100	50	23.0	1.3056
	4	Brass-Aluminium	130	50	23.0	1.3544
	5	Brass-Aluminium	130	50	23.1	1.3542
	6	Brass-Aluminium	130	50	24.0	1.3521
	8	Brass-Aluminium	200	50	24.4	1.3902
	9	Brass-Aluminium	200	50	24.8	1.3893

Table B.1: Experimental test log

Date	Test Number	Material	Diaphragm Thickness (μm)	Angle ($^\circ$)	Temperature ($^\circ C$)	Mach Number
1/02/2017	10	Brass-Aluminium	200	50	25.0	1.3888
	11	Brass-Aluminium	100	54	24.5	1.2907
	12	Brass-Aluminium	100	54	24.6	1.3021
	13	Brass-Aluminium	100	54	24.8	1.3017
2/02/2017	2	Brass-Aluminium	130	54	23.9	1.3524
	3	Brass-Aluminium	130	54	23.8	1.3526
	4	Brass-Aluminium	130	54	24.4	1.3512
	5	Brass-Aluminium	200	54	24.8	1.3893
	6	Brass-Aluminium	200	54	24.8	1.3893
	7	Brass-Aluminium	200	54	24.6	1.3897
	8	Glass-Copper	100	54	25.6	1.3058
	9	Glass-Copper	100	54	25.8	1.3054
	10	Glass-Copper	100	54	25.5	1.3001
3/02/2017	1	Glass-Copper	130	54	23.0	1.3544
	2	Glass-Copper	130	54	23.2	1.3540
	3	Glass-Copper	130	54	23.4	1.3535
	4	Glass-Copper	200	54	23.8	1.3916
	5	Glass-Copper	200	54	24.0	1.3911
	6	Glass-Copper	200	54	24.0	1.3911
6/02/2017	1	Glass-Copper	100	50	24.0	1.3046
	2	Glass-Copper	100	50	24.3	1.3039
	3	Glass-Copper	100	50	24.4	1.3037

Table B.1: Experimental test log

Date	Test Number	Material	Diaphragm Thickness (μm)	Angle ($^\circ$)	Temperature ($^\circ C$)	Mach Number
6/02/2017	4	Glass-Copper	100	50	24.4	1.3025
	5	Glass-Copper	130	50	24.8	1.3516
	7	Glass-Copper	130	50	25.0	1.3537
	8	Glass-Copper	130	50	25.2	1.3532
	9	Glass-Copper	200	50	25.4	1.3986
	10	Glass-Copper	200	50	25.2	1.3950
	12	Glass-Copper	200	50	25.4	1.3919
7/02/2017	1	Glass-Copper	100	30	23.6	1.3066
	2	Glass-Copper	100	30	24.7	1.3042
	3	Glass-Copper	100	30	24.4	1.3049
	4	Glass-Copper	100	30	23.8	1.3062
	5	Glass-Copper	100	30	24.2	1.3053
	6	Glass-Copper	130	30	24.6	1.3508
	7	Glass-Copper	130	30	25.0	1.3524
	8	Glass-Copper	130	30	24.0	1.3534
	9	Glass-Copper	200	30	24.8	1.3893
	10	Glass-Copper	200	30	24.4	1.3902
	11	Glass-Copper	200	30	24.2	1.3974
	12	Glass-Copper	100	20	25.1	1.3022
	13	Glass-Copper	100	20	24.6	1.2905
	14	Glass-Copper	100	20	24.6	1.2790
8/02/2017	2	Glass-Copper	100	20	23.8	1.3062

Table B.1: Experimental test log

Date	Test Number	Material	Diaphragm Thickness (μm)	Angle ($^\circ$)	Temperature ($^\circ C$)	Mach Number
8/02/2017	3	Glass-Copper	100	20	24.0	1.3058
	4	Glass-Copper	130	20	24.0	1.3521
	5	Glass-Copper	130	20	24.2	1.3593
	6	Glass-Copper	130	20	24.4	1.3512
	7	Glass-Copper	130	20	24.6	1.3546
	9	Glass-Copper	200	20	25.6	1.3874
15/02/2017	1	Glass-Copper	200	20	23.8	1.3916
	2	Glass-Copper	200	20	23.8	1.3849
	3	Glass-Copper	200	20	24.0	1.3845
	4	Copper-Glass	200	20	24.4	1.3835
	6	Copper-Glass	100	20	24.5	1.3141

B.2 Experimental Results

B.2.1 Regular reflection results

Table B.2: 36° Glass results

Intended Incidence angle	36				
Material	Glass				
Mach Number	Average actual incidence angle	Actual incidence angle std. deviation	Average Reflection angle	Reflection angle std. deviation	Reflection angle error
1.3058	36.242	0.163	33.184	0.297	0.593
1.3054	36.146	0.146	33.242	0.400	0.799
1.3544	36.228	0.212	32.410	0.377	0.754
1.354	36.184	0.218	32.388	0.371	0.742
1.3916	36.200	0.213	32.006	0.229	0.458
1.3911	36.190	0.228	31.492	0.157	0.315

Table B.3: 36° Copper results

Intended Incidence angle	36				
Material	Copper				
Mach Number	Average actual incidence angle	Actual incidence angle std. deviation	Average Reflection angle	Reflection angle std. deviation	Reflection angle error
1.3058	36.172	0.225	30.616	0.373	0.745
1.3054	36.140	0.185	31.100	0.184	0.368
1.3544	36.164	0.213	30.790	0.373	0.745
1.3540	36.112	0.193	30.846	0.358	0.716
1.3916	36.192	0.234	30.498	0.342	0.684
1.3911	36.146	0.242	30.202	0.371	0.743

Table B.4: 36° Brass results

Intended Incidence angle	36				
Material	Brass				
Mach Number	Average actual incidence angle	Actual incidence angle std. deviation	Average Reflection angle	Reflection angle std. deviation	Reflection angle error
1.2907	36.034	0.067	32.312	0.181	0.362
1.3021	36.116	0.149	32.414	0.198	0.396
1.3524	36.194	0.148	32.300	0.129	0.259
1.3526	36.098	0.176	32.326	0.348	0.696
1.3893	36.076	0.137	32.146	0.264	0.528
1.3893	36.206	0.238	32.042	0.396	0.792

Table B.5: 36° Aluminium results

Intended Incidence angle	36				
Material	Aluminium				
Mach Number	Average actual incidence angle	Actual incidence angle std. deviation	Average Reflection angle	Reflection angle std. deviation	Reflection angle error
1.2907	36.060	0.077	31.518	0.269	0.539
1.3021	36.082	0.097	31.358	0.302	0.603
1.3524	36.114	0.157	31.184	0.286	0.572
1.3526	36.084	0.149	30.918	0.331	0.661
1.3893	36.086	0.134	30.952	0.239	0.478
1.3893	36.206	0.286	31.394	0.375	0.750

Table B.6: 36° Steel bottom results

Intended Incidence angle	36				
Material	Steel Bottom				
Mach Number	Average actual incidence angle	Actual incidence angle std. deviation	Average Reflection angle	Reflection angle std. deviation	Reflection angle error
1.3030	36.254	0.236	30.808	0.262	0.524
1.2909	36.386	0.215	31.458	0.190	0.380
1.3144	36.110	0.142	31.554	0.368	0.735
1.3503	36.182	0.215	31.462	0.188	0.376
1.3535	36.394	0.243	32.176	0.286	0.573
1.3533	36.342	0.258	31.640	0.199	0.399
1.3921	36.152	0.123	31.324	0.355	0.710
1.3849	36.174	0.194	31.386	0.352	0.703

Table B.7: 36° Steel top results

Intended Incidence angle	36				
Material	Steel Top				
Mach Number	Average actual incidence angle	Actual incidence angle std. deviation	Average Reflection angle	Reflection angle std. deviation	Reflection angle error
1.3030	36.142	0.193	30.944	0.388	0.776
1.2909	36.116	0.161	30.962	0.285	0.570
1.3144	36.034	0.090	31.430	0.343	0.687
1.3503	36.094	0.138	31.558	0.195	0.391
1.3535	36.194	0.126	31.630	0.320	0.640
1.3533	36.102	0.218	31.526	0.336	0.672
1.3921	36.166	0.201	31.106	0.410	0.820
1.3849	36.120	0.213	31.324	0.270	0.539

Table B.8: 40° Glass results

Intended Incidence angle	40				
Material	Glass				
Mach Number	Average actual incidence angle	Actual incidence angle std. deviation	Average reflection angle	Reflection angle std. deviation	Reflection angle error
1.3046	40.194	0.187	40.064	0.201	0.402
1.3039	40.220	0.213	40.092	0.041	0.081
1.3037	40.170	0.221	39.900	0.217	0.433
1.3025	40.138	0.200	39.980	0.279	0.558
1.3516	40.192	0.181	40.112	0.059	0.118
1.3537	40.242	0.325	40.210	0.315	0.630
1.3986	40.284	0.264	40.000	0.101	0.202
1.3919	40.254	0.250	40.128	0.153	0.307

Table B.9: 40° Copper results

Intended Incidence angle	40				
Material	Copper				
Mach Number	Average actual incidence angle	Actual incidence angle std. deviation	Average reflection angle	Reflection angle std. deviation	Reflection angle error
1.3046	40.174	0.237	37.738	0.208	0.415
1.3039	40.158	0.157	37.350	0.106	0.213
1.3037	40.126	0.189	37.574	0.143	0.285
1.3025	40.240	0.197	37.038	0.185	0.371
1.3516	40.158	0.152	36.900	0.215	0.430
1.3537	40.116	0.138	36.892	0.327	0.653
1.3986	40.102	0.158	36.612	0.298	0.596
1.3919	40.152	0.238	36.734	0.254	0.507

Table B.10: 40° Brass results

Intended Incidence angle	40				
Material	Brass				
Mach Number	Average actual incidence angle	Actual incidence angle std. deviation	Average reflection angle	Reflection angle std. deviation	Reflection angle error
1.306	40.078	0.116	40.534	0.176	0.353
1.306	40.140	0.101	40.368	0.317	0.635
1.3544	40.324	0.345	40.420	0.301	0.603
1.3542	40.282	0.323	41.052	0.333	0.666
1.3521	40.172	0.096	40.242	0.386	0.771
1.3902	40.264	0.155	40.830	0.365	0.729
1.3893	40.086	0.050	40.214	0.354	0.709

Table B.11: 40° Aluminium results

Intended Incidence angle	40				
Material	Aluminium				
Mach Number	Average actual incidence angle	Actual incidence angle std. deviation	Average reflection angle	Reflection angle std. deviation	Reflection angle error
1.306	40.050	0.135	39.174	0.274	0.548
1.306	40.076	0.216	39.144	0.222	0.443
1.3544	40.094	0.072	38.798	0.217	0.434
1.3542	40.060	0.077	38.670	0.426	0.852
1.3521	40.060	0.090	38.350	0.336	0.673
1.3902	40.014	0.086	38.264	0.378	0.755
1.3893	39.986	0.056	38.434	0.317	0.634

Table B.12: 40° Steel bottom results

Intended Incidence angle	40				
Material	Steel Bottom				
Mach Number	Average actual incidence angle	Actual incidence angle std. deviation	Average reflection angle	Reflection angle std. deviation	Reflection angle error
1.3087	40.278	0.199	40.272	0.349	0.698
1.3003	40.386	0.199	39.732	0.260	0.519
1.2995	40.272	0.187	39.484	0.160	0.320
1.3608	40.336	0.197	39.212	0.297	0.593
1.3521	40.144	0.166	39.044	0.233	0.465
1.3911	40.360	0.263	38.450	0.328	0.656
1.3911	40.440	0.191	38.592	0.316	0.632

Table B.13: 40° Steel top results

Intended Incidence angle	40				
Material	Steel Top				
Mach Number	Average actual incidence angle	Actual incidence angle std. deviation	Average reflection angle	Reflection angle std. deviation	Reflection angle error
1.3087	40.110	0.165	39.316	0.362	0.725
1.3003	40.160	0.181	39.388	0.320	0.640
1.2995	39.904	0.151	39.128	0.238	0.476
1.3608	40.138	0.163	38.806	0.337	0.674
1.3521	39.932	0.194	38.234	0.339	0.678
1.3911	40.112	0.225	38.496	0.345	0.690
1.3911	40.302	0.320	38.478	0.359	0.718

Figure B.2, Figure B.3, Figure B.4 and Figure B.5 show all of the regular reflection results on one graph with and without the error bars respectively.

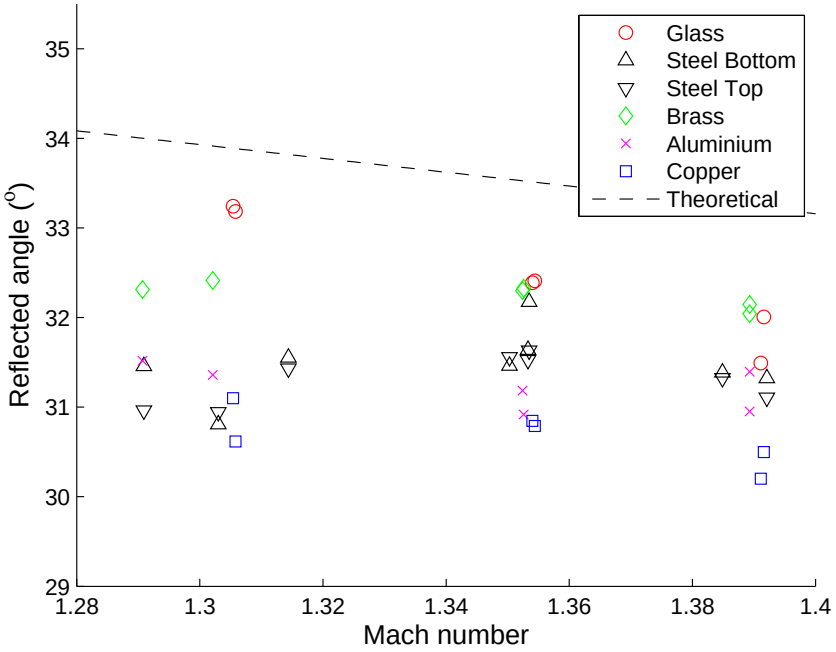

Figure B.2: Graph of all results at 36°

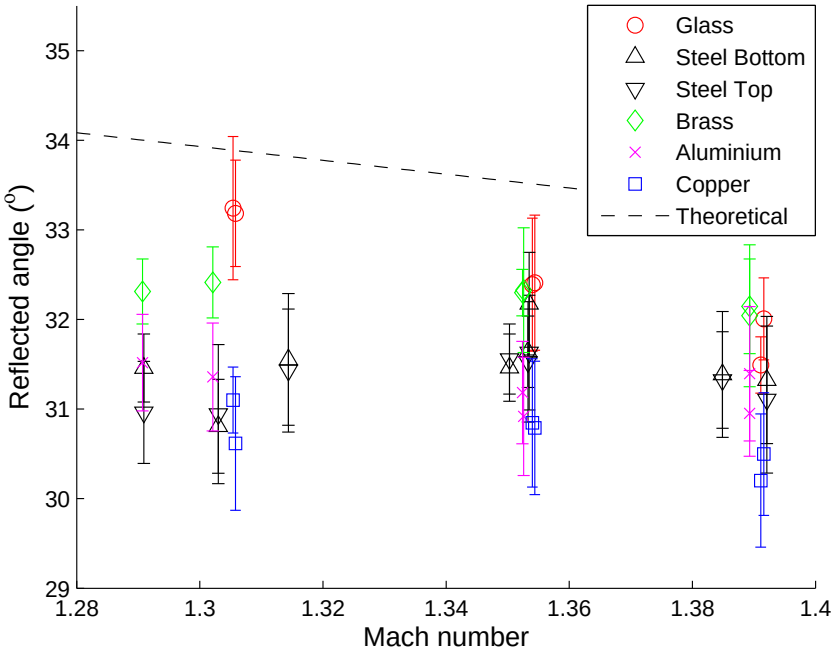

Figure B.3: Graph of steel results at 36° with error bars

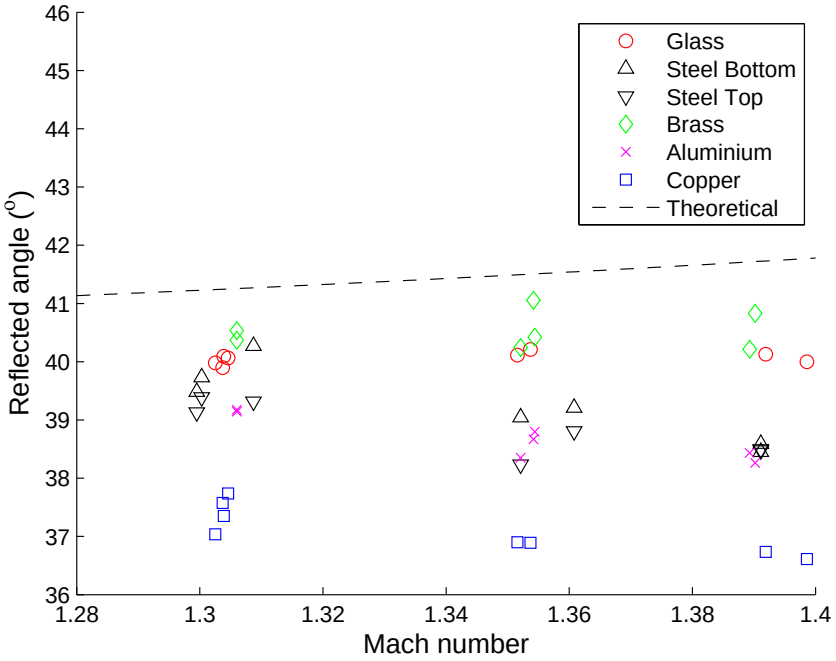

Figure B.4: Graph of all results at 40°

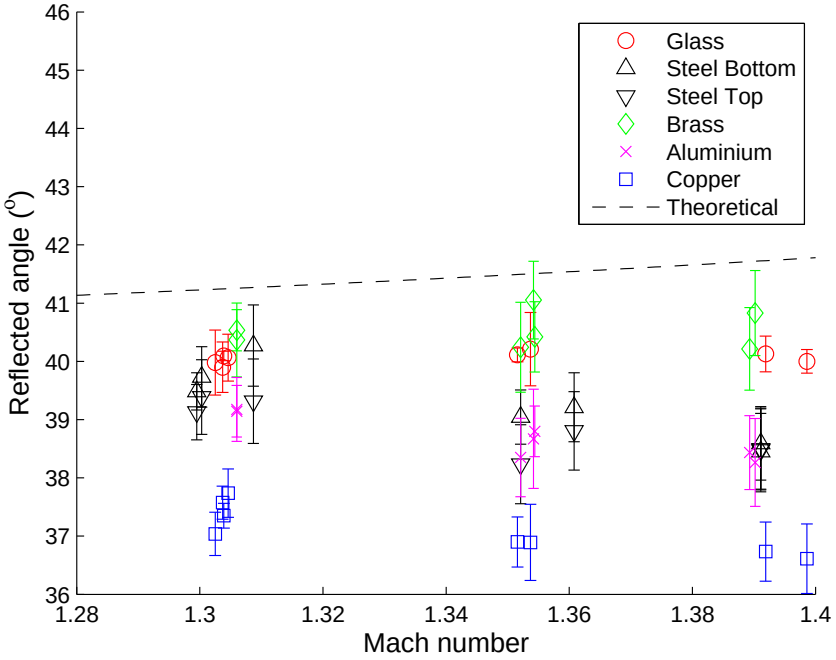

Figure B.5: Graph of steel results at 40° with error bars

B.2.2 Irregular reflection results

Table B.14: 60° Glass results

Intended Incidence angle	60				
Material	Glass				
Mach Number	Average actual incidence	Actual incidence angle std. deviation	Average incidence-reflection angle	Reflection angle std. deviation	Reflection angle error
1.3066	60.030	0.058	60.294	0.099	0.197
1.3042	60.036	0.076	59.828	0.140	0.280
1.3508	60.012	0.087	62.138	0.144	0.289
1.3524	60.042	0.081	62.254	0.133	0.266
1.3893	60.094	0.064	65.102	0.344	0.687
1.3902	59.988	0.087	65.146	0.238	0.476

Table B.15: 60° Copper results

Intended Incidence angle	60				
Material	Copper				
Mach Number	Average actual incidence	Actual incidence angle std. deviation	Average incidence-reflection angle	Reflection angle std. deviation	Reflection angle error
1.3066	60.068	0.061	63.716	0.203	0.406
1.3042	60.032	0.128	63.022	0.401	0.802
1.3508	60.052	0.110	64.568	0.158	0.317
1.3524	60.082	0.131	64.362	0.141	0.282
1.3893	59.980	0.046	67.104	0.252	0.504
1.3902	59.996	0.094	67.120	0.179	0.359

Table B.16: 60° Brass results

Intended Incidence angle	60				
Material	Brass				
Mach Number	Average actual incidence	Actual incidence angle std. deviation	Average incidence-reflection angle	Reflection angle std. deviation	Reflection angle error
1.306	60.002	0.097	62.506	0.104	0.208
1.3056	60.054	0.109	61.858	0.321	0.642
1.3549	59.992	0.078	63.388	0.110	0.219
1.354	60.022	0.067	63.846	0.168	0.337
1.393	59.984	0.067	65.748	0.242	0.483
1.3921	60.062	0.115	65.490	0.175	0.350
1.3793	60.008	0.027	63.892	0.228	0.455

Table B.17: 60° Aluminium results

Intended Incidence angle	60				
Material	Aluminium				
Mach Number	Average actual incidence	Actual incidence angle std. deviation	Average incidence-reflection angle	Reflection angle std. deviation	Reflection angle error
1.306	60.052	0.084	63.296	0.156	0.313
1.3056	60.006	0.071	62.774	0.360	0.720
1.3549	59.970	0.079	64.668	0.164	0.328
1.354	59.996	0.045	64.912	0.149	0.298
1.393	60.062	0.113	66.142	0.130	0.260
1.3921	60.008	0.051	66.256	0.133	0.266
1.3793	59.962	0.057	64.712	0.136	0.272

Table B.18: 60° Steel bottom results

Intended Incidence angle	60				
Material	Steel Bottom				
Mach Number	Average actual incidence	Actual incidence angle std. deviation	Average incidence-reflection angle	Reflection angle std. deviation	Reflection angle error
1.3122	59.992	0.133	60.118	0.191	0.382
1.303	60.006	0.067	60.064	0.128	0.257
1.3025	60.142	0.111	59.906	0.100	0.199
1.351	60.022	0.111	64.452	0.094	0.188
1.3499	60.110	0.100	64.812	0.125	0.250
1.3494	60.000	0.086	64.336	0.208	0.416
1.3919	59.972	0.086	65.936	0.198	0.396
1.3893	60.096	0.132	66.374	0.109	0.217
1.3893	60.064	0.063	65.360	0.227	0.453

Table B.19: 60° Steel top results

Intended Incidence angle	60				
Material	Steel Top				
Mach Number	Average actual incidence	Actual incidence angle std. deviation	Average incidence-reflection angle	Reflection angle std. deviation	Reflection angle error
1.3122	60.020	0.068	59.968	0.283	0.566
1.303	60.058	0.101	60.466	0.403	0.805
1.3025	60.146	0.127	59.820	0.055	0.110
1.351	59.974	0.050	64.230	0.141	0.283
1.3499	60.078	0.073	64.306	0.208	0.415
1.3494	60.072	0.151	64.404	0.191	0.382
1.3919	60.010	0.115	65.550	0.129	0.259
1.3893	60.076	0.099	65.924	0.131	0.262
1.3893	60.064	0.111	65.372	0.171	0.342

Table B.20: 70° Glass results

Intended Incidence angle	70				
Material	Glass				
Mach Number	Average actual incidence	Actual incidence angle std. deviation	Average incidence-reflection angle	Reflection angle std. deviation	Reflection angle error
1.2905	70.034	0.094	51.908	0.109	0.217
1.279	69.996	0.058	52.866	0.173	0.346
1.3521	70.072	0.084	51.985	0.096	0.192
1.3512	69.956	0.082	52.866	0.373	0.746
1.3916	69.990	0.098	53.744	0.289	0.579
1.3849	70.016	0.098	54.614	0.250	0.500

Table B.21: 70° Copper results

Intended Incidence angle	70				
Material	Copper				
Mach Number	Average actual incidence	Actual incidence angle std. deviation	Average incidence-reflection angle	Reflection angle std. deviation	Reflection angle error
1.2905	69.924	0.067	55.234	0.120	0.240
1.279	70.002	0.066	54.972	0.185	0.370
1.3521	70.068	0.026	55.618	0.175	0.349
1.3512	70.072	0.075	55.746	0.198	0.396
1.3916	70.002	0.116	55.684	0.175	0.349
1.3849	69.944	0.040	56.686	0.224	0.448

Table B.22: 70° Brass results

Intended Incidence angle	70				
Material	Brass				
Mach Number	Average actual incidence	Actual incidence angle std. deviation	Average incidence-reflection angle	Reflection angle std. deviation	Reflection angle error
1.3038	70.000	0.086	53.154	0.407	0.814
1.3102	70.084	0.148	53.396	0.391	0.782
1.353	70.026	0.062	53.190	0.342	0.683
1.3526	70.022	0.082	53.276	0.132	0.265
1.3887	70.004	0.099	53.964	0.104	0.208
1.3686	70.062	0.067	53.524	0.064	0.128

Table B.23: 70° Aluminium results

Intended Incidence angle	70				
Material	Aluminium				
Mach Number	Average actual incidence	Actual incidence angle std. deviation	Average incidence-reflection angle	Reflection angle std. deviation	Reflection angle error
1.3038	70.010	0.091	53.842	0.348	0.695
1.3102	70.132	0.206	53.918	0.379	0.757
1.353	69.958	0.097	54.470	0.231	0.462
1.3526	69.992	0.069	54.126	0.150	0.299
1.3887	69.984	0.129	54.450	0.237	0.474
1.3686	69.972	0.044	54.654	0.194	0.389

Table B.24: 70° Steel bottom results

Intended Incidence angle	70				
Material	Steel Bottom				
Mach Number	Average actual incidence	Actual incidence angle std. deviation	Average incidence-reflection angle	Reflection angle std. deviation	Reflection angle error
1.299	69.996	0.138	53.446	0.356	0.713
1.2892	70.068	0.085	53.442	0.247	0.493
1.29	70.082	0.152	53.050	0.304	0.608
1.299	70.020	0.044	52.526	0.082	0.164
1.3144	69.966	0.083	52.398	0.209	0.419
1.3135	70.122	0.066	51.206	0.380	0.759
1.3635	70.068	0.127	53.040	0.370	0.741
1.3481	70.048	0.083	52.624	0.156	0.311
1.3608	70.018	0.056	52.658	0.125	0.251
1.3883	70.536	0.120	52.762	0.205	0.409

Table B.25: 70° Steel top results

Intended Incidence angle	70				
Material	Steel Top				
Mach Number	Average actual incidence	Actual incidence angle std. deviation	Average incidence-reflection angle	Reflection angle std. deviation	Reflection angle error
1.299	69.906	0.071	53.406	0.261	0.522
1.2892	69.986	0.078	53.494	0.429	0.858
1.29	70.010	0.069	53.324	0.269	0.539
1.299	69.974	0.071	52.520	0.183	0.366
1.3144	70.130	0.132	51.804	0.147	0.293
1.3135	70.076	0.147	51.242	0.366	0.732
1.3635	70.074	0.036	53.300	0.445	0.891
1.3481	70.192	0.117	53.004	0.372	0.745
1.3608	69.976	0.066	52.948	0.105	0.210
1.3883	70.320	0.141	53.072	0.348	0.696

Table B.26: 70° Glass (Reversed) results

Intended Incidence angle	70				
Material	Glass Reversed				
Mach Number	Average actual incidence	Actual incidence angle std. deviation	Average incidence-reflection angle	Reflection angle std. deviation	Reflection angle error
1.3141	70.104	0.050	50.972	0.257	0.514

Table B.27: 70° Copper (Reversed) results

Intended Incidence angle	70				
Material	Copper Reversed				
Mach Number	Average actual incidence	Actual incidence angle std. deviation	Average incidence-reflection angle	Reflection angle std. deviation	Reflection angle error
1.3141	70.014	0.082	54.272	0.121	0.242

Figure B.6, Figure B.7, Figure B.8 and Figure B.9 show all of the irregular reflection results on one graph with and without the error bars respectively.

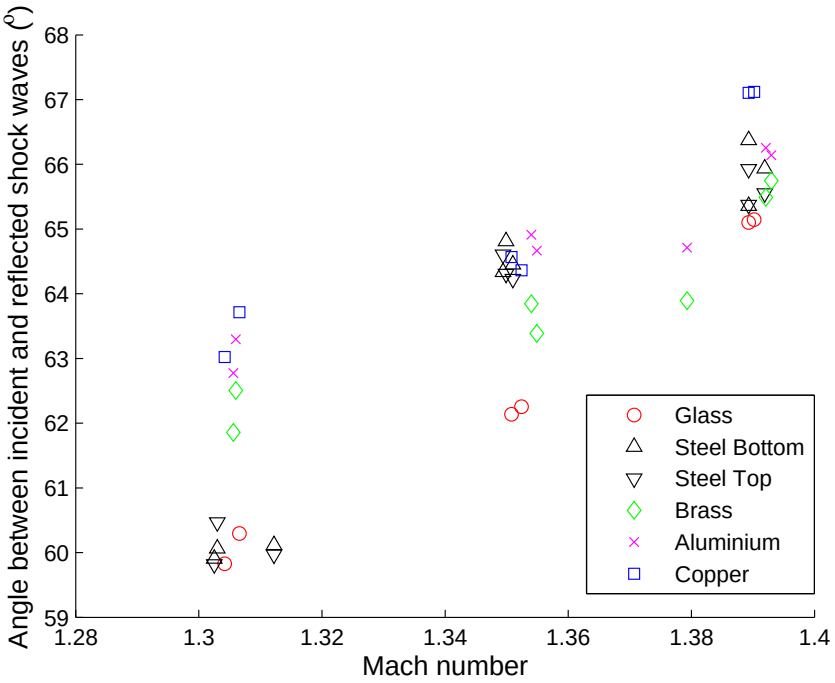

Figure B.6: Graph of all results at 60°

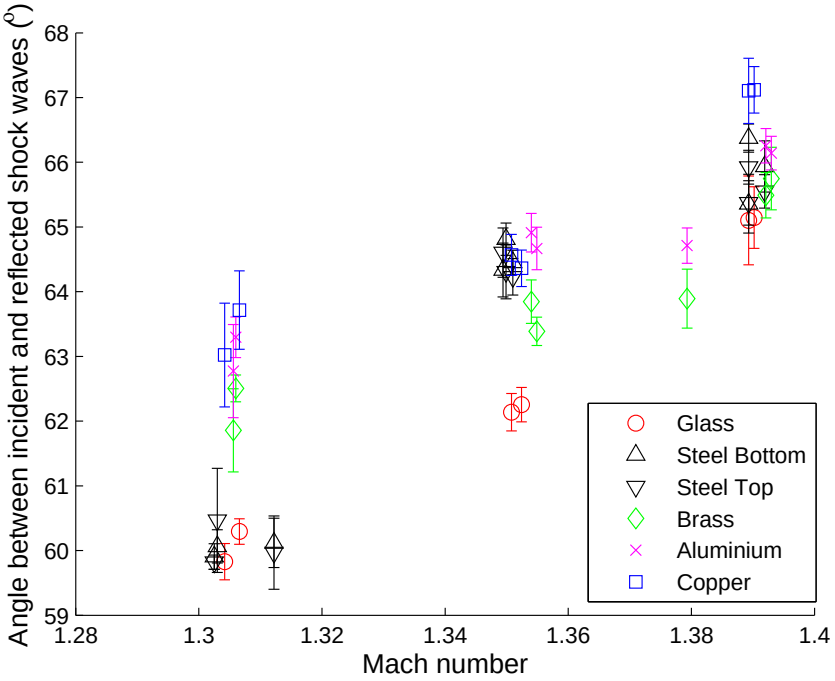

Figure B.7: Graph of steel results at 60° with error bars

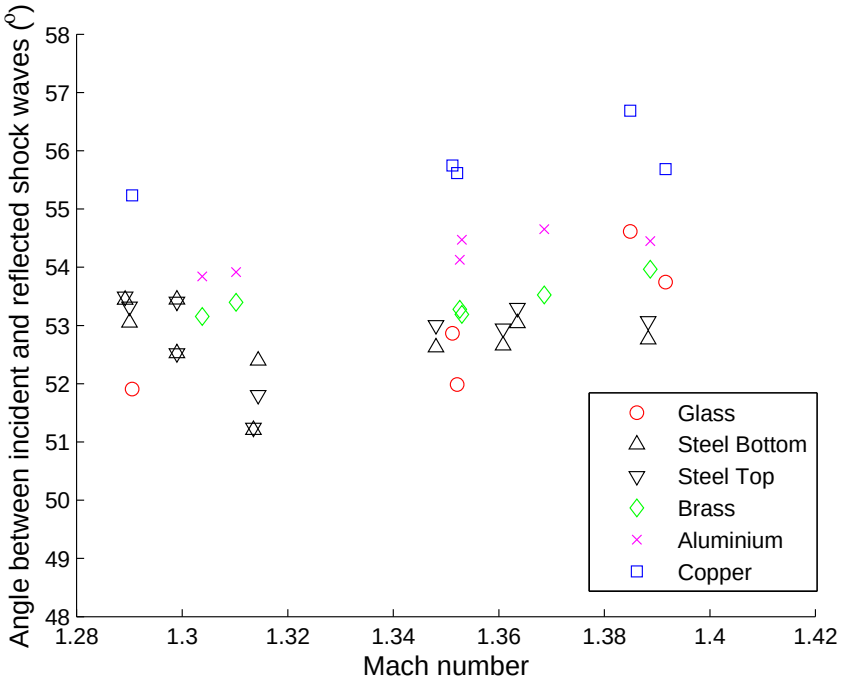

Figure B.8: Graph of all results at 70°

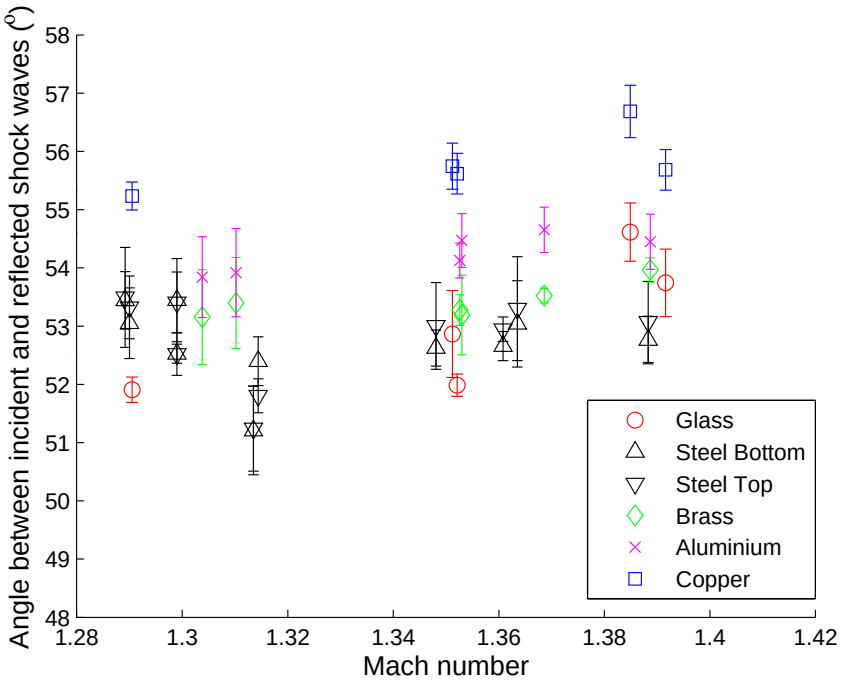

Figure B.9: Graph of steel results at 70° with error bars

Appendix C Uncertainty Anaylsis

The uncertainty analysis follows the method suggested by L. Kirkup in the statistical approach to variability in data [**23**].

The uncertainty represented as the error bounds in the graphs is twice the standard deviation of the results from the mean. The standard deviation is calculated as:

$$\sigma = \sqrt{\frac{\sum (x_i - \overline{x})^2}{n}}$$

Where the mean $\overline{x}$ is calculated as:

$$\overline{x} = \frac{\sum x_i}{n}$$

The error bounds are $\pm 2\sigma$ this introduces a 95% confidence limit which means that true mean has a 95% chance of lying between $\pm 2\sigma$.

An example is shown inTable C.1 where the results of each measurement of glass at 36° at M1.3058 are shown as well as the standard deviation and error bounds.

Table C.1: Example of uncertainty calculation

Measurement	Actual incidence angle	Reflected angle
1	36.55	33.77
2	36.10	33.08
3	36.26	33.05
4	36.15	33.07
5	36.15	32.95
Average	36.242	33.184
Standard Deviation	0.163	0.297
2×Std. Dev. (error bounds)	0.325	0.593

Appendix D Digital Appendix

The digital appendix contains the following folders and documents:

- Adjusted Images Folder - This contains all the experimental pictures that were adjusted in Corel Photo-Paint X4 before being analysed.
- Admin Documents Folder - This contains the risk assessment, procedures and pressure circuit diagrams for the LSDST.
- Autodesk Files Folder - This contains the Autodesk part, assembly and drawing files used in the design of the pricker and test rig as well as the repairs made to the shock tube.
- Blue Tube Code Folder - This contains the Matlab code used to theoretically calculate the regular reflection angles as well as a code for calculating the delay required for the optical set up.
- Experimental Pics Folder - This contains the original photos taken during experimentation without adjustment. They are referenced to the date, test number and Mach number of each test, which can be checked against the test log in Appendix B
- Graph Codes Folder - This contains the Matlab codes used to graph the quantitative results.
- Graphs folder - this contains the eps files of the quantitative graphs that were shown in the dissertation.
- Qualitative Pics - This contains the pictures after adjustment and identified for the qualitative analysis placed in the dissertation.
- Results Part Files - This contains the Autodesk part files with all measurements made as well as centrelines drawn. The quantitative part files are referenced to the material pair, date, test number and which measurement that part file refers to.

- Irregular reflection Results - This is an excel spreadsheet of all irregular reflection angle measurements.
- Regular reflection Results - This is an excel spreadsheet of all regular reflection angle measurements.